

NGST MONOGRAPH No. 1

NGST “Yardstick” Mission

Edited by:

Pierre Y. Bely (Space Telescope Institute);

Charles Perrygo (Swales Aerospace);

Richard Burg (Johns Hopkins University)

July 1999



Next Generation Space Telescope
Project Study Office
Goddard Space Flight Center

TABLE OF CONTENTS

1. PREFACE	1-1
2. OPTICAL TELESCOPE ASSEMBLY	2-1
2.1 Optical configuration	2-1
2.2 Primary mirror	2-3
2.3 Secondary and following mirrors	2-6
2.4 Baffles	2-8
2.5 OTA structure	2-9
2.6 Mirror coating	2-10
3. SCIENCE INSTRUMENT MODULE	3-1
3.1 Introduction	3-1
3.2 Focal plane arrangement	3-1
3.3 NIR camera	3-2
3.4 NIR spectrometer	3-3
3.5 MIR camera and spectrometer	3-4
3.6 Detectors	3-5
3.7 Structures and mechanisms	3-9
3.8 Thermal system	3-10
3.9 Cryogenic system for the MIR instrument	3-12
3.10 Calibration of instruments	3-14
3.11 Instrument operational modes	3-15
3.12 Science and engineering data	3-16
3.13 Control electronics and power supply	3-17
3.14 ISIM mass estimate	3-19
4. SPACECRAFT SUPPORT MODULE	4-1
4.1 The spacecraft bus	4-1
4.2 The isolation truss	4-3
4.3 The Sunshield	4-4
4.4 Power Subsystem	4-6
4.5 Command and data handling	4-8
4.6 Communication system	4-10

5. WAVEFRONT CONTROL SYSTEM	5-1
5.1 Wavefront Sensing	5-1
5.2 Optical Element Actuators	5-2
5.3 Wavefront Control Process	5-2
5.4 Fine Figure Control	5-5
6. THERMAL SYSTEM	6-1
6.1 Thermal design overview	6-2
6.2 Thermal environment	6-3
6.3 Thermal modeling	6-3
6.4 Results	6-5
7. POINTING CONTROL SYSTEM	7-1
7.1 Rationale	7-1
7.2 Spacecraft attitude control system	7-2
7.3 Line of Sight Stabilization	7-4
7.4 Predicted performance	7-7
8. MASS ESTIMATE	8-1
9. ORBIT AND LAUNCH	9-1
9.1 Orbit	9-1
9.2 Launch Vehicle	9-2
9.3 On-Board Propulsion System	9-2
10. OBSERVATORY PERFORMANCE	10-1
10.1 Introduction	10-1
10.2 Point Spread Function	10-2
10.3 Influence of line of sight jitter	10-3
10.4 Slew time - Settling time after a slew	10-5
10.5 Thermal effects of slews	10-5
10.6 Instrumental backgrounds	10-6
10.7 Sky coverage	10-7
10.8 Wavefront error budget	10-9
10.9 Throughput	10-11
10.10 Meeting the science goals	10-12
APPENDIX A: LIST OF CONTRIBUTORS	A-1
APPENDIX B: LIST OF ACRONYMS	B-1

1. PREFACE

The Next Generation Space Telescope (NGST) is under study by NASA as a successor to the Hubble Space Telescope (HST) within the framework of the NASA Origins program. The scientific objectives of the NGST mission focus on themes related to the large scale geometry of the universe, the origin of galaxies and the nature of the earliest generations of stars.

This monograph describes the Yardstick Mission developed by NASA for 1. establishing a robust reference design against which the industry designs can be compared; and 2. offering the Project Office staff a basic concept with which various studies could be performed to become a “smart customer,” and 3. assist in determining the areas in need of technological development.

The design of the Yardstick Mission was conceived as part of a feasibility study performed by a team of scientists and engineers from NASA, academia and industrial concerns in the summer of 1996¹. The design was subsequently refined and analyzed in detail by GSFC, MSFC and JPL over the following 18 months. Technically, the “bar was set high” in order to motivate fresh thinking and innovation among the industrial firms in charge of the overall NGST designs and of the technological development (e.g. large size, fast and ultra-lightweight primary mirror, optical phasing by phase retrieval, low operating temperature). Hence, the Yardstick Mission walks a fine line between risky new concepts, sound but possibly expensive engineering approaches and conservatism to ensure feasibility.

The design philosophy is based on the following assumptions and rationale:

- Nominal lifetime of 5 years, with a goal of 10 years
- No on-orbit maintenance
- Functional redundancy as opposed to system redundancy
- Extensive use of active optics in order to reduce optics cost and mass, ease-up requirements on attitude control system
- Use same material for optics and telescope structure to avoid CTE mismatch problems when OTA temperature goes from ambient to cold
- Use science camera for guiding to reduce cost
- On-board acquisition of guide stars to save on ground operations cost and minimize instruction time overheads
- Individual focussing for each instrument

A large number of engineers and scientists worked on the development of the yardstick concept over the course of two years. The list of main contributors is given in Appendix A.

The Yardstick Mission uses a deployable 8 meter diameter telescope optimized for the near infrared region (2-5 microns), but with instruments capable of observing from the visible all the way to 30 microns. The observatory is radiatively cooled to about 30 K and would be launched on an Atlas IIAS to the Lagrange Point L2. The main characteristics of the observatory are shown in Table 1.1.

Table 1.1. NGST Yardstick architecture main characteristics

<i>Item</i>	<i>Value</i>
Scientific performance	
Wavelength coverage	0.6 to 30 microns
Aperture	8 meter, quasi-filled
Point source sensitivity	4 nJy in 10,000s at 2 microns, S/N=10, BP=20%
Resolution	0.050 arcseconds (diffraction limited at 2 μ m)
Science instruments	cameras, multiobject spectrograph
Field	NIR: 4'x4' (camera) 3'x3' (spectrograph)
	MIR: 2'x2' (camera)
Sky coverage	Yearly: full sky Instantaneous: 17%
Technical features	
Optics configuration	3-mirror anastigmat with accessible exit pupil
Aperture diameter	8 meters OD, 7.2m effective dia
Wavefront control	image-based wavefront sensing with 5 DOF mirror actuation + DM
Optics temperature	<70 K (50 K nominal)
Mirror material	lightweight beryllium
System <i>f</i> ratio	<i>f</i> /24
Fine pointing	10 mas
Data rate	1.6 MB/s
Mission aspects	
Mass	<3300 kg
Spacecraft pointing accuracy	2" rms
Power	800W
Mission lifetime	5 years nominal- 10 years goal
Orbit	Sun-earth Lagrange 2 Halo orbit
Launcher	Atlas II AS
Programmatic aspects	
Cost of manufacture	\$564M (1996 \$)
Development duration	48 months
Launch date	June 2007

Figure 1.1 shows the overall view of the observatory and its main components. It is composed of the Optical Telescope Assembly (OTA), the Integrated Science Instruments Module (ISIM) and of the Spacecraft Support Module (SSM).

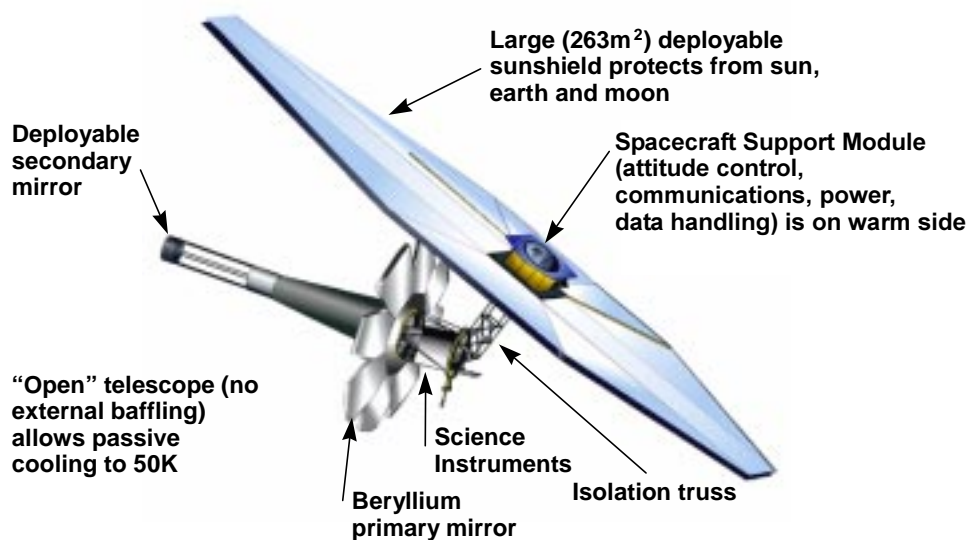


Figure 1.1. Artist's view of the Yardstick Observatory and its main components.

2. OPTICAL TELESCOPE ASSEMBLY

2.1 Optical configuration

The optical configuration is a three-mirror anastigmat design* that provides a real, accessible pupil and permits the use of a relatively fast primary mirror to minimize telescope length. This design provides excellent imaging over a large field with relatively loose alignment tolerances. A real pupil permits the use of a deformable mirror for wavefront correction and a fast steering mirror for fine pointing. A cool stop can also be placed at this pupil. All of the optics following the secondary are conveniently located behind the primary.

The three mirrors have the same optical axis, but to avoid obscuration by the deformable mirror and the fast steering mirror, the optical system is used off-axis as shown in Figures 2.1 and 2.2. Field curvature has been introduced into the design in order to keep the off-axis principal rays normal to the final image surface. This prevents defocus from being introduced by the action of the fast steering mirror. The four separate near-infrared cameras are then fitted to the curved image surface. The individual detector array chips within each camera could even be fitted separately to the image surface if desired for ultimate performance (i.e. diffraction-limited performance at a shorter wavelength). Also, the deformable mirror has been tilted downward to achieve the best fit to the primary's image.

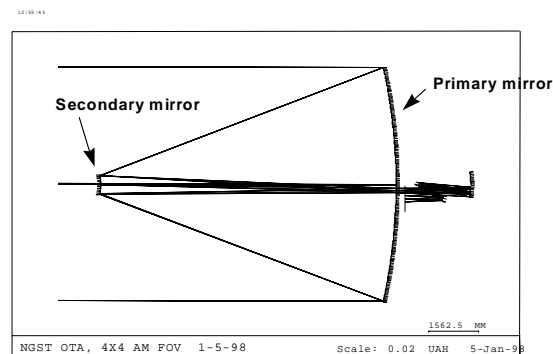


Figure 2.1. Optical layout of the telescope.

*The yardstick optical train was originally optimized to maximize image quality over the usable field, but without particular attention to distortion because it can be calibrated out in the science images.

It was recently realized, however, that the FSM shifts the mapping of the distortion field onto the focal plane as it rotates to compensate jitter. This results in a displacement of the image of all points in the field. A second, independent effect of the FSM activation is that the field rotates about the guide star.

Both effects grow with the field angle from the guide star and in the current design add up to a displacement on order of a pixel at the edge of the NIR camera.

It is likely that the design described here will have to be altered in some way to reduce these effects.

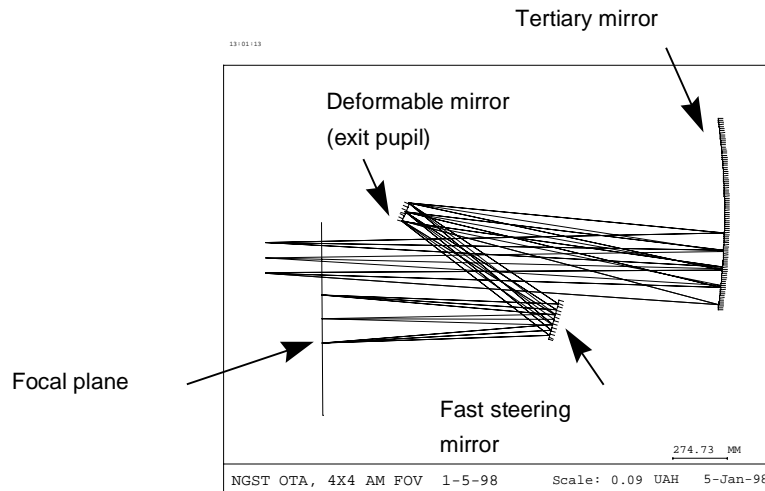


Figure 2.2. Close-up view of tertiary-to-image optics

The optical quality of the system at its final focus (following the tertiary and the deformable and fast steering mirrors) is excellent over the full 4 arcminute by 4 arcminute field of the near-infrared camera as shown in the spot diagrams in Figure 2.3. The rms wavefront error is 0.028 waves at 2 microns, well below the defraction limit of 0.071 waves defined by the Marechal condition. It must be noted that this focus is not used directly. Optical relays are used to transfer the 2 x 2 arcminute sub-images to the individual detectors providing an additional capability to correct for residual aberrations.

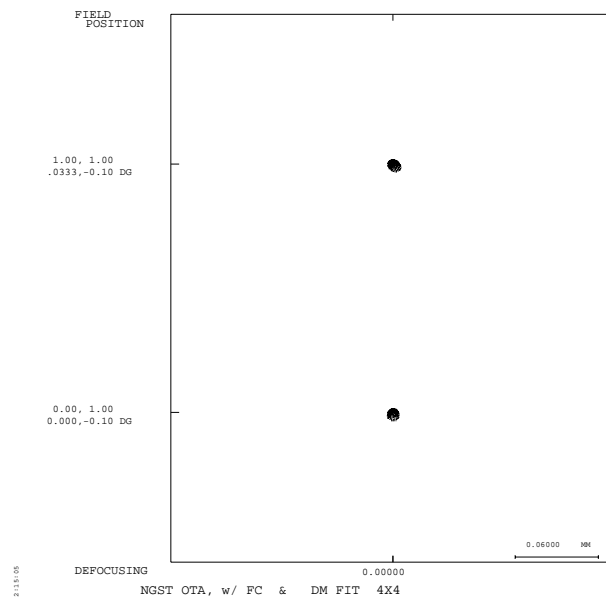


Figure 2.3. Spot diagrams at final focus, center of field (bottom) and 2' from center (top).

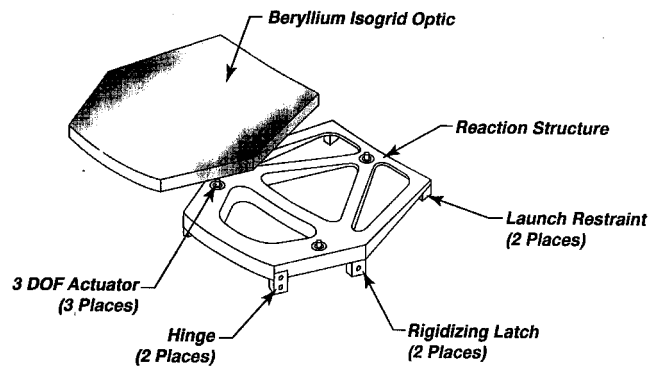
Table 2-1. Main optical parameters of the telescope

Item	Value
Primary mirror diameter	8m
collecting area	40.8 m ²
f/ratio	1.25
conic constant	-0.9984
Secondary mirror diameter	0.66 m
radius of curvature	1.678 m
conic constant	-1.3699
prim-sec separation	9.231 m
Tertiary mirror diameter	0.95 m
radius of curvature	2.864 m
conic constant	-0.7209
sec-tert separation	11.57 m
Deformable mirror diameter	0.092 m
tert-DM separation	1.645 m
Fast steering mirror diameter	0.31 m
DM-FSM separation	0.902 m
Exit pupil diameter	0.092 m
location	at DM
de-magnification	87
Final focus FSM-Image separation	1.179 m
f/ratio	f/24
plate scale	1.1"/mm

2.2 Primary mirror

The primary mirror is composed of a central core 3.3 m in diameter surrounded by 8 off-axis petals approximately 2.2 m long and 1.8 m wide. The total collecting area is 40.8 m² which is equivalent to a full circular aperture of 7.2 m in diameter. The petals are folded alternatively up and down for launch. This number of petals is a compromise between the desire to maximize collecting area once deployed and to minimize volume when folded for launch: because some area is lost at each petal edge, the number of petals should be minimized, but when that number is too small a large area is lost at the periphery where the petals are not contiguous. It must be noted also that the up and down folding scheme leads to very efficient packaging but requires an even number of petals if the aperture is to be symmetric.

The mirror segments are made of beryllium, which has the highest stiffness-to-density ratio and the highest thermal conductivity of all optical materials. Beryllium also has the advantage of a very low and uniform coefficient of thermal expansion (CTE) at cryogenic temperatures. These properties result in the lightest mirror that can be produced for a given stiffness, and negligible distortion at the operational cryogenic temperature on orbit. The type of beryllium selected is the hot isostatically pressed type made of spherical powder which results in a highly isotropic material. The mirror blanks are fabricated by near net shape injection molding method followed by minimal low stress machining. The mirror blanks have an overall thickness of 40 mm and an open back (see Figure 2.4). The facesheet is 2 mm thick and the isogrid core is made of 100 mm cells with 1.5 mm webs. The areal density of the mirror elements is 6.3 kg/m².



Typical Beryllium Petal Assembly

Figure 2.4. Typical Beryllium Petal Assembly

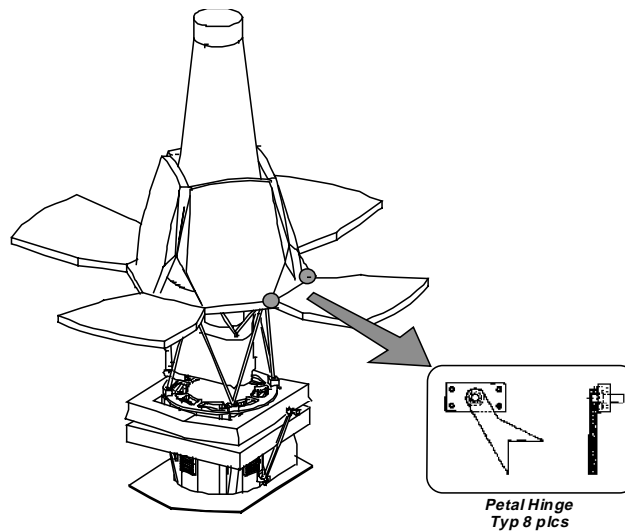


Figure 2.5. Primary mirror deployment system

The mirrors are polished using “cold-figuring”. Cold figuring refers to a manufacturing procedure wherein the optics are fabricated at room temperature, but tested at a cryogenic temperature close to that at which the optics will operate. Cold figuring significantly reduces both the gross aberration, and the differential aberrations due to material anisotropies, incurred in going from ambient to cryogenic operating temperatures. Since the coefficient of thermal expansion of beryllium is very small and almost constant below 80 K, it is sufficient to perform the cold figuring at about liquid nitrogen temperature (77K).

Each mirror segment is supported on 3 actuated bipods which provide 6 degree of freedom positional adjustment. These actuators have two stages, a long throw coarse stage, and a limited travel high accuracy stage. The first stage with a total travel of 5 mm is used to correct for deployment errors and cool down distortions of the backup structure. The second stage, having a positional accuracy of 30 nanometers, is used for final alignment and periodic readjustments. In addition, the mirror figure of each mirror segment can be adjusted using a set of 3 force actuators located at the periphery and one at the center. These force actuators, with a capacity of 1 Newton, are used to compensate for radius of curvature mismatch between segments and to correct for low order aberrations due to residual polishing errors and cool down distortions. When supported kinematically on their mounts, the first bending mode of the mirror segments is 6.07 Hz.

The primary mirror backup structure is a deployable truss made of beryllium for lightness and to match coefficient of thermal expansion with the mirrors. Locking mechanisms are used to firmly connect the central part and the 8 petals of the backup structure upon deployment in order to form a single structure to support the mirror segments (Figure 2.5).

The mirror segments are maintained in mutual alignment both in angle and in piston, using a wavefront control system described in detail in section 1.3. Wavefront errors are measured using a relatively bright star, and the mirrors adjusted in tip/tilt and piston to minimize that error. The mirror elements are then left untouched until a new calibration is considered necessary following major attitude change.

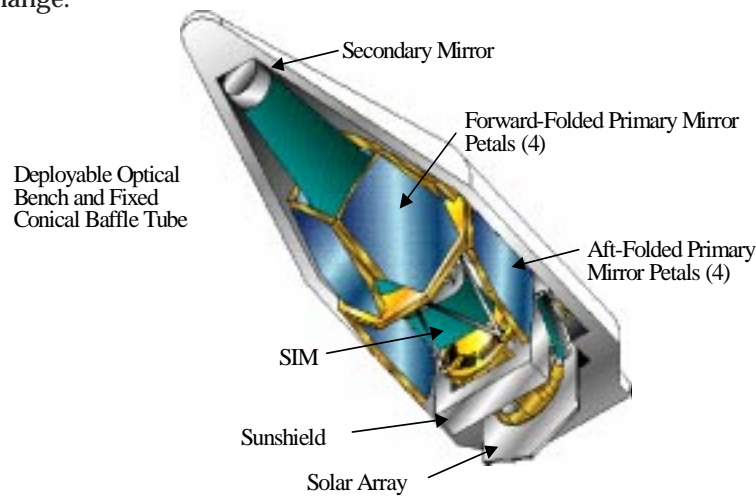


Figure 2.6. View of the OTA folded for launch in an Atlas IIARS fairing

Table 2.2. Mass breakdown for typical primary mirror petal.

<i>Item</i>	<i>Mass (kg)</i>
Mirror	27.0
Support structure	20.0
Kinematic mount actuators (3)	1.5
Figure control actuators (3)	0.9
Hinges	2.0
Latches	2.0
Cables	2.0
Total	54.4 kg
Areal density	13.5 kg/m ² (area of a petal is ~4.1 m ²)

2.3 Secondary and following mirrors

The secondary mirror is 70 cm in diameter, made of light weighted beryllium and is mounted on precision actuators for positioning and alignment with 5 degrees of freedom. The secondary mirror is supported off the central baffle tube on 4 thin struts that extend from a collar around the central baffle tube to the secondary mirror baffle. For stowage in the launch vehicle fairing, the collar slides down the outer diameter of the central baffle with the secondary assembly latching to the top of the central baffle. The four struts are in the converging return beam from the primary mirror, and their re-entry obstruction must be minimized. The struts location and dimensions are shown in Figure 2.8.

The tertiary mirror, located below the primary corrects for aberrations to provide high quality imaging of the large field of view and to produce an accessible exit pupil where a deformable mirror is located for correcting residual wavefront errors.

The deformable mirror (DM), is 92 mm in diameter and has 349 actuators arranged in a square grid array with 5 mm pitch. This represents a scale of 40 cm in the primary mirror. The maximum actuator stroke is 4 mm. The DM is located at the exit pupil.

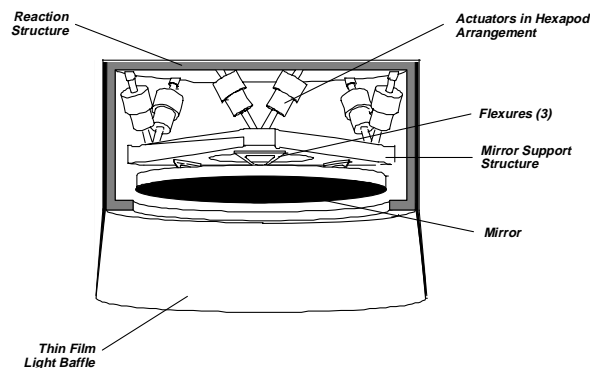


Figure 2.7. Schematic view of the secondary mirror support system

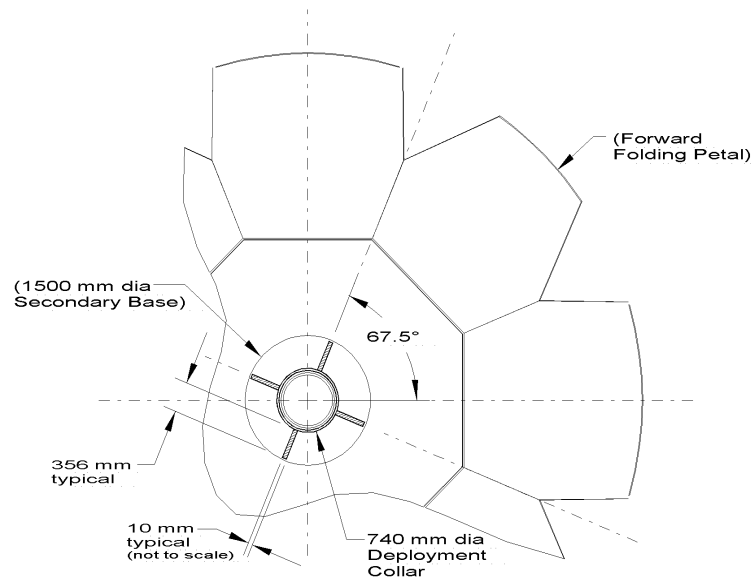


Figure 2.8. Cross section of the struts holding the secondary mirror.

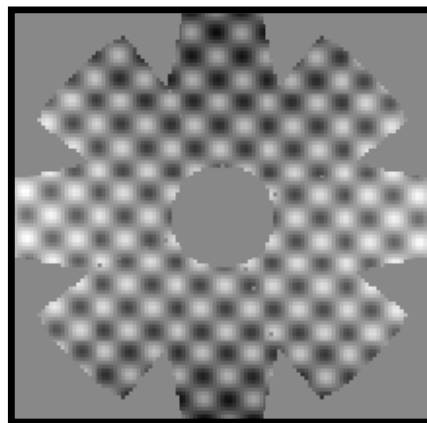


Figure 2.9. Actuator pattern of the deformable mirror superimposed onto the primary mirror pupil

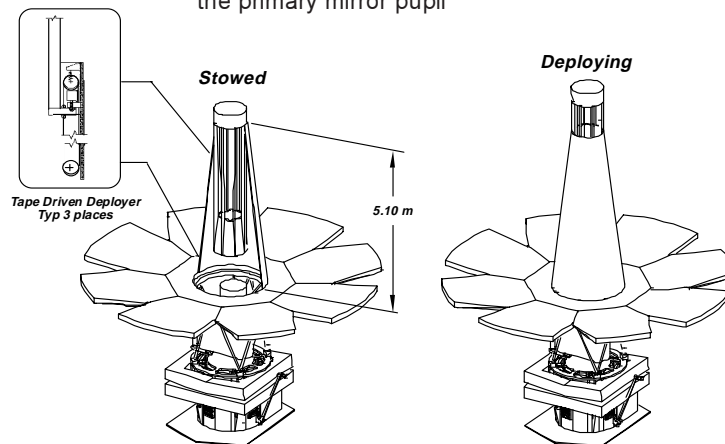


Figure 2.10. Deployment of the secondary mirror.

The fast steering mirror is 31 cm in diameter and has a maximum range of $\pm 6.6'$ in tip and tilt. With a magnification of about 26, this represents a range of ± 15 arcseconds on the sky. The actual maximum stroke, however, is limited by the constraints in the optical design and is on the order of $\pm 2''$ on the sky.

2.4 Baffles

The OTA baffling system is composed of a baffle at the secondary mirror, a central baffle above the primary mirror and a field stop at the first focus. Together, they prevent direct light coming from sources outside of the field of view from entering the field (Figure 2.11). The baffles have vanes and are coated to minimize secondary bounces. There is no external baffle in order for the OTA to see a large view of space and cool down passively to cryogenic temperatures. For L2 orbits, the moon and the earth are always hidden by the sun shield except possibly at the largest elongation in which case observations can be selected in directions away from these bright bodies. In general, though, the only source of off-axis light will be due to stars and the zodiacal light. A detailed straylight analysis has shown that the integrated starlight on the open primary and secondary mirror creates a level of straylight at the focal plane which is more than an order of magnitude lower than that of the zodiacal light in the field of view.

In the near infrared and mid infrared, the thermal background due to the self emission of the optics and radiation from the back surface of the sunshield scattering of the primary and secondary mirrors. A detailed analysis of these effects shows that, provided that the sunshield back surface is at 100 K or less, the resulting background at the focal plane from the thermal is negligible compared to the zodiacal light up to the mid-IR (10 microns).

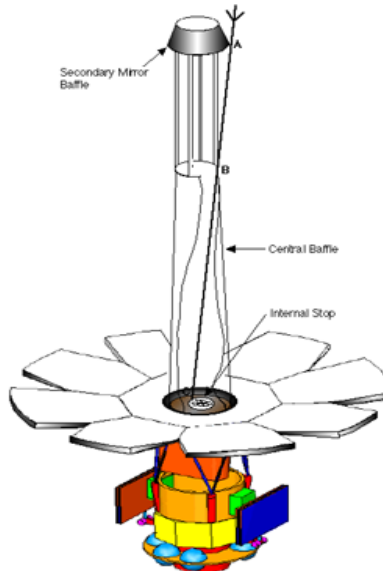


Figure 2.11. Location and dimension of the main baffles and field stop. The edge of the secondary minimum baffle (A), the edge of the central baffle (B) and the edge of the field stop (C) are defined so that no source outside of the field of view can enter the system.

2.5 OTA structure

Beryllium is used throughout the optics and structure in order to minimize shifts in alignment and focus during cooldown. Since this is not perfect, the structure alignments and optical figures are fabricated with a bias at room temperature, which is removed thermally as the spacecraft goes to its operating condition.

The telescope structure comprises an 8-sided deployable truss to which the primary mirror petals are attached, and a conical tube supporting the secondary mirror system (Figure 2.12). The central part of the primary mirror backup structure has two rings (Figure 2.13). The inner ring supports the ISIM, and the outer one is connected to the SSM deployable isolation truss via a 4-sided truss surrounding the ISIM. This ensures that the ISIM is not in the load path whether during launch or on orbit.

Beryllium is used throughout the optics and structure to minimize shifts in alignment and focus during the cooldown following launch as well as after slews during operation. Since this is imperfect, optical figures and alignments are biased at room temperature so that the desired prescription is attained when the observatory reaches operating temperature.

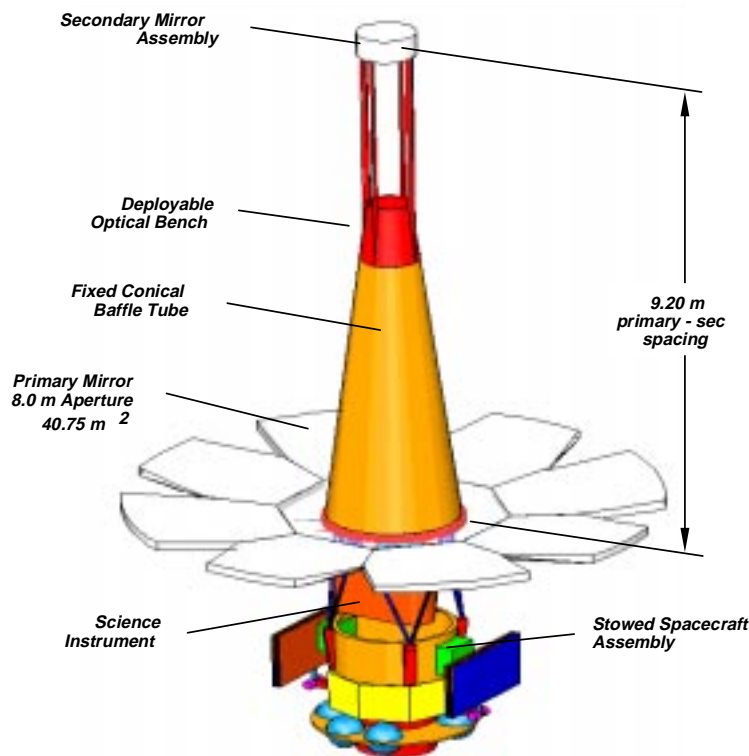


Figure 2.12. Overall view of the OTA

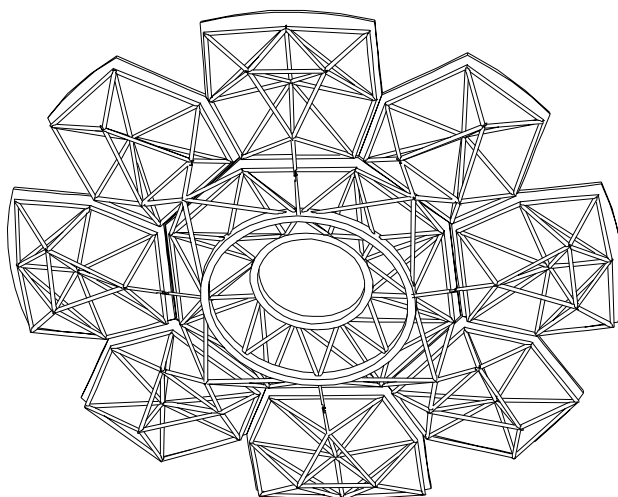


Figure 2.13. View of the back of the primary mirror

2.6 Mirror Coating

Each mirror in the OTA optical train is coated with gold. Gold provides excellent reflectivity in the near infrared and mid infrared and still has an acceptable reflectivity in the visible down to 0.6 micron. Figure 2.14 shows how the reflectivity of gold compares to that of silver and aluminum. Silver would perform better in the visible, but it needs to be protected from oxidation and this leads to losses in reflectivity in the near and mid infrared typically on the order 20 %. Protected silver coatings are also problematic for large mirrors in as much that they cannot be removed except by repolishing the mirror if something goes wrong with the coating process.

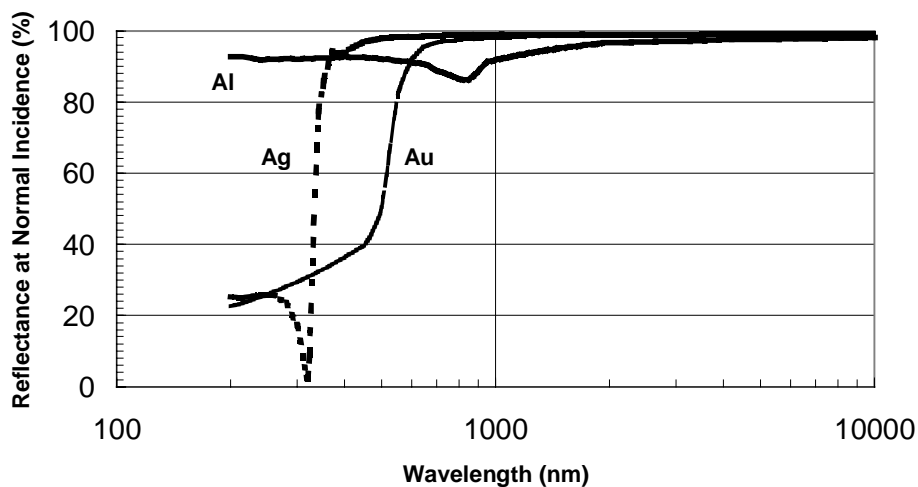


Figure 2.14. Reflectance of evaporated metals in the visible and infrared⁴

Bare gold has the disadvantage of being soft and easily damaged, and appropriate cleaning techniques must be used. Gold can be overcoated with single layer for protection and with multilayer dielectrics for selective enhancement, but both options will reduce reflectivity over a portion of its useful spectral range. The use of bare gold as a mirror coating produces the most uniform high reflectivity throughout the infrared spectrum.

The thermal expansion coefficient of gold differs from that of beryllium but gold is very soft and the stresses induced by the bi-metallic effect following cooldown from ambient to operating temperature are negligible.

3. SCIENCE INSTRUMENT MODULE

3.1 Introduction

The instrument suite is composed of a near infrared camera (actually composed of 4 sub cameras all identical), a multi-slit near infrared low resolution spectrograph and a mid-infrared camera/spectrograph combination. Table 3-1 summarizes the key parameters of the instrument suite.

Table 3.1. Main instrument characteristics

<i>Instrument</i>	<i>Detector</i>	<i>Wave-length range</i>	<i>Resol. Element (microns)</i>	<i>Resol. Element (mas)</i>	<i>F/D</i>	<i>Array size</i>	<i>Field of view (arcmin)</i>	<i>Critically sampled (microns)</i>
NIRCAM	InSb	0.6-5.3	27	29	23.8	8192	4x4	2.3
MIRCAM	Si:As	5-30	27	117	5.5	1024	2x2	9.1
NIRSPEC	InSb	0.6-5.3	27	100		4096	3x3	
MIRSPEC	Si:As	5-30	27	120		1024		

The near infrared camera, the mid-infrared camera and the multi-slit near infrared spectrograph can work in parallel thereby significantly decreasing the time required for performing surveys. The cameras do not need prior target acquisition, since their field of view is large compared to the uncertainties of the pointing system, but when not working for specific fields, the near infrared multi-slit spectrograph can also be used in a fully autonomous parallel mode (“point and shoot”) with automatic selection of the targets increasing even further its usefulness.

3.2 Focal plane arrangement

The focal plane arrangement of the science instrument apertures is shown in Figure 3.1. The optical axis is located at the center of the NIR camera.

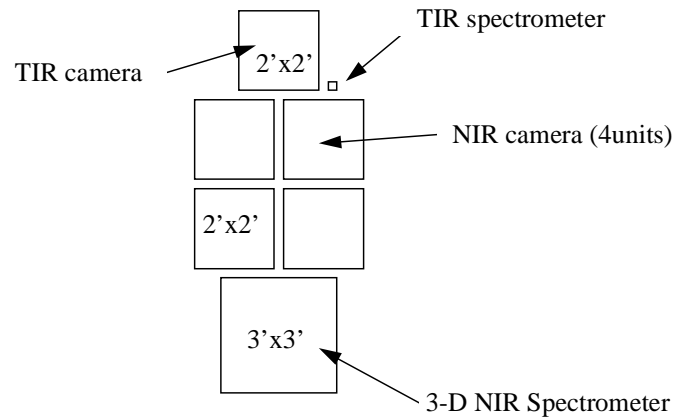


Figure 3.1. Focal plane arrangement. The NIR is located at the center of the field of good optical quality which is xx away from the optical axis of the telescope.

3.3 NIR camera

The NIR camera is a wide field imager taking full advantage of the intrinsic spatial resolution of the telescope at wavelengths of 2 microns and above. The camera covers a spectral range of 0.6 to 5.3 microns (the practical range of the InSb detectors) and the magnification is optimized for providing critical sampling at about 2 microns.

Efficient surveying capability, as well as guiding requirements, set the field at about 4 x 4 arcminutes. Because of the practical limits in detector sizes, and the packaging and optical difficulty of building cameras for that large a field, the camera is composed of four subcameras each covering a field of 2x2 arcminutes. This also provides redundancy.

Figure 3.2 shows the optical layout of each of the subcameras. It is composed of an Offner relay which transfers the main telescope field onto the detector while creating a pupil where a filter wheel can be located. The Offner relay is free of all first order aberrations and image quality is excellent over the entire field. Each subcamera is focused by displacing the secondary mirror of its Offner relay.

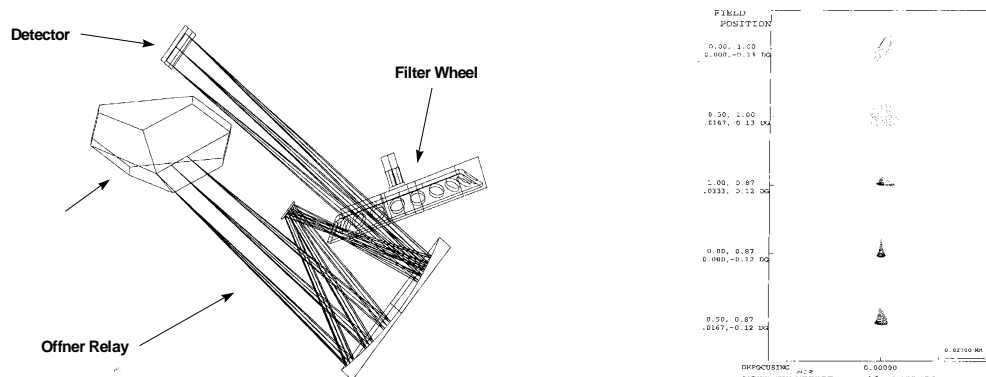


Figure 3.2. Optical layout of one of the four NIR cameras (left) and spot diagram at various points in the field.

A filter wheel with 12 positions is provided for each subcamera with one of these positions a silvered blank for dark current monitoring. Five contiguous broad band filters are provided in all four channels for deep surveys and guiding. These filters have a 50% bandpass and are distributed as follows: 0.65 to 1mm, 1 to 1.5 mm, 1.5 to 2.25 mm, 2.25 to 3.4 mm and 3.4 to 5 mm. The 6 remaining filters are specific to each of the four channels and selected among:

- NICMOS photometric system (F110W, F160W, CO, H2, Paschen-a)
- Set of 20 to 30% medium band filters for redshifts measurements and precision stellar photometry
- Set of grisms

The filter wheel is located at a pupil to minimize filter size. Because of the lack of space, the wheel straddles the return beam and has openings to clear it. The filters are 35 mm in dimension and are matched in thickness so that focus adjustment is not required when changing filters.

3.4 NIR spectrometer

The NIR spectrometer is a multi-slit spectrometer with a spectral resolution of 100, a spatial resolution of 100 mas covering a field of 3 x 3 arcminutes. The inspiration for this instrument is an integrated circuit micromirror array with digital control recently developed by Texas Instruments. The array is composed of 1800 x 1800 micromirrors which can be tilted at ± 20 degrees from the uncontrolled rest position. The array is positioned at a focus such that at one tilt angle, the micromirrors reflect the incoming beam into the spectrograph, while rejecting the beam in the other angle. The micromirrors can be then arranged to form single slits of any desired width and length, or more interestingly can be used to form multiple slits for multiple object spectroscopy. Acquisition of potential targets can be obtained by using the spectrograph in camera mode (a filter is used in lieu of the grisms).

The Texas Instrument chip would not work at cryogenic temperatures and its pixel size is not optional, however. A new device will have to be developed.

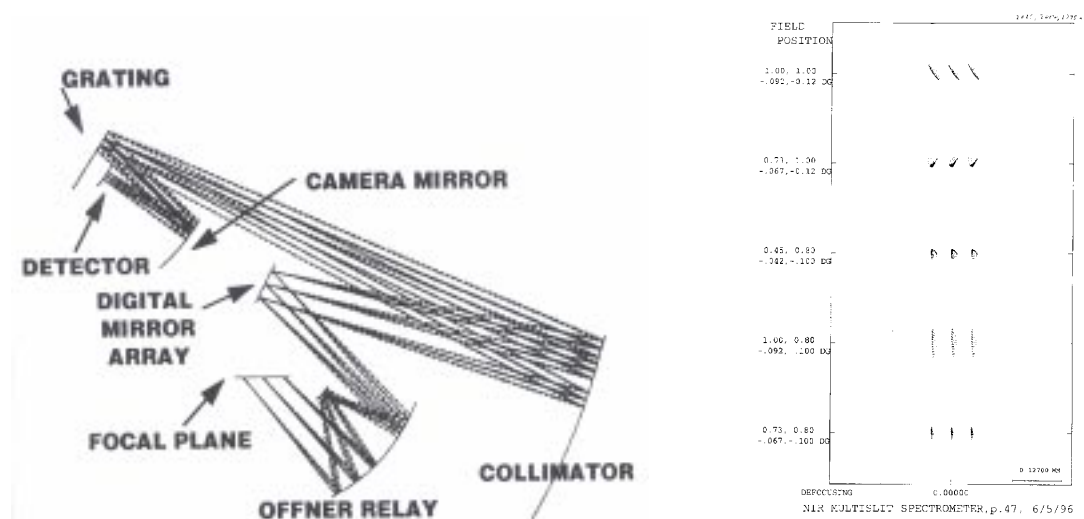


Figure 3.3. Optical layout of the NIR multi-slit spectrometer (left) and spot diagram for various points in the field.

The micromirrors are 100 x 100 microns in size, each one covering 100 mas on the sky.

3.5 MIR camera and spectrometer

The MIR camera covers a field of 2x2 arcminutes over a spectral range of 5 to 30 microns using a 1k x 1k Si:As array as detector. The optical layout is shown in the figure. It is a refractive system which, compared to a reflective system, is shorter and easier to package. Optical elements are also easier to manufacture (reflective elements would require aspheric surfaces), and performance over the wide field is better. The drawback to refractive systems in a space environment is aging effects due to cosmic rays interacting with the lens material. Moreover, Cerenkov radiation and scintillation from cosmic rays must be evaluated.

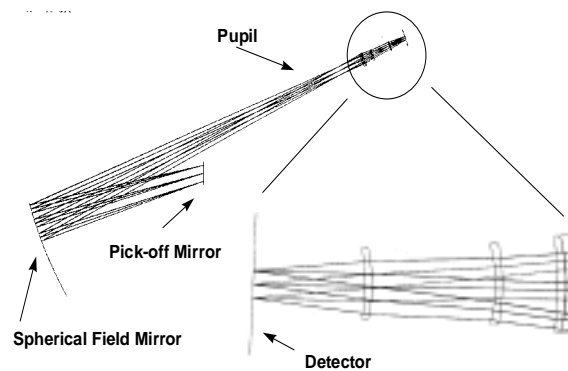


Figure 3.4. Optical layout of the MIR camera (left) and spot diagram for various points in the field.

The MIR spectrograph is a single aperture spectrometer with a spectral resolution of 1000 and a spectral range of 5.8 to 21 microns. The entrance slit is 0.75 arcsecond wide and 2 arcseconds long. The spectral range is divided into two bands, 5.8 to 13.1 and 12.75 to 21.2 microns. A cross disperser is used for the first band. Spectra are formed on the detector of the MIR camera. The grism/cross disperser units are mounted on the camera filter wheel.

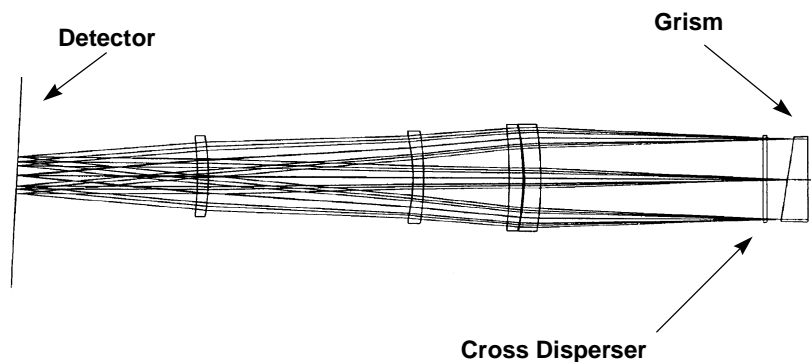


Figure 3.5. Optical layout of the MIR spectrograph. The dispersed beam is fed into the MIR camera to economize a dedicated detector.

3.6 Detectors

Detector type

Indium Antimonide (InSb) is the detector type because of its low dark current and low readout noise characteristics. A low dark current is critical to the overall sensitivity of the observatory and should be negligible compared to the zodiacal background. InSb detectors must be operated at about 35 K. Mercury-cadmium-telluride (HgCdTe) has the advantage of being able to work at higher temperature (70K) up to about 3 microns (beyond that they also must be cooled to about 35K) but has a much higher dark current. Since it is possible to cool down the ISIM passively to about 30K, InSb is the obvious choice for the entire NIR spectral range. In addition, InSb's response extends to the visible, a feature which can be very advantageous for both science and guiding, and eliminates the need for additional visible detectors. It was felt that using the same detector for all NIR cameras and the spectrometer would simplify the design process and lower procurement costs.

The MIR detector is an Si:As impurity band device. Among current 2-dimensional near infrared detectors we have selected the Impurity Band Conduction (IBC) array which offers relatively high quantum efficiency and good spectral coverage from 5.5 to 30 microns. Si:As detectors need to be cooled to about 6K and thus require active cooling.

The main characteristics of these two types of detectors are given in the table. Since the detector dark current in the currently available detectors is somewhat higher than desired compared to the natural zodiacal background but is not yet fundamentally limited, we have assumed that improvements by at least a factor of 2 to 5 over the next five years could be made in this area provided there is sufficient support for dedicated development effort.

Table 3.2. Main characteristics of the detectors

<i>Parameter</i>	<i>InSb</i>	<i>Si:As</i>
Wavelength coverage (μm)	0.6 to 5.3	5 to 30
Dark current (electron/s)	0.02*	10*
Readout noise (electrons)	15*	30*
Multi-sampled readout noise	4	8*
Full well	100,000	300,000
Temperature (deg K)	30K	6 K
Read out time ($\mu\text{s}/\text{pixel}$)	3	3

*assuming improvement by a factor of 2 to 5 over what is currently measurable in current state-of-the-art detectors

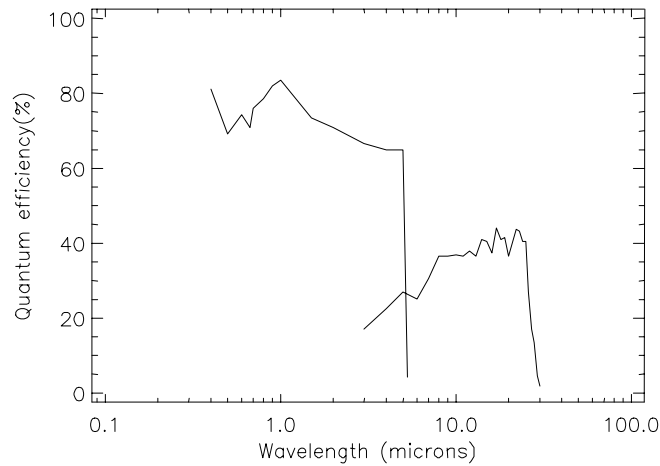


Figure 3.6. Typical quantum efficiency of the InSb and Si:As array (courtesy of SBRC)

Because of the very large format required, the NIR detectors are made of a mosaic of 1k x 1k arrays arranged in sets of 4. This is both to reduce cost (no supplemental development effort beyond existing technology, higher yield and easier rework during the testing phase) and to minimize the impact of the guiding function on science data. The Si:As array is made of 1k x 1k array using the same footprint as the NIR elemental arrays.

The cables for each 2k x 2k module (four SCAs) contain 148 leads: 32 output leads per SCA, and 9 clocks and 11 biases shared among the 4 SCAs. To minimize generation of heat in the SIM, the arrays' driver electronics (buffer amplifiers, voltage regulator for the biases and timing generators) are located outside of the ISIM on the OTA/SSM truss, in a 60K environment.

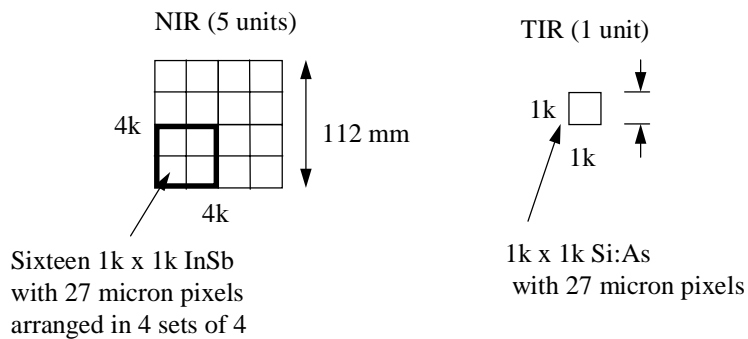


Figure 3.7. Detector configuration. Because of practical limitations in detector size and to minimize cost the NIR detectors are made of a mosaic of sixteen 1k x 1k arrays arranged in sets of 4. Gaps are minimal.

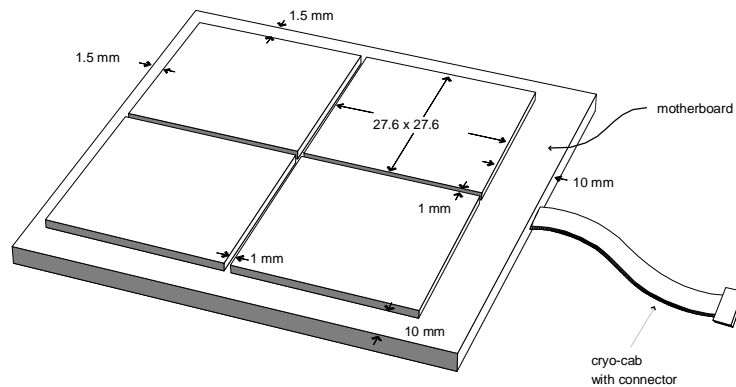


Figure 3.8. Schematic view of one of four 2k x 2k assemblies composing each of the NIR camera detector assemblies.

Cosmic rays

Cosmic rays have two effects on detectors: i) long-term exposure to radiation can damage the detectors, and ii) individual hits mask pixels for a given integration.

Based on ISO and COBE experience, InSb detectors appear to stand very well against radiation damage. Lab experiments for SIRTf have also shown that exposure to a lifetime dose of 1.3 krad does not show any long term degradation. For 5 years at L2, the radiation dose is about 2 krads and this should be no problem. Silicon detectors may be more sensitive, and are currently undergoing tests.

Direct hits can temporarily fill up pixel wells, but pixels recover quickly following reset and can be used for the next integration. The solution is to decompose observations into several exposures, and reject the affected pixels in software. At L2 the cosmic rate is 1 proton per cm^2 per second and 27-micron pixels will thus get hit every 14000 seconds. Allowing 10% of the pixels to be hit for each sub exposure, and allowing a margin for inclined rays, we have adopted a subexposure integration time of 1000 seconds. As a measure of safety, and to allow operations to resume one day after a solar flare, we have included a minimum shielding of $5\text{g}/\text{cm}^2$ to absorb the low energy protons ($< 70\text{ MeV}$). No attempt is made to shield against the high energy galactic protons since real improvements would require impractical shielding against multi GeV protons. Moreover, the high energy proton flux is relatively modest. Since grazing incidence protons affect many pixels, shielding is limited to a cylinder surrounding the detector. The shield is made of 2cm thick aluminum and has a mass of about 2.5kg per detector.

Detector readout

Unlike CCDs, InSb arrays can be read nondestructively. In order to reduce the readout noise, the entire array is read multiple times at the start and end of an integration. The arrays are reset before the very first read and not again until before the very first read of the next integration period. This figure shows the reduction of readout noise as a function of the number of reads. As expected, readout noise is reduced by the inverse square root of the number of reads, but past 30 readouts or so, reduction tends to plateau.

We have adopted the number of 32 as being a good compromise between reduction of readout noise and the penalty paid for storage of the frames. By averaging the first 32 reads and subtracting the result from the average of the final 32 reads, one reduces the effects of readout noise by about a factor of 5 from 30 rms noise for a single read to about 6e RMS noise.

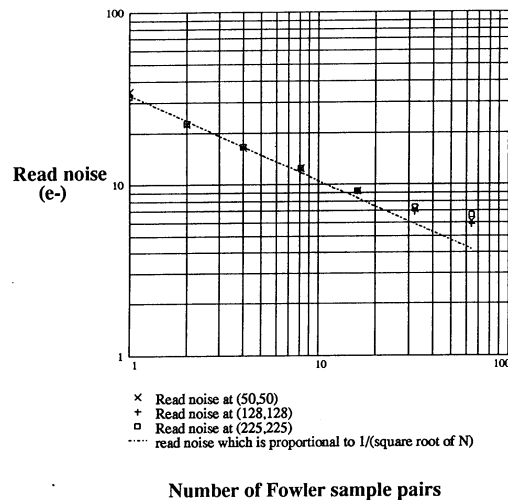


Figure 3.9. Reduction of readout noise by multiple sampling. The reduction follows the inverse square root of the number of reads up to about 32 sampling.

It takes about 3 microseconds per pixel to switch the pixel output transistor onto the bus and stabilize the signal before clamping it prior to the A/D conversion. To speed up the readouts, the 1024 x 1024 chips have 16 independent readout buses and clamping circuits, so that each 512 x 128 area is read

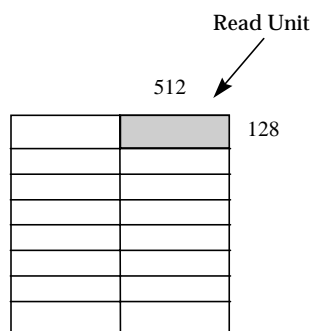


Figure 3.10. Each 1k x 1k chip is read by 512 x 128 subareas so as to reduce the readout time.

independently. With reads at the beginning and 32 at the end of each frame, the total readout time is thus about 12s. This represents a 1.2% duty cycle for a nominal 1000 second exposure. The readouts are staggered in time to minimize heat loads. There are 4 A/D per chip. The average power consumption is 2mW per chip.

3.7 Structures and mechanisms

Optical bench

The optical bench is a truss structure made of beryllium with mounting brackets for the optical components and mechanisms, which are also made of beryllium. Beryllium has a very high intrinsic stiffness, thus minimizing mass. Since all mirrors are also made of beryllium, an optical bench made of the same material guarantees that the optical system will remain in focus to the first order independently of the overall temperature. It also eliminates the need for differential expansion devices, normally installed in optical systems to avoid stressing the optical components during the cool down period. The overall view of the optical bench is shown in Figure 3.11. It is of prismatic shape, 2 x 2 meters at the top and 2.5 meters in height.

The enclosure serves as physical, straylight, and contamination protection for the instrument. It also forms a thermal barrier against radiation from the back of the sunshield. It is composed of a light frame supporting lightweight panels. It is wrapped in MLI and surrounded by a light thermal shield. The enclosure has no physical contact with the optical bench and is supported by the OTA attachments fixtures used for the optical bench.

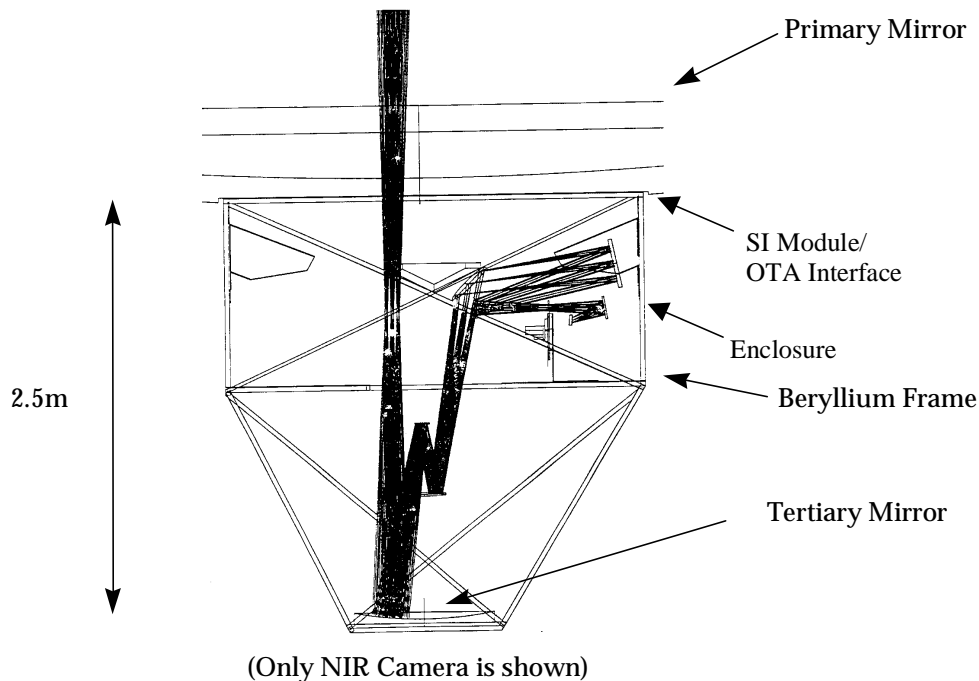


Figure 3.11. Overall view of the science instrument module.

The optical bench is attached to the OTA with 3 sets of bipod flexures providing a determinant kinematic mount.

Filter wheels

The filter wheels for the cameras and the grism wheels for the spectrographs are of the same design, and differ only by the size and shape of the wheel. The wheel is driven by a torque motor operating in direct drive, a solution which was developed for the SIRTf program. This has the advantage of mechanical simplicity, high positional accuracy, and minimizes heat dissipation for cryogenics applications. An encoder is used for position readout.

Cold stop

The cold stop insertion mechanism uses two orthogonally placed stepper motors which provide up to 10 mm translation in x and y for accurate placement of the cold stop.

Focusing mechanisms

Each camera and spectrometer can be individually focused. In the case of the NIR camera and NIR spectrograph, focusing is done by displacing the small convex mirror in the Offner relays. For the MIR camera/spectrograph focusing is obtained by moving the second lens of the camera. These focusing optical elements are mounted on a single axis stage driven by a redundant stepper motor, and equipped with position sensors. This is important for simplifying I&T, easing launch constraints for the efficient implementation of the new WFC system.

Fast steering mirror

The two redundant fast steering mirrors are mounted back to back on a flip mechanism. The flip mechanism uses a spring loaded “one-time-only” detent system for the highest reliability. After a 180 degree rotation the backup mirror is located at exactly the same place as the original mirror.

Enclosure

The enclosure serves as physical, straylight and contamination protection for the instrument. It forms also a thermal barrier against radiation from the back of the sunshield. It is composed of a light frame supporting lightweight panels. As explained in section 4.11, it is wrapped in MLI and surrounded by a light thermal shield. The enclosure has no physical contact with the optical bench and is supported by the OTA attachment fixtures used for the optical bench.

3.8 Thermal system

The optical bench and optical components must be at less than 80 K in order to reduce the emissivity of optical components and other surfaces seen by the NIR detector to a negligible level. In addition, it is advantageous for the ISIM to be at less than 30 K so that the InSb may be operated without extra cooling. This is the solution that has been adopted. Since the back side of the sun shield (which is at about 60 K and with a high emissivity) offers a large view factor to ISIM, radiative isolation of the optical bench is required. The optical bench is first surrounded by a structural enclosure with no physical contact except at the thermally isolated attachments to the OTA. This enclosure protects all

sides of the optical bench, except the side opposite the sun shield, where the enclosure is replaced by a large radiator (about 4 square meters) connected to the optical bench. The inside of that enclosure is covered with a gold kapton layer, and the outside is wrapped in multilayer insulation (MLI). The enclosure is itself surrounded with a shield, also wrapped with MLI, which is radiatively cooled by a radiator to expel parasitic heat received from the sunshield.

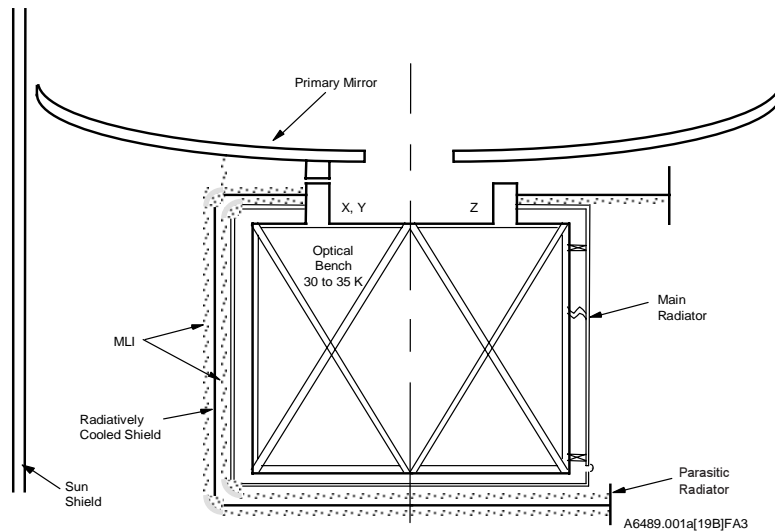


Figure 3.12. Schematic of the thermal system

Based on the heat input from detectors and parasitics indicated in this table, and assuming that the back of the sun shield is at 60K, and that there is a negligible heat input from the OTA (both radiatively and conductively), a simplified thermal model shows that the optical bench will be at about 31.4K. With the substantial thermal protection adopted, the optical bench temperature is relatively unaffected by small changes in the sunshield temperature. It would be at 30.4K for a sun shield temperature of 50K, and at 32.7K for a shield temperature of 70K. The optical bench temperature is also relatively unaffected by a change in amount of heat generated inside ISIM. The optical bench temperature would rise to only 33.0K if heat dissipation were to increase by 50 mW (from 173 mW to 223 mW).

Table 3.3. Heat loads and parasitics

Source	Heat dissipation (mW)
NIR detectors	160
MIR detector	2
FSM	7
Mechanisms	<1 average
DM	<1
Multi-mirror system	<1
Cable parasitics	5
OTA/ISIM parasitics	5
Cryo system heat exchanger	Negligible
Subtotal	173
Radiation in form sunshield (60K)	36
Total	216
Radiation out from radiator	216

3.9 Cryogenic system for the MIR instrument

The near infrared camera and detectors are operated at the nominal 30K to which the ISIM can be driven passively. At this temperature the thermal emission of the optics and the detector dark current are negligible. This is not the case in the mid-infrared. Critical elements of the MIR camera and spectrometer must be cooled actively, the filters and cold stop down to about 15 degrees and the detector down to at least 6-8K.

Two cooling possibilities exist for the MIR instrument: cryostat or mechanical cooling. In a 30 K environment a cryostat can be made to last 10 years without excessive volume and mass.

Solid hydrogen is preferable to liquid helium as a cryogen because it has about 10 times the cooling power for the same mass. The mass required for 5mW of cooling power at 6.5 K for 10 years is about 50 kg. 20mW cooling would require about 100 kg of solid He. This is about 2 to 5 times more mass than that of a mechanical cooler, but a LH2 cryostat uses existing technology and no development is required. Reliability is also considered higher. Figure xx shows a preliminary design for such a cryostat. The instrument optical elements are outside of the cryostat and cooled with thermal straps.

Among the possible cryo-cooling systems (H2 sorption cooler, Stirling-cycle, VM-cycle, reverse Brayton-cycle) we have selected, for the purpose of this study, the reverse Brayton-cycle cooler because of its moderate power requirement (60 W), low mass (less than 10 kg), high reliability, long life, and very low level of vibration. As opposed to Stirling-cycle reciprocating mechanical coolers, Brayton-cycle systems use turbines for both compression and expansion. The turbines which use gas bearings are vibration free and the absence of continuously rubbing parts eliminates failure by wear. In addition, the individual components are small, easy to integrate, and the heat generating turbo-

compressor is ideally suited for use with a radiatively cooled heat sink. The fluid is helium in gas form. The reverse Brayton-cycle cooler proposed for our application is based on a US Air Force/ NASA development program under way at Creare. A unit capable of 5 mW of cooling power at 6K could be ready for flight as early as year 2000.

The reverse Brayton-cycle cooler consists of a turbo-compressor and a counterflow heat exchanger located in the SSM, a low temperature radiator heat intercept located outside of the ISIM, and a turbo-expander and cold counterflow heat exchanger located in the ISIM.

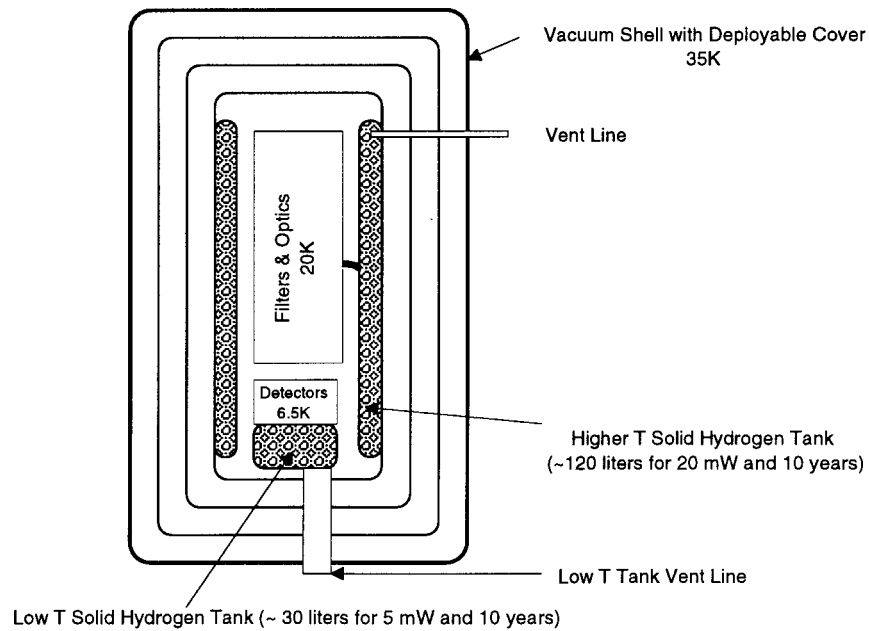


Figure 3.13. Schematic view of a 6.5 K solid hydrogen cryostat for the MIR instrument

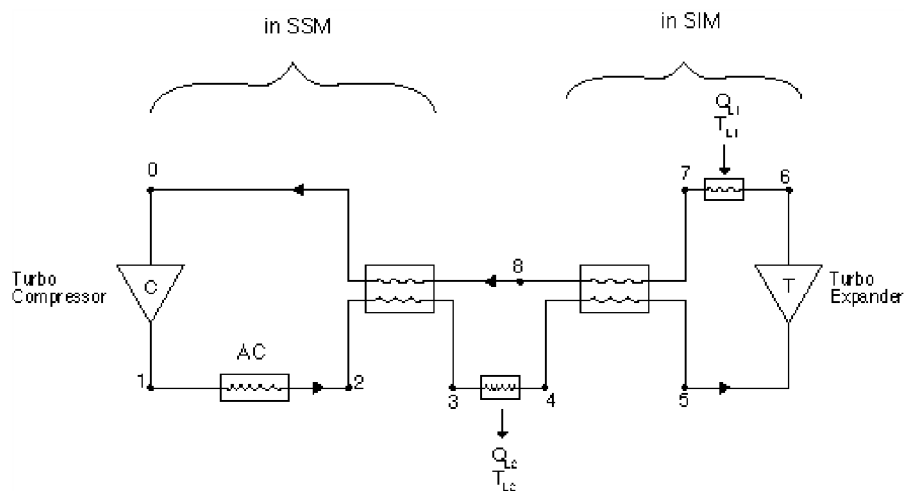


Figure 3.14. Schematic layout of the Brayton-cycle cooler system proposed for the thermal-infrared camera and spectrograph.

The compressor has a 3 mm shaft rotating nominally at 5000Hz (300 000 rpm) in an 80 mm diameter by 100 mm length housing. It is mounted directly on a radiator which expels the compressor heat (around 50 W). This radiator, which is at about 220K, is mounted on the SSM facing away from the sun. The control electronics consists primarily of a three phase inverter which is located with other electronics in the SSM. The warm heat exchanger occupies a cylindrical volume of approximately 150 mm in diameter by 100 mm long and is mounted on the warm radiator proximate to the turbo-compressor.

The cooling fluid in-going and return flow runs through flexible tubing about 12 mm in diameter, between the SSM and the cold end of the extended structure. Parasitic heat is intercepted by a 1/2 square meter radiator operating at about 55 K, which is mounted on the cold end of the extended structure, facing away from the ISIM and from the primary mirror. This radiator also supports the cold heat exchanger which is similar in size to the warm side exchanger, and the turbo-expander which is approximately 60 mm in diameter by 100 mm long.

A thin tubing, about 10 mm in diameter, runs from the expander to two 6K heat exchangers near the mid-infrared channel, and then back to the cold heat exchanger. The 6K heat exchangers, one for the detectors and another for the filter wheel, are simply made of a 25 mm long copper block surrounding the tubing.

The detector and filter wheel are connected to these 6K heat exchangers with a flexible cold thermal strap, made of 1 mm braided copper wire. The fittings on both ends of the detector thermal strap are electrically isolated from their mating surfaces with a thin dielectric material. The thermal strap is then grounded with a wire that is taken out to the preferred instrument ground, thus reducing ground loop noise by eliminating capacitance to ground.

3.10 Calibration of Instruments

The relative sensitivity of the detectors as a function of field position ("flat fielding") will be determined on an overall scale using sky flats. At 6 microns, a sky flat can be obtained in about 20 minutes with a signal to noise ratio of 100 using the zodiacal emission at 45 degree from the ecliptic.

More frequent calibration of the detectors on a pixel-to-pixel scale will be performed using a continuum lamp which provides relatively smooth illumination. This calibration lamp is mounted on the edge of the secondary mirror for filling the science instrument optics in a manner equivalent to a sky source. The source is a tungsten halogen lamp with a quartz case. The quartz case is transparent to the NIR spectral band and allows the NIR instruments to be illuminated with the flux of the tungsten filament at a temperature of 2800 C which peaks around 3 microns. The quartz case, which blocks all radiation beyond about 5 microns, will be the only source seen by the mid-infrared instruments. With a temperature of about 300 K, the quartz case radiation will peak at around 10 microns.

Wavelength calibration of the spectrometer modes will be determined on the ground. Since the dispersion of the grisms is expected to remain stable, no on-board line source is required.

Detector dark current will be measured using a blank filter in the filter wheel. For the MIR camera this blank filter has a silvered back to reduce thermal emission.

Flux calibration will be made using existing standard sources (UKIRT, NICMOS, ISO).

3.11 Instrument operational modes

To minimize cost, from both the hardware and commanding software points of view, operational modes have been kept at a strict minimum. This is also justified by a scientific program which emphasizes surveys and pointed observations for only a limited number of types of targets.

NIR camera

The near infrared camera has three modes:

1. The *regular imaging mode* in which a particular filter is selected, and the observation is executed with quick multiple readouts at the beginning and end. Long observations are broken up in sequences of 1000 seconds sub-exposures for cosmic ray removal.
2. The *bright object exclusion mode* in which a short exposure is taken prior to the observation itself to determine the position of potential bright objects in the field. This is to prevent remanence or possible damage. Pixels where bright objects fall are identified and then excluded from the read-outs of the ensuing exposures.
3. The *guiding mode* in which a short exposure is taken prior to the observation to identify an adequate guide star and determine which of the 1k x 1k sub-chip will be dedicated to guiding. A portion of that chip surrounding the guide star will then be read at fast rate (30 to 100 Hz) and the rest of the chip will not be read. Meanwhile, the other chips in that camera are read normally at the rate desired for the scientific application (nominally 1000 seconds).

The four sub-cameras are treated as fully independent and can each be in a different mode. This is both for simplicity of the commanding and for ensuring complete redundancy. Because of the very large field of the cameras and the good absolute pointing of the attitude control system (around 2 arcseconds), blind pointing is sufficient and no target acquisition capability is provided. This implies, however that there will be no guarantee that a target can be placed on the same camera pixel on a second visit.

NIR multi-slit spectrograph

The near infrared multi-slit spectrograph has four modes:

1. The *regular spectrographic mode* in which a pre-selected set of micro-mirrors “slits” are turned on, and the spectrographic observation is executed with quick multiple readouts at the beginning and end. Long observations are broken up in sequences of 1000 second sub-exposures for cosmic ray removal.

2. The *imaging mode* in which all micro-mirrors are turned on and a filter is used instead of the spectrographic dispersers. The observation proceeds as in the spectrographic mode described above, albeit creating an image of the entire field.
3. The *acquisition peak up mode* in which a previously obtained image of the field is used to select the objects to be observed and determine which micro-mirrors will be turned on. The brightest target in the multi-object list is used for autonomous acquisition, which consists in locating that target at the desired “open slit” by a spiral search executed by the fast steering mirror under the control of the guiding system. The observatory roll control accuracy is sufficient to guarantee that the other selected targets in the field will also be placed at their preselected position.
4. The *point and shoot spectrographic mode* in which the selection of targets to be observed and the determination of the micro mirrors to be turned on is autonomously performed on board. This selection uses an image obtained in the imaging mode defined above and is performed by an algorithm which determines the objects to be observed as a function of specific target brightness and angular separation criteria. This mode will be especially useful for performing “parallel surveys,” i.e. when the spectrograph is not the primary instrument.

Mid-infrared camera/spectrograph

The mid-infrared camera/spectrograph has three modes:

1. The *imaging mode* where the instrument is used as a camera with preselection of filters and the observation is executed with quick multiple readouts at the beginning and end as explained for the near infrared camera. As for the NIR camera, blind pointing is sufficient because of the large field.
2. The *spectrographic mode* in which a target is located on the spectrographic slit following peak up as explained below, and the observation proceeds with multiple subexposures as for the imaging mode.
3. The *peak-up mode* used for target acquisition in the spectrograph slit. This is accomplished by a spiral search executed by the fast steering mirror under the control of the guiding system.

3.12 Science and engineering data

Science data

For each observation a data rate required for the primary and the parallel observations can be computed by considering the integration times, efficiency factors (10 per cent engineering/calibration loss), wobbling time during repointing (18 minutes deadtime), detector deadtime (36 seconds per frame due to initialization and readout). The Design Reference Mission (DRM) allows one to derive the mean data rate during the mission. A sustained downlink rate not less than 800 kbit/s seems to be required. The local storage should be in the 30-50 Gbyte range in order not to introduce too heavy scheduling constraints. The on-board computing power should be in the range 50-300 Mflops.

Note that since each science frame is actually obtained from several tens of readouts (e.g. 60) an on-board fast memory of about 10 Gbytes is also required. Increasing the on-board computing power can reduce the fast memory requirement.

Engineering data

The engineering data for housekeeping and mechanism position monitoring include about 100 parameters as listed in Table 3.4.

Table 3.4 List of engineering parameters

Parameter	Number
Mechanism position	16
Fast steering mirror (2 units)	8
Detector temperature	6
Optics bench and optics temperature	30
Mechanism temperature	16
Cryo system turbine and heat exchanger temperatures	6
Control electronics temperatures	10
Vacuum gage	1
Total data points	93

3.13 Control electronics and power supply

All control electronics for ISIM are located in the warm SSM. This is to avoid unnecessary heat load in ISIM, but also to allow the use of ordinary “warm” electronics components. The electronics box communicates directly with the SSM. There are two redundant control electronics boxes and wiring, side 1 and side 2, both having full control and communication capability with all sensors and mechanisms. To reduce parts counts and increase reliability, there is no cross strapping between side 1 and side 2. A schematic block diagram of the control electronics is shown in the figure.

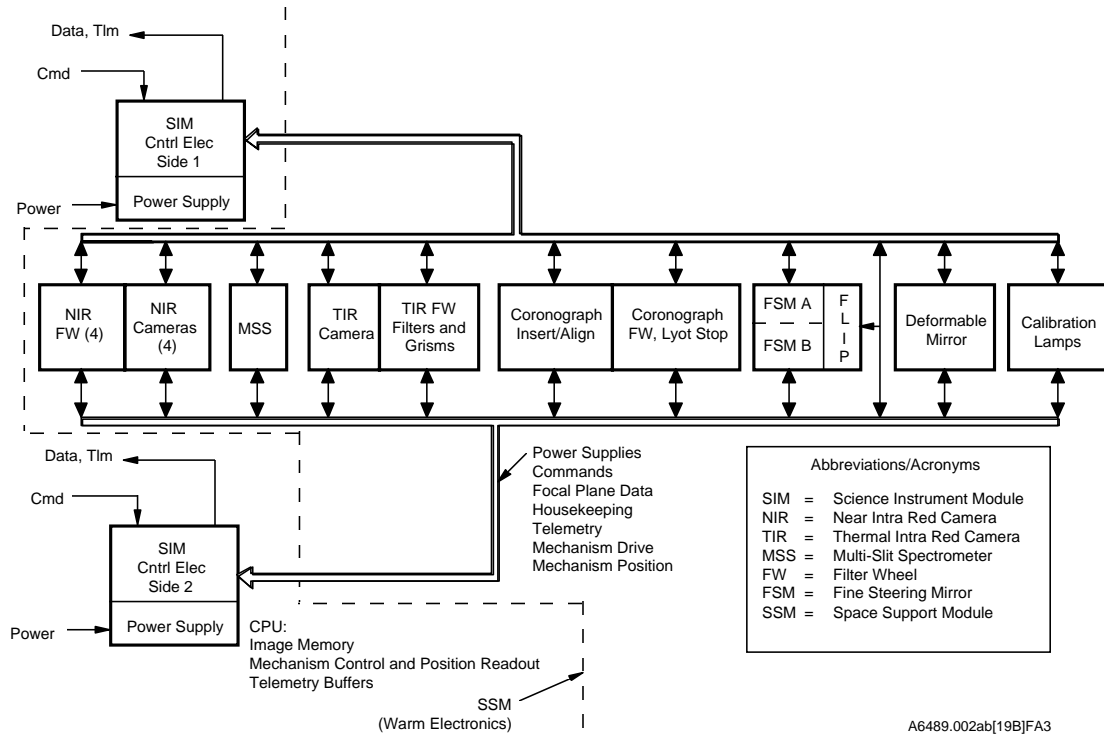


Figure 3.14. Control schematics

The power estimate for the science module is shown in table 3.5.

Table 3.5. Power estimate

<i>Item</i>	<i>Power (W)</i>
Inside ISIM	
Detectors	0.160
Multi-mirror syst	NA
Mechanisms	0.010
FSM&DM	
Total ISIM	0.170
Located in SSM	
Main electronics	100
Power supplies	20
Cryocooler	60
Total SSM	180

3.14 ISIM mass estimate

The mass estimate for the ISIM is summarized in Table 3.6.

Table 3.6. Mass summary

<i>Subsystem</i>	<i>Mass (kg)</i>
Structure	127
Optics	23.2
Detectors	4.4
Electronics and cabling	66
Mechanisms	23.5
Cooling system	19
Miscellaneous	65.8
Contingency	98.7
Total	371.5

4. SPACECRAFT SUPPORT MODULE

The spacecraft support module (SSM) supplies the supporting functions of the observatory: power, communication, data handling, attitude control, sun shielding, station keeping, and momentum dumping. It is composed of three main elements: the spacecraft bus, the sunshield and the isolation truss (see Figure 4.1). The spacecraft bus, located on the warm side of the sunshield and connected to the OTA via an isolation truss made of gamma-alumina composite, has an extremely high stiffness/thermal conductivity ratio.

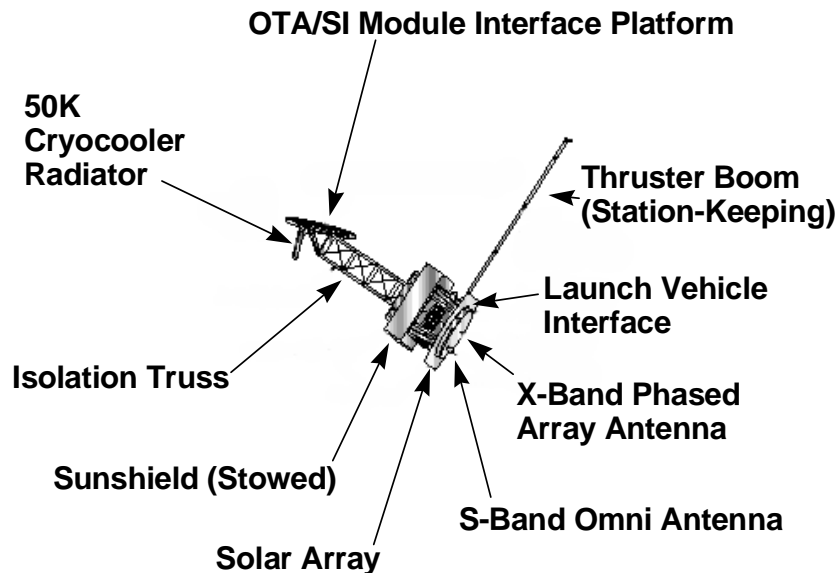


Figure 4.1. Spacecraft Support Module sunshields shown stowed

The SSM also provides the structural interface between the launch vehicle and the OTA for launch. The isolation truss deploys on orbit to separate and reorient the cold OTA (and attached ISIM) from the warm SSM structure, providing conductive heat isolation to these cold segments. The sunshield deploys on orbit to provide radiative isolation for the cold components from direct solar radiation and from the warm SSM.

A closeup view of the SSM is shown in Figure 4.2.

4.1 The spacecraft bus

The spacecraft bus structure is a twelve-sided cylindrical structure, approximately 2 meters long and 1.7 meters in diameter. The aft end of this structure interfaces to the launch vehicle via a Marman clamp payload attach fitting. Load is transferred from the OTA for launch along its length,

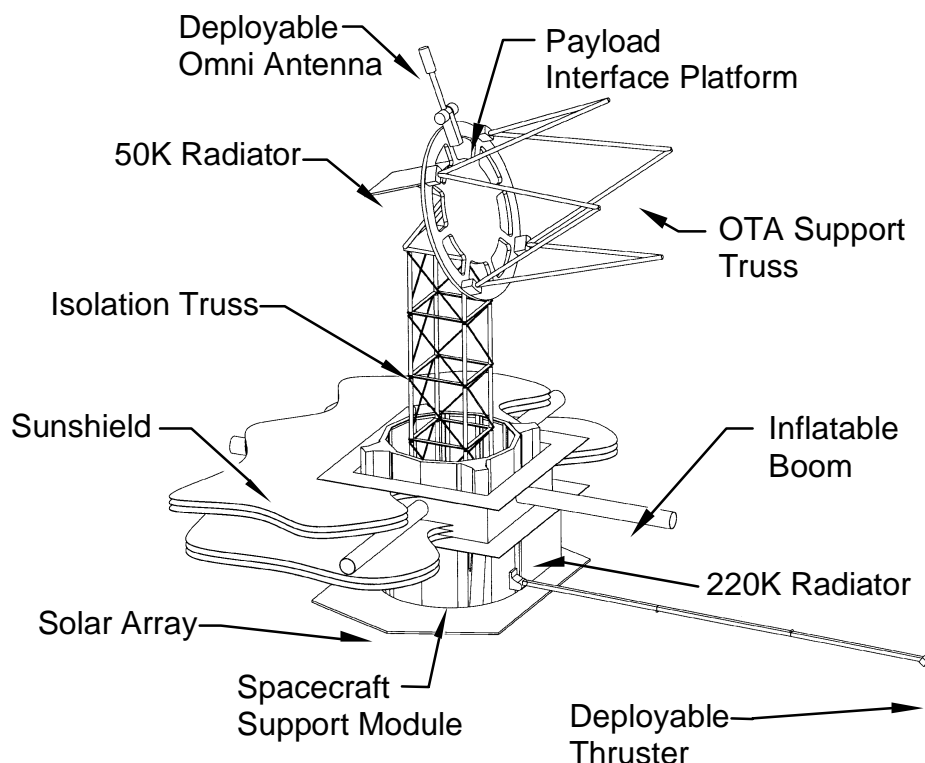


Figure 4.2. Closeup view of the SSM

transitioning through four tapered longerons with hardpoints/launch locks at the forward end of the SSM through the Payload Interface Platform, to eight struts which interface with the aft end of the OTA.

The spacecraft bus houses the majority of the various spacecraft subsystem components in four main groups. On the side panels are mounted the components which perform spacecraft housekeeping, plus the ISIM and OTA electronics. These include a Brayton cooler for the instruments, two batteries, and the ACS, Electrical Power Subsystem and Command and Data Handling electronics. The reaction wheel module, incorporating the four reaction wheels in one assembly with the associated electronics, is mounted to an internal, centrally located bulkhead (components can be mounted with vibration isolation if required). Located at the end of the bus are the propulsion module, including Reaction Control System propellant and pressurant, valving and thrusters, communications electronics, and X-band phased array and S-band omni antennas. At the forward end of the bus, an optical bench provides a stable platform for gyros and star trackers. Additional, body-mounted components include the aft-mounted fixed solar array, side-mounted 220K radiator, and the deployable RCS thruster. The SSM is shown partially exploded in Figure 4.3.

The spacecraft bus is maintained at approximately room temperature using standard thermal control techniques, including multilayer insulation for the majority of surfaces, with thermal control paint used adjacent to deployables and separating surfaces (to avoid blanket interference with separations). Thermal louvers are used to maintain tighter control of critical box and battery temperatures.

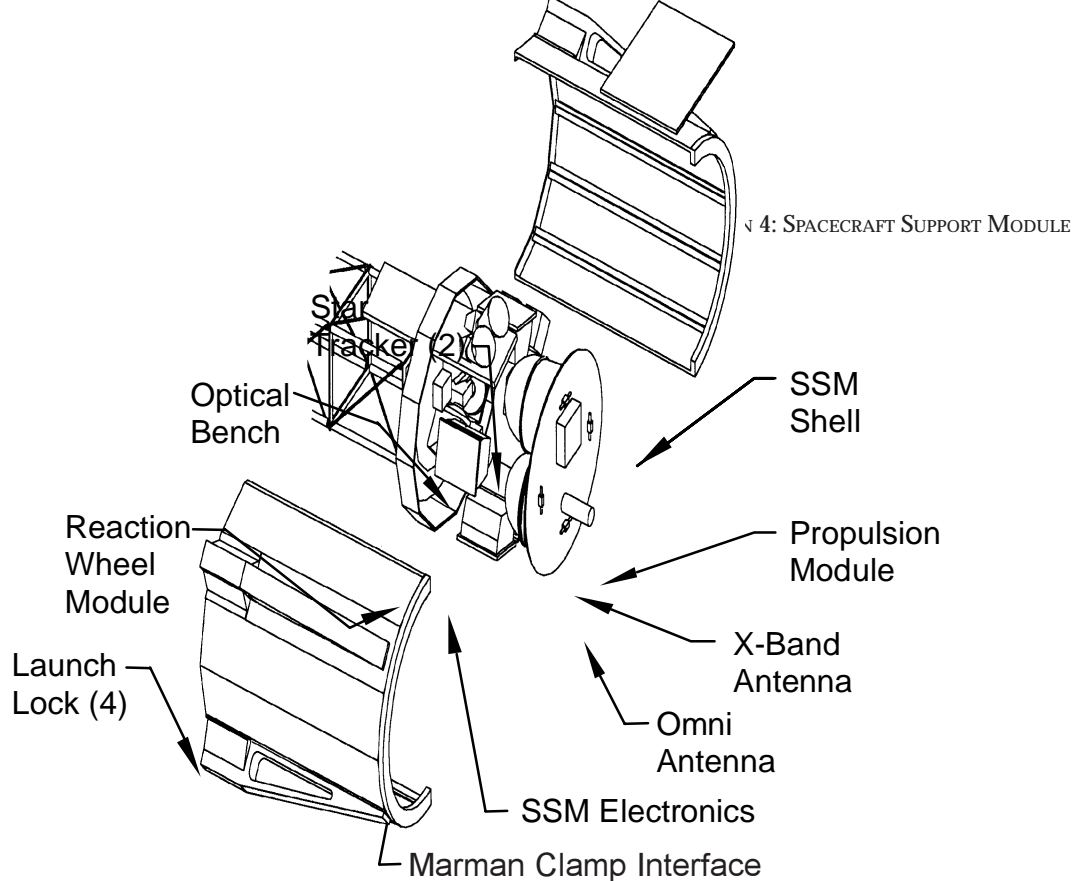


Figure 4.3. Spacecraft bus

The SSM structure is composed generally of carbon-fiber-reinforced polymer components tailored to stiffness and strength requirements. Highly stressed areas, such as the launch vehicle interface and launch locks, are metallic.

The sunshield is housed for launch outside of the bus structure, in a square “annulus.” Internal to the bus are mounted the pressurant and valving for the sunshield deployment system (described below). Mounted to the forward end of the bus internal bulkhead is the aft end of the isolation truss. For launch, the entire deployable segment of the truss is stored within the volume of the bus.

4.2 The isolation truss

The Isolation Truss assembly comprises a four-bay deployable isolation truss, the payload interface platform, and the OTA support truss. These components are designed to minimize conductive heat transfer from the spacecraft bus to the OTA, while meeting operational stiffness requirements. The tubular elements of the trusses are gamma-alumina composite, which has an extremely high stiffness/thermal conductivity ratio.

The isolation truss deploys to provide a separation of 2.9 meters from the forward end of the spacecraft bus to the center of the payload interface platform. It carries all of the harnesses and plumbing which run between the SSM and OTA/ISIM. Deployment energy is via stored spring energy within the hinge joints. The deployment rate of the truss is controlled by a lanyard/drive motor system which limits the rate of energy release by the hinge springs.

The payload interface platform rotates 70° from its launch-axis orientation to its operational fixed configuration on orbit. It rotates via stored spring energy of an unfolding deployment strut which forms a four-bar linkage with the platform and the forward bay of the isolation truss. Attached to the aft face of the platform is a 50K cryocooler radiator, mounted perpendicular to its face. The platform is a composite, stiffened plate. Mounted to it are four metallic hardpoints which form the launch interface to the SSM. These also provide the mounting points for the eight struts of the OTA support truss.

The OTA support truss transfers the launch loads of the OTA to the SSM via eight composite tubes in an octapod arrangement. These surround but do not interface directly with the ISIM (which is linked structurally directly to the OTA). The truss provides a separation of 2.5 meters from the OTA front surface to the payload interface platform.

4.3 The Sunshield

The sunshield protects the OTA and ISIM from the sun. It comprises six parallel membranes arranged in a diamond shape with deployed dimensions of 32.8 meters in length, and 14.2 meters in width, as shown in Figure 4.4. The shape is tailored to provide full shielding of the cold components from sunlight over the operational ranges of pitch and roll for NGST. Its center of pressure is aligned with the system center of mass for the nominal orientation normal to the sun. The membranes are composed of Kapton film with coatings tailored to the emissivity and absorptivity requirements of each layer, as well as environmental requirements.

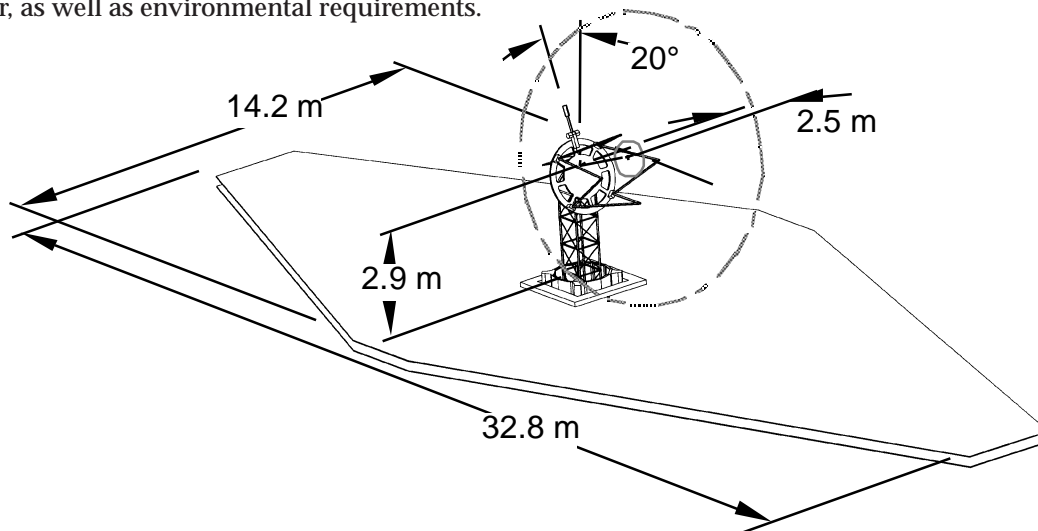


Figure 4.4. Dimensions of the sunshield

The structural backbone of the sunshield is four axially-extendible mechanical or inflatable booms arranged in a cruciform pattern, which deploy and support the film layers (Figure 4.5). The booms are sandwiched within the film stack, with three membranes on either side for symmetry. When stowed, the shield is packaged in the central housing: the membranes are Z-folded in two orthogonal directions. The inner folds of each stowed film layer are attached to the interior of the central housing with Velcro, which secures the layers for launch, and prevents residual air or film strain from prematurely deploying the film.

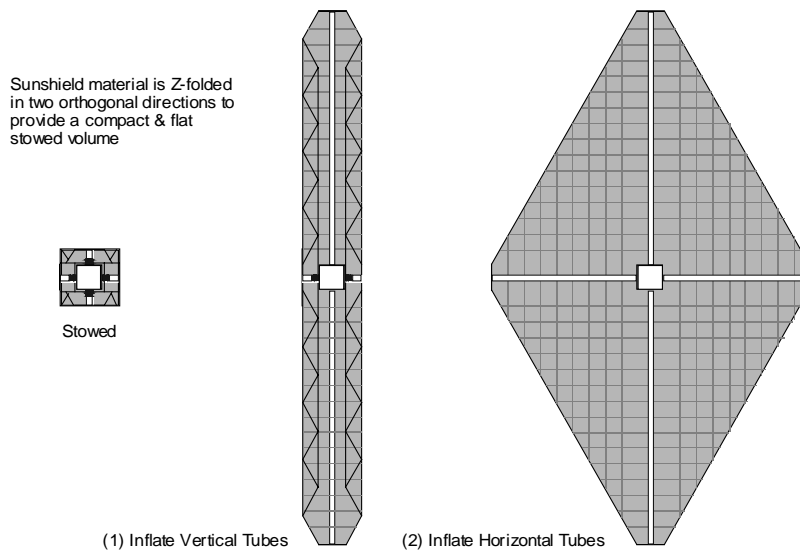


Figure 4.5. Inflatable sunshield. Orthogonal-bi-fold unfolding sequence.

At the tip of each boom is a trapezoidal plate which supports each layer via a constant-force spring-tensioned suspension system. The plates support the film for launch, maintain the required separation of the layers, and transfer the deployment forces from the boom to the layers. Extension of the booms pulls the Velcro attachments free one at a time, to provide controlled deployment of the layers. Boom deployment occurs in a two step sequence, with opposing booms fully extending, followed by deployment of the second pair of booms. If inflatable booms are used, then the booms are rigidized after deployment and internal pressure is not required to maintain the stability and stiffness requirements of the booms.

The sunshield is sized to allow the entire observatory to be tilted $\pm 25^\circ$ with respect to the sun direction as shown in Figure 4.6.

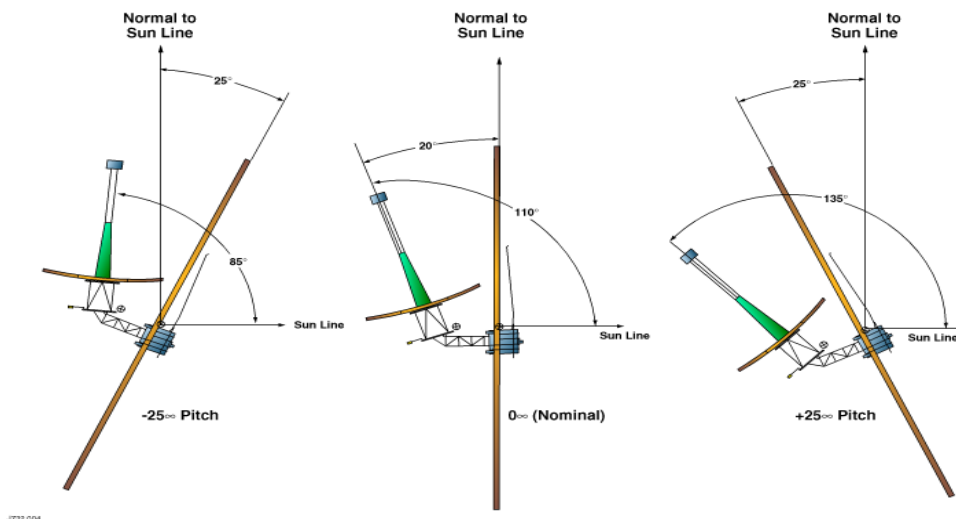


Figure 4.6.

4.4 Power Subsystem

The Power Subsystem is a direct energy transfer system consisting of solar array, batteries, and power system electronics. The Power Subsystem provides the major electrical functions of power control, energy storage, and distribution of power to the observatory loads. Power which is generated in the solar array is supplied directly to the observatory loads. Two 30 amp-hour batteries provide observatory power during launch.

The estimate of the power required for the entire observatory is shown in Table 4.1.

Table 4.1. Power estimate

<i>Item</i>	<i>Mean Power (W)</i>
Space Support Module (SSM)	113
Attitude Control Electronics	15
Active Vibration Isolation	76
Command & Data Handling Subsystem	147
Communication/RF	28
Power Supply Electronics	15
Electrical RSN	30
Thermal Control	50
SSM Total Mean Power	474
Integrated Science Instrument Module (ISIM)	180
Optical Telescope Assembly (OTA)	0
Harness Loss	36
Battery Charging Load (@ 100 C)	16
Observatory Total Mean Load	706
Solar Array Mean Power	900
Array Power Margin	194

Solar Array

The solar array uses multi-junction cells. The multi-junction (MJ) cell is more efficient, weighs less, and has lower system costs than the gallium arsenide (GaAs) or silicon (Si) cells (Table 4.2).

Table 4.2. Solar cell trade study. These data are generated for S/C load of 800W, operating @ 80°C.

	<i>Silicon</i>	<i>Gallium-Arsenide</i>	<i>Multi-Junction</i>
Efficiency (%)	14.8	18.5	24
EOL Power (W/m ²)	113	176	214
Size (m ²)	9.4	6.0	4.95
Weight (kg)	47	30	25

The end-of-life (EOL) power required from the solar array is 1192 watts, requiring about 6 m² of solar array. The corresponding weight is estimated at 30 kg.

Battery

The batteries are required for launch and bus regulation only. Two 30 amp-hour batteries are required to support the 400 watt loads for 2 hours from the prelaunch phase until the solar array acquires sun. The maximum depth-of-discharge (DoD) for these batteries is 60%.

During operation, the batteries provide a more reliable power system. The battery voltage is used to clamp the solar array operating voltage. The battery provides bus stability by acting as a large capacitor to protect the spacecraft bus from voltage transients.

The battery uses lithium ion cells which provide higher specific energy, low cycle life, and weigh less compared to the other cells, such as NiCd and NiH₂. For one 30 amp-hour battery, approximately eight to nine cells are required to support the +28V DC bus. The estimated weight for two 30 amp-hour batteries is 19 kg.

Power System Electronics

The Power Subsystem is a direct energy transfer (DET) design. Power generated by the solar array is supplied directly to the loads through an unregulated +28V (+/- 7V) bus. The power is controlled by many digitally switched segments and one pulse width modulator segment when excess array power is available.

The Power System Electronics (PSE) takes power from the solar array, provides load power to the observatory, controls battery charging, shunts excess array power, and contains the circuitry required for the protection and command and telemetry interface. The PSE shall be properly designed to interface with the solar array, batteries, and loads. It shall be a single unit that is the primary interface for the Power Subsystem to other subsystems and instruments on the spacecraft. Figure 4.7 illustrates a simplified block diagram of the PSE.

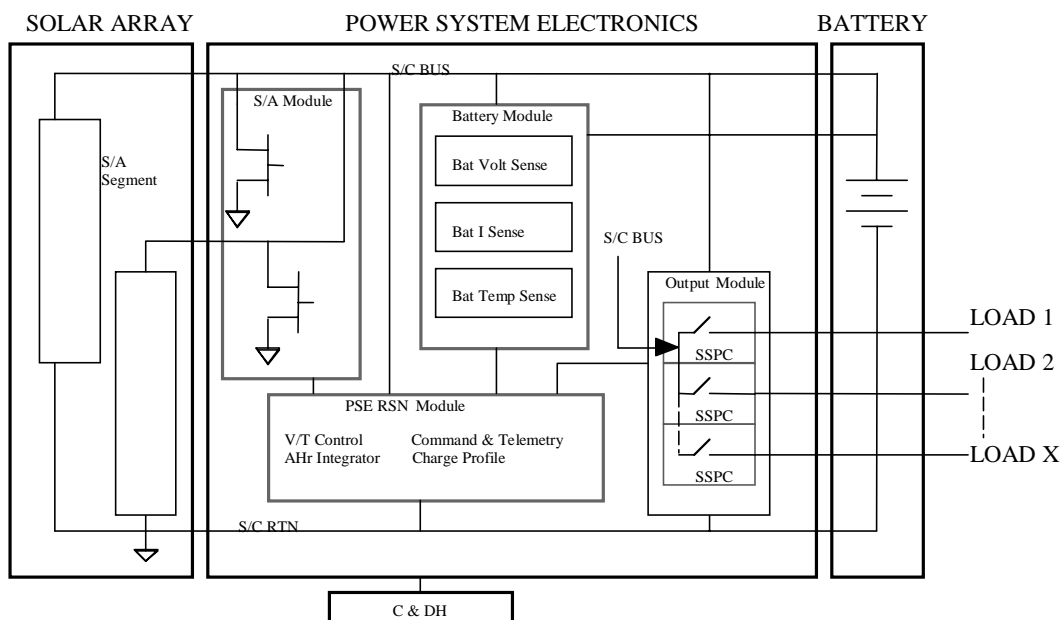


Figure 4.7. NGST Power Subsystem Block Diagram

The solar array module is designed to accommodate the number of solar array segments. These segments are connected to digitally switched, solid state shunts and PWM converter. The shunts, which are surface mount FETs, are switched according to the power needs of the battery and loads. The battery module monitors the battery voltage, current, and temperature. Figure 4.7 illustrates a simplified block diagram of the battery module. The load switching module performs the power switching and distribution to the spacecraft and instruments using SSPC.

The PSE is controlled by software in the PSE RSN Module. It consists of shunt regulator, battery current controller, battery V/T limit controller, battery amp-hour integrator, bus overvoltage regulator, and telemetry and protection circuits. The battery charge control and solar array PWM control signals are generated by the system software running on the radiation-hardened microprocessor. The PSE shall provide all the telemetry and command interface circuitry required to properly interface with the C&DH 1773 optical interface.

The backplane connects the module together, provides termination for the digital signal lines and conditions the power bus with multichip ceramic capacitors.

4.5 Command and data handling

The Command and Data Handling (C&DH) system processes, stores and formats all science instruments and spacecraft data and commands for the observatory. The ACS and Power subsystem have software and processor hardware resident in their respective electronics. The instrument, however, uses a processor housed in the C&DH electronics. A MIL-STD-1773 bus is used to communicate between the C&DH processor, the ACS processor and the Power processor. The interface to the RF

subsystem includes two low rate uplink/downlink interfaces, one for each S-Band transponder unit. In addition two high speed downlink interfaces are provided, one for each X-Band transmitter.

The data from the science instruments is summarized in Table 4.3. If the instruments are assumed to generate data independently and 384 analog to digital converters are used, the peak instrument data transfer rate to the C&DH system will be approximately 1 gigabit per second. The average transfer rate because of the long integration times is approximately 1.6 megabits per second. The data is received from the instrument, and placed in a temporary memory buffer, corrected with the back-ground readings and, formatted into CCSDS packets. The data is then read from the temporary buffer compressed using a 2:1 lossless compression algorithm executing in a dedicated hardware chip, and transferred to the solid state recorder.

Table 4.3. Science instrument data rates

<i>NIR</i>	<i>FPA</i>	<i>256X256 sections</i>	<i>ADC's</i>	<i>Bits/pixel</i>	<i>Readout period (us)</i>
NIR Camera	4	1024	256	16	6
NIR Spec	1	256	64	16	6
TIR Camera and SPEC	1	256	64	16	6

With only one ground station, the spacecraft must operate through a 16-hour period with no ground communications and support a 8-hour continuous ground pass. This requires the inclusion of a large solid state recorder, approximately 92 gigabits, and the capability to perform, record and playback operations at full rate, approximately 1.6 megabits per second, simultaneously. The long period without communications also requires the C&DH processor to accommodate large command loads and software for autonomous spacecraft control.

The X-band downlink interface reads packets from the solid state data recorder and places them in CCSDS transfer frames with optional convolutional encoding or Reed Solomon encoding. The final serial data stream containing both spacecraft telemetry and instrument images and telemetry is connected to redundant X-band transmitters via copper cable for transmission to the ground. The data rate for this serial stream is 1.6 megabits per second before coding. A redundant S-Band telemetry link is driven in a similar fashion. The downlink data rate for the S-Band services is limited to 16 K-bits per second, and will primarily be used for housekeeping data when X-band downlink services are not available.

The uplink services provided will include CCSDS commanding to all subsystems at 2 kbits per second or 16 kbits per second. Command processing will include standard command block verification and COP protocol implementation. In addition hardware commands are available for resets/redundant hardware switch-over. The 2 Kbit S-Band uplink and the 16kbit S-band downlink will primarily be used for engineering passes at ground stations without X-band downlink capability.

Stored telemetry will be placed in the solid state recorder without compression to allow any ground station to decode and display spacecraft housekeeping data. Ground, stored commands, and commands generated by any on board autonomy software is coordinated and distributed by the space-

craft processor command software and distributed on a MIL-STD-1773 bus.

The baseline C&DH system consists of the following circuit assemblies: Instrument Interface, Solid State Recorder, Science Data Processor, Spacecraft Data processor, Uplink/Downlink, Housekeeping RSN. The mass and power for these items is summarized in Table 4.4.

Table 4.4. Power consumption and mass of the C&DH system

<i>C&DH Assembly</i>	<i>Power</i>	<i>Mass (kg)</i>
Instrument I/F	20	1.1
Science/Spacecraft Processor	15	1.1
Solid State Recorder	8	1.1
Uplink/Downlink	7	1.1
LVPC	21	1.1
H/K RSN	5	1.1
Chassis		4.4
Total	76	11

The science instrument's interface contains an optical network interface with a 1giga-bit/second capability, a temporary frame memory buffer, a data compression circuit, and a high speed backplane interface used to communicate with the solid state recorder memory, instrument processor and C&DH processor. The gigabit interface accepts data from the instrument ADC package and places it directly into the temporary frame buffer.

The science data processor has a high speed backplane interface, used to access instrument data in the temporary frame buffer. The NIR mini-camera is implemented through this interface. The science processor is responsible for managing the data compression and handshaking with the spacecraft processor to store compressed images in the solid state recorder. The science processor can communicate directly with the spacecraft processor using the backplane interface.

The solid state recorder provides 92 gigabits of storage for science and spacecraft data. The recorder is implemented using SEU tolerant, semiconductor memory with a high-speed backplane interface. The memory is flat to allow for simple software access and arranged in segments to allow for redundancy. The solid state recorder will incorporate hardware single bit detection and correction, and double bit error detection and any 32 bit boundary. The spacecraft processor will scan the solid state recorder to detect and correct errors.

4.6 Communication system

The communication system is sized to communicate with a dedicated ground station equipped with an 11 meter antenna. The maximum look angle to the center of the Earth is +/- 50 degrees. There are two transponders each using an S-band Omni antenna and an X-band phased array antenna. The block diagram of the system is shown in Figure 4.8.

Uplink commands are received by redundant S-band receivers via the S-band omni antenna, detected and passed on to the C&DH.

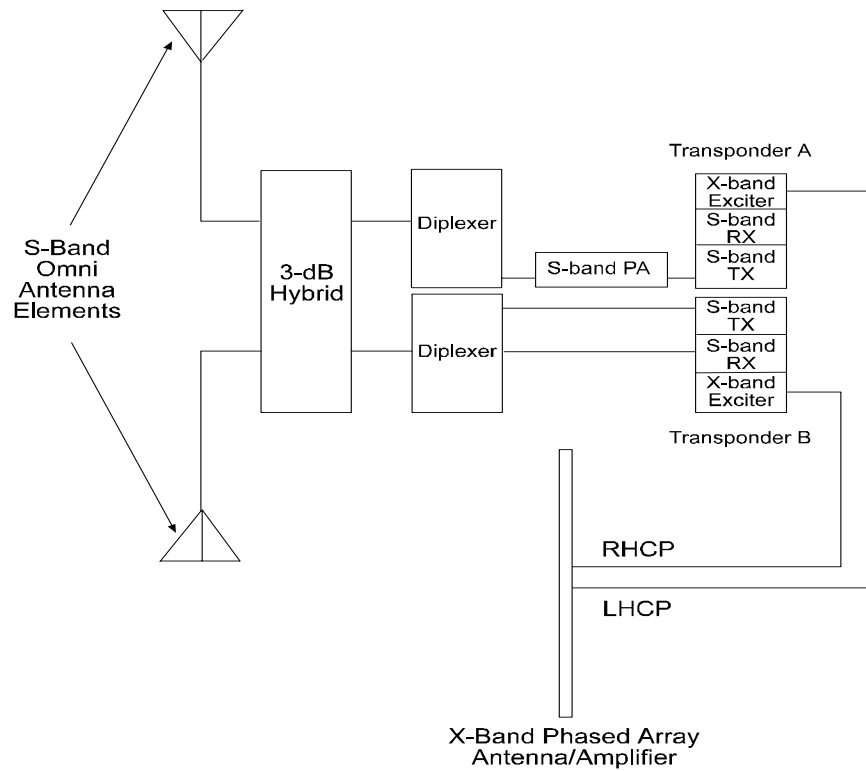


Figure 4.8. Communication system

5. WAVEFRONT CONTROL SYSTEM

Upon deployment the primary mirror segments and the secondary mirror will likely be off their ideal position due to launch stresses. Cooling down the OTA to the operating temperature will produce figure changes and additional position errors. Additionally, during normal operation, attitude changes and aging of the thermal protection may also induce unacceptable mirror displacements. The initial alignment and figure control and the periodic wavefront maintenance during the lifetime of the observatory are performed by the Wavefront Control System (WFCS). This is an active optics system composed of a wavefront sensor, displacement control of each element in the optical train, shaping actuators on the primary mirror segments and a deformable mirror (DM) located at the exit pupil.

Wavefront control proceeds in two phases. The first, coarse alignment and phasing mode, is used only when the optics are very badly misaligned, as they will likely be following launch and deployment. It has a very large capture range (about 5 millimeters) in order to ease the deployment requirement while still aligning the optical train and phasing the primary mirror segments to within about one micron. The second, the fine figure control mode, is invoked next, and uses the primary mirror adjustments and figure shaping and the DM to improve the wavefront to below the diffraction limit at the 2 micron wavelength.

Once the telescope is aligned and phased, the wavefront control system is turned off. Passive structural stability is relied upon to hold figure and alignment during observations. The wavefront quality is checked periodically and the wavefront control system reactivated as required.

5.1 Wavefront Sensing

Wavefront sensing is provided by the near infrared camera with the telescope pointed at a bright star. For coarse alignment, the camera is read at its maximum rate (30 Hz) for line of sight jitter removal. Once the telescope is sufficiently aligned (but not necessarily phased) the guiding system is activated using one of the four NIR cameras while another camera is used for wavefront sensing.

Wavefront errors are determined by obtaining defocused star images and analyzing the image with a “phase retrieval” computer algorithm. Phase retrieval refers to those computer methods which produce an estimate of wavefront errors by analyzing the intensity pattern in defocused images (e.g. phase diversity, curvature sensing, etc.). There are several good alternative approaches for wavefront sensing: Twyman-Green interferometers, Mach-Zender interferometers, shearing interferometers, Shack-Hartman sensors (together with a segment metrology system), all provide interesting options. Phase retrieval was selected as a baseline because it is the simplest, as it does not require additional

sensors, and introduces a minimum of new error sources. It is also intrinsically redundant since the same basic algorithms can be run on images obtained in any of the NIR (or even MIR) channels. Both the imaging and the spectrographic modes of the cameras are used. Imagery is used during focus and coma sweeps runs for measuring errors from the mm-level to several waves. The low resolution spectrographic mode is used for fine corrections.

Defocused images are obtained by moving the Offner relay secondary mirror in the NIR camera. Two images are obtained, one intra and the other extra-focal, producing a roughly 2,000-point estimate of the wavefront. The required processing is performed on the ground, but a program to implement this onboard is currently being developed.

5.2 Optical elements actuators

As described in detail in sections 1.2 and 1.3, the position of each element in the optical train can be adjusted in translation and rotation along all 6 degrees of freedom with an accuracy of about 20 nanometers. In addition, the primary mirror segments have shaping actuators which allow for the correction of the radius of curvature.

5.3 Wavefront control process

Upon deployment, all 8 primary mirror petals are purposefully tilted away by several arcminutes from their nominal position relative to the center segment. This ensures that the image given by each petal does not interfere with the image of the central segment. Then begins a sequence of actions to capture and align each segment with respect to the secondary mirror and the focal plane in the Integrated Science Instrument Module. The central segment is aligned first. Once this is done, the guiding system is turned on to stabilize the line of sight and the outer petals are aligned using the central segment as reference. The primary mirror segments and the rest of the optical train are then fully aligned, focused, and phased by successive iterations of medium duration exposures, phase retrieval, and uplink of the desired optical elements displacement commands. Once this petal cophasing is finished all petals are returned to their predetermined position. Cophasing of the entire set may not be perfect because of actuator repeatability errors, so a final phase retrieval iteration is executed to correct these residual errors.

The final step consists in setting the DM to minimize residual wavefront error due to segment to segment edge discontinuities and figure errors in each segments. By design, the wavefront error following alignment, phasing and first order figure shaping of the primary mirror segments is expected to be 150nm rms (i.e. $\lambda/13$ at $2\mu\text{m}$, which corresponds to a Strehl ratio of 0.8). The DM can improve the wavefront by about a factor of 10. The main reason for the DM correction is to provide a margin of safety. But if the expected goals for the main optics are met, use of the DM will allow diffraction limited imagery down to the visible.

After the initial image capture, optics alignment and cophasing, the optical train is expected to passively hold its figure even following attitude changes (Section 6, Thermal, and Section 10, Observatory Performance). However, structural dimensional changes over time, and large changes in

thermal environment may require periodic tuning up. The image quality will be monitored using science observations and dedicated tests, and the image capture, alignment and cophasing process described above will be repeated as required.

A simulated example of the wavefront control process is shown in Figure 5.1. The process is described below.

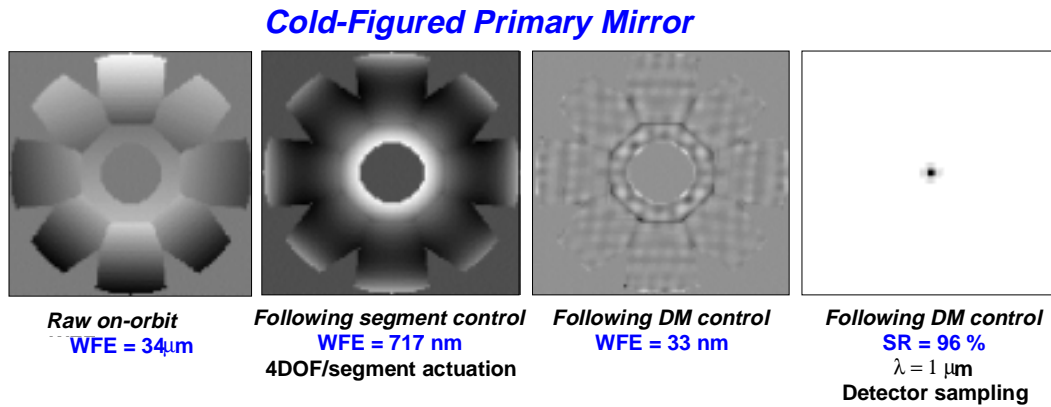


Figure 5.1. Simulated wavefront error at the main stages of the wavefront control procedure. The initial wavefront error upon deployment is shown at left. The second panel shows the improvement following alignment and phasing of the segments. The third panel shows the improvement obtained with the DM. The resulting image, with a Strehl ratio of 0.96 is shown at right.

Initial capture and alignment

The telescope is pointed to a field containing a very bright star and stabilized to within 2 arcseconds rms using the attitude control system star trackers. The image of the star given by the center segment is then located in one of the 4 NIR cameras (4' x 4' total field). If no image is found, the central segment is tilted in a growing conical pattern until its light crosses the focal plane, though perhaps in a large chaotic blur. Once this blur is identified, the center is determined and then driven to the center of one of the NIR cameras. The central segment is then displaced in piston through a range of about 2 mm to measure the spot diameter in order to determine the degree and sign of the defocus. Once this is done, the segment is driven to its best focus position. Large misalignments inducing coma and other aberrations are likely to be present the first time this is done. However, the image is good enough for the guiding system to work, and the fast steering mirror is activated to stabilize the image to a fraction of an arcsecond.

Next, the *coarse alignment* of the secondary mirror to the center segment and the focal plane of the instrument module is commenced. This process utilizes “prescription retrieval” software called VSIM, which processes out of focus narrow or broadband imagery to directly estimate misalignment and low-order figure error terms. VSIM has been successfully applied to several different instruments, starting with the Hubble Space Telescope and including several other space instruments, tested in situ or on the ground. With appropriately diverse data VSIM is capable of separating the effects of misalignments from those of figure errors, and can distinguish between figure errors on multiple surfaces. Experience indicates that VSIM will enable alignment of the center segment to the SM and ISIM to within a few mm and milliradians.

Coarse phasing

The next alignment operation is the coarse phasing process. Each outer segment is tilted back in, one at a time, and coaligned with the center segment, so that their 2 spots overlies. The 2 segments are not in phase at this point, with perhaps a few microns difference between them. To detect this phase difference, a grism is placed in the beam, creating a “dispersed-fringe sensor” (DFS) as illustrated on Figure 5.2. The DFS disperses the light from the 2 coaligned segments up and down the detector, so that the light at any point on the detector is at a single wavelength. Phase differences between the 2 segments cause the overlapping images to produce interference fringes. The period of these fringes is a function of the absolute phase difference between the 2 segments.

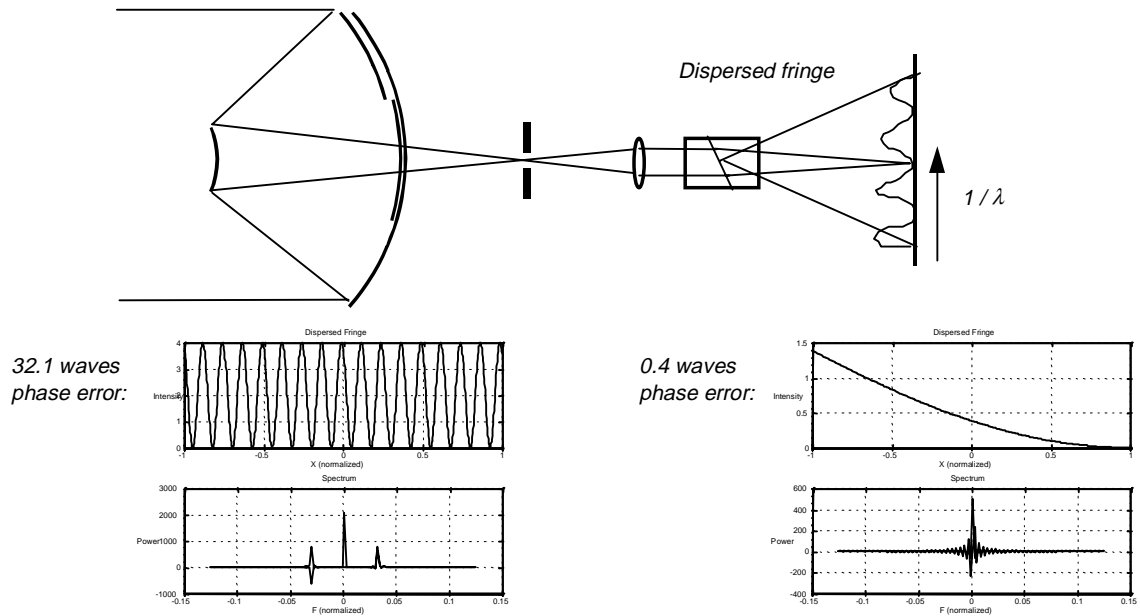


Figure 5.2. Cophasing of two mirror segments using a Grism in the near-IR camera to spectrally spread the images a bright broadband calibration star produced by 2 segments. Phase differences between the 2 segments cause the overlapping images to produce interference fringes. The period of these fringes is proportional to the absolute phase difference between the 2 segments. Use of this spread fringe phase sensor allows pairwise phasing to within $1/4$ in just a few actuation steps. (This phasing approach is in routine use at the Palomar Interferometer, where it is used to phase up widely-separated small apertures using starlight.)

The DFS has a large dynamic range. The maximum detectable OPD difference is defined by the Nyquist sampling limit of the particular detector and the dispersion of the grism. This will nominally be set to be larger than the focal depth of the segments, as greater OPDs can be easily detected and corrected by simple focus scan techniques. Aberrations, including defocus, will tend to reduce the visibility of the interference fringes, but with many of them spread out across the detector this is not expected to be a significant problem. Alignment of the grism to the detector may be done following the alignment of the central segment, using narrow-band filters to register particular wavelengths on the detector. Use of the DFS allows pairwise phasing to within a wave in just a few actuation steps.

The coarse phasing of segment pairs concludes with a “direct image-sharpening,” or “white-light interferometry” (WLI). Following the setting of the outer segment using the DFS, the DFS is removed from the beam by rotating the filter wheel, so that the detector once again sees a star image. The outer

segment is then scanned in piston, and the position with the highest peak intensity is identified. The segment is moved back to that point.

Because the DFS is used, the starting point for the image sharpening step will be rather good, and a single step of image sharpening should yield excellent segment-to-segment phasing accuracy, within WF precision set by the segment figure quality. If the DFS would not be used, the starting point may not be as good. If the initial error is many waves, piston will have to be scanned over a long range. The coherence of the 2 spots depends on the bandpass of the filter and source that produces the image. The peak intensity oscillates at the half-wavelength scale, within an envelope defined by the bandpass of the source/filter used. The sharpest peak represents the white-light fringe, and occurs at the ideal inphase point.

At this point, coarse phasing of the first outer segment to the central segment is complete. The coarse phasing process is then repeated for the next segment. This can be done pairwise, with respect to the central segment, by tilting the previously-aligned segment back out of the way, or it can be done relative to the multi-segment aperture composed of the central segment and all previously-aligned segments.

When all segments have undergone coarse phasing, and all are brought back into alignment with the central segment, the OTA optical train will be aligned and phased to within a wave.

The computer processing required for most phases of the coarse figure control is within the capabilities of the onboard computer. The exception is the prescription retrieval phase, which requires workstation-class processing if completion is desired in a few minutes.

5.4 Fine figure control

Fine Initialization Control continues where the Coarse phasing leaves off: with the PM segments, SM and ISIM phased to within about a wave. The fine figure control phase makes fine adjustment of the position and figure actuators of the segments and finally sets the 349 actuators of the continuous face-sheet DM to minimize WF error. The result is a diffraction limited telescope at 2 μm wavelength.

As with the coarse figure controller, all sensing is performed using the Near IR Camera. Focus-diverse imagery is required, and is obtained by defocusing the Near-IR camera. The required processing is substantial but may be performed onboard. If not, then ground-based processing is an option, with the resulting segment and DM control commands uplinked for implementation on the spacecraft.

Wavefront sensing is performed using focus-diverse, iterative transform phase retrieval. This starts by taking two or more images, defocused enough to spread the light over a large number of pixels (20-200, depending on required sensitivity and desired spatial frequency resolution). Typically 3 images, one in focus and 2 taken on opposite sides of focus, are used. These images are processed using a

modified Gerchberg-Saxton algorithm. The G-S iteration starts with a random guess at the phase of the pupil used to form the image. This is combined with the square-root of the amplitude of the image data to create an estimate of the image. This is inverse Fourier transformed back to pupil space, and then the phase due to the diversity factor (the defocus) is removed, and the aperture mask is applied. The result is an estimate of the in-focus pupil. Then the diversity factor is put back in and the result is Fourier transformed back to the image plane. The phase from this estimated image-plane field is combined with the square-root of the data to start the next iteration.

About 10 of the G-S iterations are performed for the first image before moving to the next and repeating. The pupils estimated by iterating on each image are weighted and then combined to generate a joint estimate of the in-focus pupil wavefront. The entire process is repeated, typically 20-40 times, until the difference between iterations is below some low threshold.

6. THERMAL SYSTEM

A telescope the size of NGST Near Earth would require an impractical large amount of cooling power to be cooled actively to the cryogenic temperatures required for NIR and MIR operation. The solution is passive cooling and consists in:

- protecting the observatory from the Sun with a multilayer shield,
- using a high Earth or deep space orbit so that the Earth's thermal input is minimal, and
- in configuring the telescope to have a large view of space to improve radiative cooling.

The L2 orbit is actually ideal in this case because the sunshield can also hide the Earth and the Moon.

Baffles and stops prevent the science instrument detectors from directly seeing any surface other than the mirrors in the optical train. However, the non-optical surfaces and, in particular, the large sunshield's back surface, can still irradiate the detector by scattering off the mirrors. Indeed, the sunshield's back surface is the single most important factor on which the observatory thermal emission affecting the focal plane depends (see Figure 6.1).

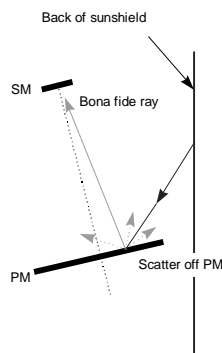


Figure 6.1. Scatter from the back of the sunshield is the dominant source of self-emission in the observatory.

The back surface of the sunshield controls the minimum temperature of all elements in the telescope and its own radiation reaches the detector by scattering. For the thermal self-emission to be negligible compared to the zodiacal light, the back of the sunshield must at a temperature below 100K (Figure 6.2). This can be accomplished by adding 5 low emittance layers behind the surface of the shield facing the sun. Under these conditions, the main optics are at very low temperatures (about 30K for the primary and 26K for the secondary mirror) and do not contribute significantly to the overall self-emission of the observatory.

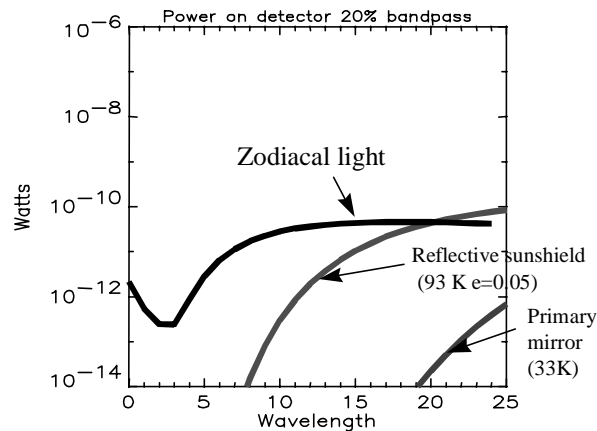


Figure 6.2. The back of the sunshield must be under 100K and reflective to reduce the self-emission of the observatory below the zodiacal light level up to 20 microns.

An advantage of reducing the OTA temperature to about 30K is that the NIR detectors do not need extra cooling. The MIR detector will require cooling to about 8K which can be obtained with a cryocooler or a cryostat.

6.1 Thermal design overview

Sunshield

The sunshield consists of six parallel layers separated to inhibit heat conduction. Each layer is made of $\frac{1}{2}$ to 1 mil Kapton to minimize shield mass and volume during stowage and launch. Each inner layer is aluminized on both sides to inhibit radiation from layer to layer and to assist with reflecting heat energy from the gap between the layers. If effective emittance, ϵ^* , is used to quantify the sunshield's thermal performance, then the sunshield needs to have an ϵ^* no greater than 0.0003. Since typical multi-layer insulation (MLI) cannot meet this stringent low ϵ^* , the shield layers are configured to allow thermal energy to escape to space from between the layers before reaching the cold side layer. This approach allows a low effective emittance and enables passive cooling with a relatively small number of layers.

ISIM

The thermal control concept for the ISIM has been described in Section 3.8. A parasitic radiator serves to intercept heat from the sunshield, SSM and OTA. The side of the ISIM facing away from the sunshield serves as the main radiator for the NIR detectors.

Spacecraft Bus

The OTA and ISIM are conductively isolated from the spacecraft bus via a deployable isolation truss made up of low conductivity material such as gamma-alumina. The spacecraft bus is located on the sun side or warm side of the sunshield allowing it to operate at typical spacecraft temperatures.

Typical spacecraft thermal control techniques are utilized. The spacecraft is unique in that it does not have any dedicated views to deep space. A majority of spacecraft power dissipation will be radiated from sun facing radiators. Optical solar reflectors will be used on the radiators to provide a robust and durable low a/e thermal coating. The solar array will utilize a low packing factor to moderate its temperature to ensure reliability for a 5- to 10-year mission life.

6.2 Thermal environment

Orbit

The L2 orbit point provides only solar environmental heating since heat energy from the earth is negligible. L2 allows NGST to be oriented such that both the earth, moon, and sun are always on the hot or sun side of the sunshield.

Attitude Pointing

Thermal analyses consider the extreme off pointing of up to 27 degrees. The sun shield layers are configured to prevent solar energy from impinging on the OTA or between the layers during maximum off normal pointing. As illustrated in Figure 4.6 pointing access to 40% of the sky is achieved by pitching the observatory up to ± 25 degrees off the sun line and allowing 360 degrees of roll about the sunline.

Transfer Deployment/Orbit

All OTA deployments will be completed before the sunshield is deployed to allow relatively warm temperatures on the deployment mechanisms. Various attitude and roll type maneuvers will need to be performed to prevent overheating of critical OTA and instrument components.

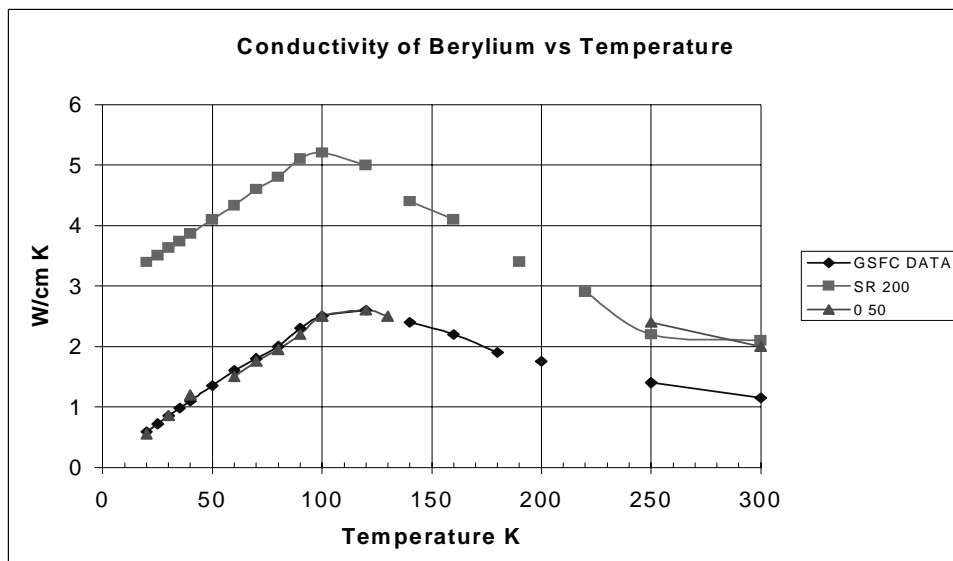
6.3 Thermal modeling

Accurate assessment of sunshield performance relies very strongly on accurate calculation of geometric form factors and gray-body radiation interchange factors. The low emittance and potentially specular nature of the inner layer surfaces complicates these calculations. The Thermal Synthesis System (TSS), developed by Lockheed Martin for NASA's Johnson Space Center, was used to calculate the radiation interchange factors because of its robust Monte Carlo ray tracing routines, and its ability to handle specular as well as diffuse surfaces. SINDA85 was used exclusively to solve for model nodal temperatures. FEMAP and TCON were also used to modify and refine structural finite element models to be more useful for thermal calculations.

Table 6.1 lists the various thermal conductivities and capacitances used in the thermal modeling. For conservatism, i.e. larger gradients, a single value for the conductivity of titanium at 35K is used in OTA analyses. The temperature variation of conductivity of beryllium and gamma alumina are shown in Figure 6.3, and Table 6.2 lists the various thermal-optical properties for the sunshield and the telescope structure.

Table 6.1 Material Thermal Conductivity

Material	Conductivity	Thermal Capacitance
Beryllium @35K	100.00 W/mK	34.1 J/kg-K (@60K)
Titanium (max. at ~40K)	4.22 W/mK	
Graphite epoxy	1.0 W/mK	
gamma-alumina	1.0 W/mK	
Copper, OFHC @35K	1100 W/mK	

**Figure 6.3.** Conductivity of Beryllium**Table 6.2.** Analysis Diffuse Thermal-Optical Properties

Coating	α	$\epsilon_{\text{hemispherical total}}$	BOL/EOL
Kapton/ITO 0.5 mil aluminized	0.34	0.55	BOL
Kapton/ITO 0.5. mil aluminized	0.59	0.55	EOL (10 year)
black surfaces on cold side	NA	0.70	NA
Beryllium	NA	0.03	NA

6.4 Results

Baseline steady state analysis results at end of life (EOL) are listed in Table 6.3. Each major component is listed with its temperature. Minimum and maximum are also listed if a particular component exhibits large temperature gradients such as the primary mirror. Figure 6.4 depicts a system-level heat map for the EOL case.

Table 6.3. Baseline Steady State Results, Temperature in K

<i>Assembly</i>	<i>EOL</i>		
	<i>Avg</i>	<i>Min</i>	<i>Max</i>
SSM	293	293	293
Shade Layer 1, sunward	395	395	395
Layer 2	336	300	359
Layer 3	263	214	295
Layer 4	190	141	230
Layer 5	157	113	193
Layer 6	121	86	151
Primary Mirror	46	36	55
Secondary Mirror	22	22	22

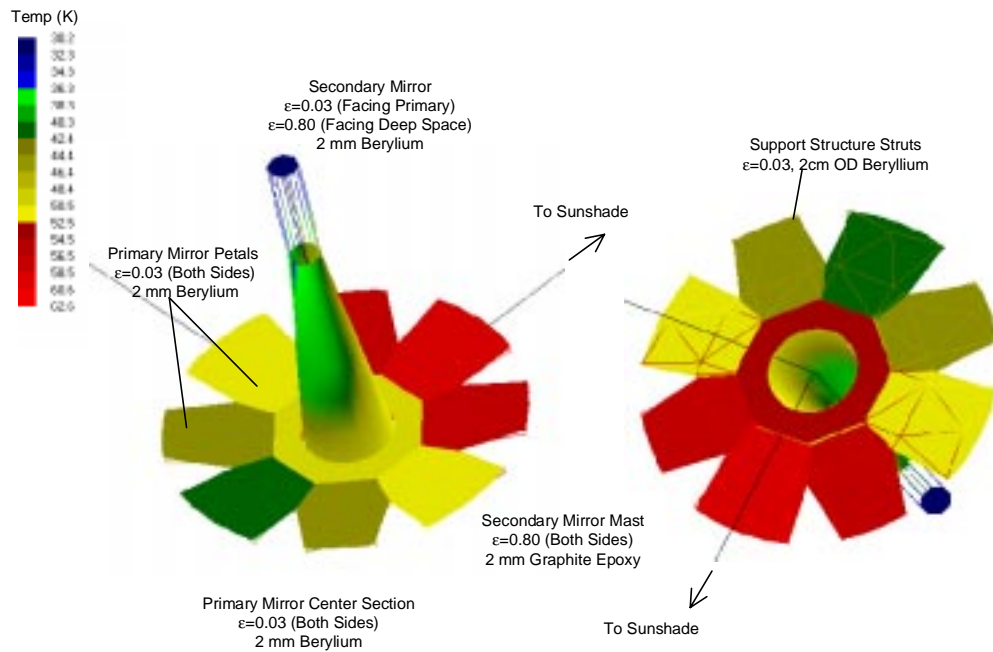


Figure 6.4. Temperature field of the OTA (front and back)

A summary of heat flow is shown in Figure 6.5. Transient analyses using the detailed OTA model are conducted assuming the NGST is slewed the maximum of 27 degrees off normal. Temperature results from this slew are then put into the end-to-end model to determine the slew's thermal effect on optical wave front error. (See Section 10).

Initial studies indicate sunshield area losses due to micrometeorite damage on all six layers could be as high as 0.7%. This damage was modeled by adding transmittance to the shield layers of 1 and 2 percent and the results are shown in Figure 6.7.

A variety of parametric analyses has been conducted using the yardstick models to examine various sensitivity and configuration issues. Examples include examining the effects of micrometeorite damage and emittance degradation on the sunshield's thermal performance.

The sunshield thermal design needs to be robust enough to tolerate degradation of the low emittance of the inner surfaces potentially due to contamination, coating imperfections, micrometeorite impact residue, or measurement error. Figure 6.8 shows the relationship between primary mirror temperature and inner surface emittance.

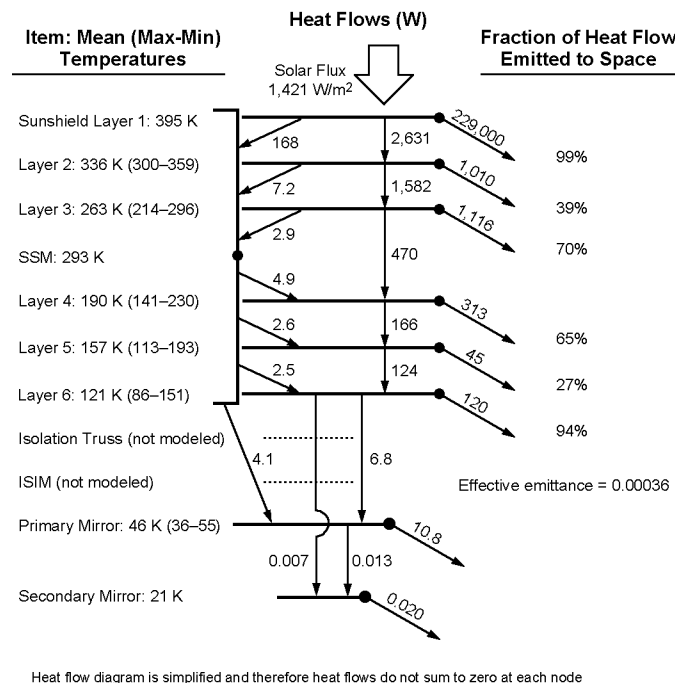


Figure 6.5. Heat flow through the observatory

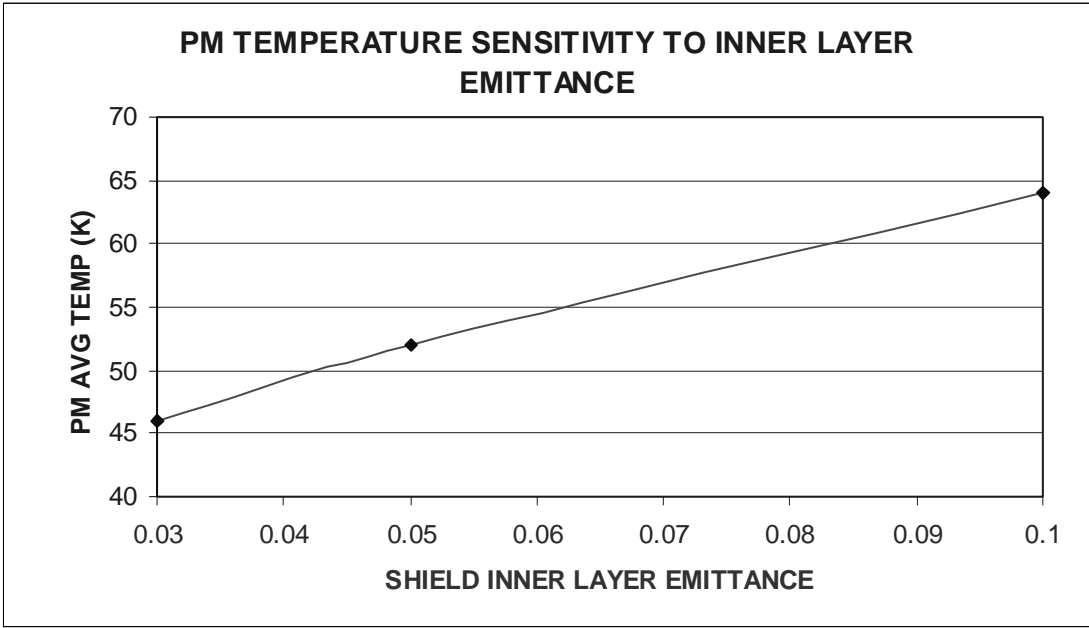


Figure 6.6. Effect of inner layers (those layers between the sunside and OTA side layers) emittance on primary mirror temperature

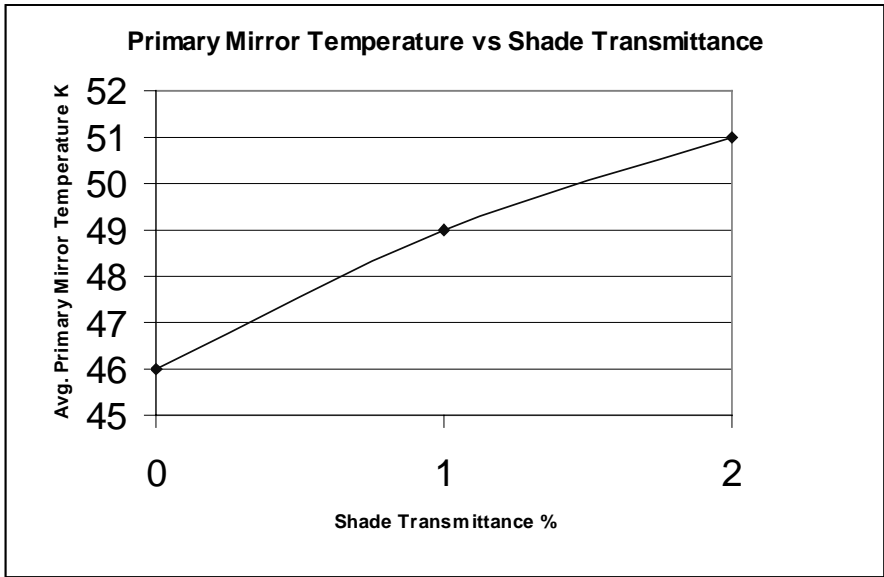


Figure 6.7 . Effect of inner layer emittance on primary mirror temperature

7. POINTING CONTROL SYSTEM

7.1 Rationale

A characteristic feature of our NGST yardstick concept is its offset geometry: the spacecraft support system (SSM) is not close to the payload as is generally the case, but away from it at the end of the isolation truss. This is because most of the SSM functions, including the attitude control system, need to operate at warm temperatures, which is not compatible with a passively cooled OTA. The attitude sensors could operate cold, but locating them on the OTA, away from the reaction wheels, would create instabilities due to the flexibility of the isolation truss connecting the SSM to the OTA. In such a situation, “body pointing”, that is to say the direct pointing of the OTA to the required milli-arcsecond level, is very difficult. In the case of HST, the telescope is pointed directly by the spacecraft attitude control, but this requires a very stiff spacecraft and telescope structure, which cannot be afforded for NGST. It also requires very precise gyroscopes, star trackers and/or fine guidance sensors, precise, low-noise reaction wheels, and a relatively high bandwidth attitude control system, all of which are costly.

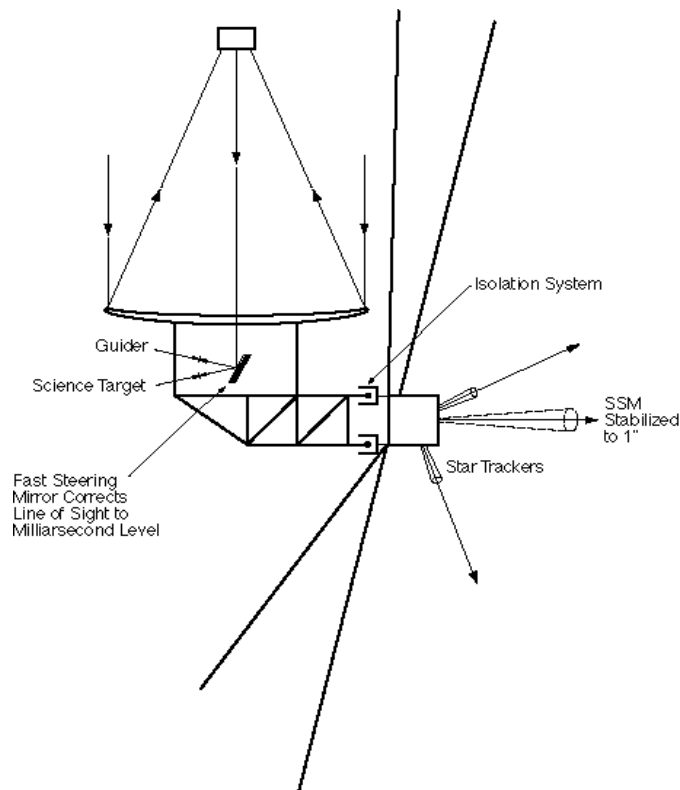


Figure 7.1. Schematics of the attitude control system and line of sight control systems

The solution adopted for the Yardstick architecture is to use an image compensation system composed of a guiding sensor monitoring a star in the field of view of the telescope, coupled to a fast steering mirror stabilizing the line of sight. With such a system, the requirements on the attitude control system can be much relaxed (to about 1" rms), and can use standard components. With an image compensation system, the attitude control system does not need to have any authority over the flexible modes and can have a very low bandwidth to avoid instabilities which could be created by the highly flexible structure of the observatory.

In what follows we first described the various components of the pointing control system, make a first order estimate of the pointing quality, and then present the results of a detailed simulation of the overall performance of the system.

7.2 Spacecraft attitude control system

The spacecraft attitude control system (ACS) is of a fairly conventional design featuring a 3-axis stabilized inertial Attitude Control System. The ACS also has the responsibility for controlling the spacecraft maneuvers, momentum management, and providing a safe, sun-pointing attitude during the initial deployment phase of the mission as well as during anomalous events.

The ACS is located in the SSM and consists of a processor for digital control and a typical complement of actuators and sensors: star trackers, gyros, coarse and fine sun sensors, and reaction wheels. The sun sensors are only used for the initial acquisition and safe-pointing modes. Momentum management is accomplished using thrusters, which are properly part of the Propulsion subsystem. During normal science operations, the ACS controller provides stable pointing and maneuvering of the spacecraft bus with star trackers, gyros, and reaction wheels.

The fine pointing mode of the ACS includes sensor processing, attitude determination, attitude control, and actuator processing, as illustrated in the block diagram shown in Figure 7.2.

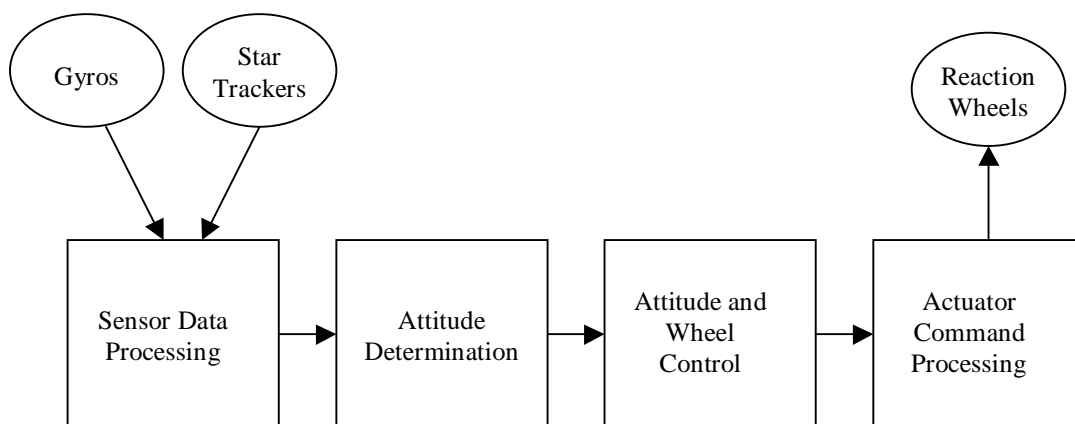


Figure 7.2. ACS pointing control architecture

The processed gyro and star tracker data are used for attitude determination. Inertial attitude is maintained as a quaternion and propagated in time by the rates measured by the gyros, which are sampled at a 10 Hz rate. The star trackers provide direct inertial attitude measurements. There are 2 trackers, aligned in the body frame with boresights 60° to the X axis (the +X axis is the boresight) and with 45° projections to the Y and Z axes. The trackers each have a field of view of $5.3^\circ \times 5.3^\circ$, are capable of tracking as many as 5 stars simultaneously, and have a noise equivalent angle (NEA) of 1.35 arcsec/star/sample, 1σ . The star positions are sampled from the trackers at a 2 Hz rate.

These measurements are optimally combined with the gyro-propagated attitude via a Kalman Filter. This filter assumes that the attitude (star tracker) and rate (gyro) measurements are corrupted by white noise, and furthermore that the rate measurements are corrupted by a random walk component (rate bias, or gyro drift). The inputs to the filter are the residuals, or differences, between the measured and expected positions of guide stars in the star tracker field-of-view. The expected positions are calculated from an onboard catalog of stars with visual magnitude < 7 with positions accurate to 0.03 arcseconds. The outputs of the filter are estimated errors in the inertial attitude estimate (roll, pitch and yaw angle updates) and in the rate bias estimate (roll, pitch and yaw gyro drift updates).

The predicted performance of this attitude determination system can be found by iterating the Kalman Filter equations to steady-state or by numeric simulation. For the sensor sampling rates and noise characteristics provided, the steady-state standard deviations are 0.3, 0.4, and 0.4 arcseconds in roll, pitch, and yaw respectively. In practice, for a well-tuned filter, i.e. one in which the sensor noise statistics are well known and fit the model, typically no more than a few minutes worth of tracker updates are required for convergence to steady-state values.

The reaction wheels provide the torque to steer the observatory. There are 4 wheels, arranged in a 4-sided pyramid geometry. All wheels are actively controlled to provide the 3-axis control. Accordingly, this allows an extra degree-of-freedom in the controller. It is used to bias the mean wheel speed to a desired set point. This feature may be exploited to avoid structural resonances or to maximize bearing lifetime. The 3-axis torque commands are developed via a digital controller consisting of three decoupled, proportional-integral-derivative (PID) controllers in series with lowpass filters for flexible mode attenuation. Cross-axis coupling is provided by a transformation involving the estimate of the spacecraft inertia matrix. The control inputs are the roll, pitch, and yaw attitude errors and rates from the attitude determination block. The PID gains and lowpass filter corners and orders are set such that the rigid body margins are at least 12 dB gain and 30 degrees phase with 10 dB of flexible mode gain suppression. For the highly flexible structure of the NGST yardstick, this requires a 0.025 Hz control bandwidth and filter corners at or below 0.5 Hz. The lowest frequency modes in the structure, those due to the large sunshield, are roughly 0.3 Hz, so it is seen that the ACS has no control authority over the flexible modes.

7.3 Line of Sight Stabilization

Line of sight stability to the required milli-arcsecond level is obtained by steering the optical beam of the telescope. The yardstick ISIM design calls for using a portion of the field of the NIR camera to track an opportunistic guide star. The error signal provided by this sensor is fed into the guiding system, which calculates the amount of correction and feeds it to a fast steering mirror servo loop (Figure 7.3).

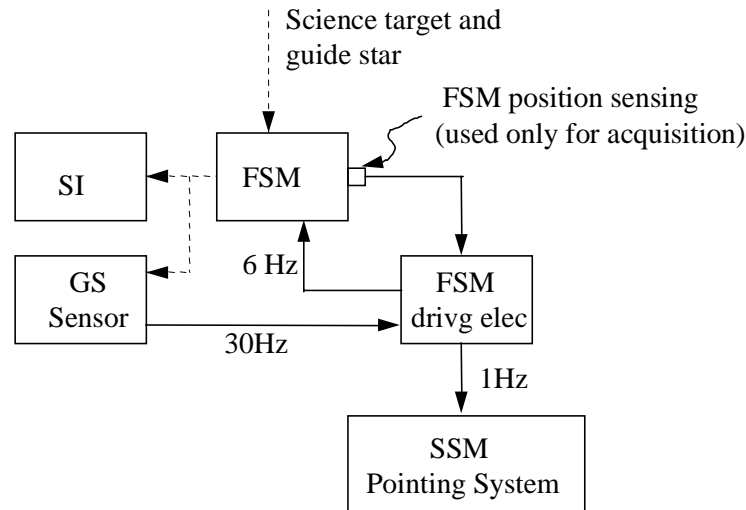


Figure 7.3. Schematic block diagram of the guiding system

Guiding sensor

To eliminate the cost of a dedicated guiding system and avoid constraining the optical system to produce a good quality field larger than the strict science field, the NIR camera is used as a guiding sensor. This is a practical solution because of the large field of the cameras, and because field splitting and extensive detector mosaicing allow the use of a small portion of the field for guiding with little penalty to the science. In normal operation, guide star selection will be done on board autonomously, that is to say without prior uplink of a given guide star location. A short exposure of the desired field will first be made and the resulting image scanned to determine the brightest star which will then be used for guiding. The region of the chip where that star falls will be read at a fast rate to supply the guiding error signal, and the rest of the chip will not be read. All other chips will be used for normal science data.

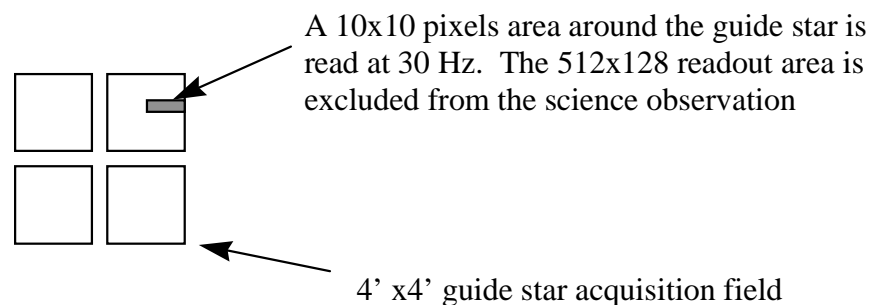


Figure 7.4. Guide star readout scheme

Table 7.1 gives the number of stars of a given magnitude or brighter at the galactic poles per square degree (Soneira and Bahcall model) for the I band and the K band. To ensure 95% probability of finding at least one guide star of a given magnitude or brighter, the average number of stars in the field available for guiding must be 3.0. This indicates that with a field of 4 x 4 arcminutes, the guiding sensor must be able to guide on stars of about 16.5 magnitude in the I band or magnitude 15.5 in the K band.

Table 7.1. Number of stars of a given magnitude and brighter at the galactic pole

<i>Magnitude</i>	<i>I Band</i>	<i>K Band</i>
15	1.4	2.0
16	2.3	3.7
17	4.2	6.7
18	7.7	12.0

To command the FSM servo, the centroid of this guide star must be estimated. This estimate is corrupted by noise, essentially due to photon noise at the detector and characterized as a noise equivalent angle (NEA). If we assume a generic 4-quadrant detector, with 30 electrons of read noise, a detector quantum efficiency of 0.8, an 8 meter aperture, 2.2 microns wavelength with $\pm 25\%$ bandpass, optical throughput of 0.6, and a guide star of K magnitude 16.5, the curve in Figure 7.5 can be plotted to show NEA as a function of integration time. Clearly the noise is inversely proportional to the integration time – the longer photons are collected the greater the signal-to-noise ratio. From the figure we see that above 30-40 ms there is little benefit to increased integration time. Below 30 ms, the noise rapidly increases. Therefore, a 30 Hz sampling rate (33 msec integration time) was chosen for this design.

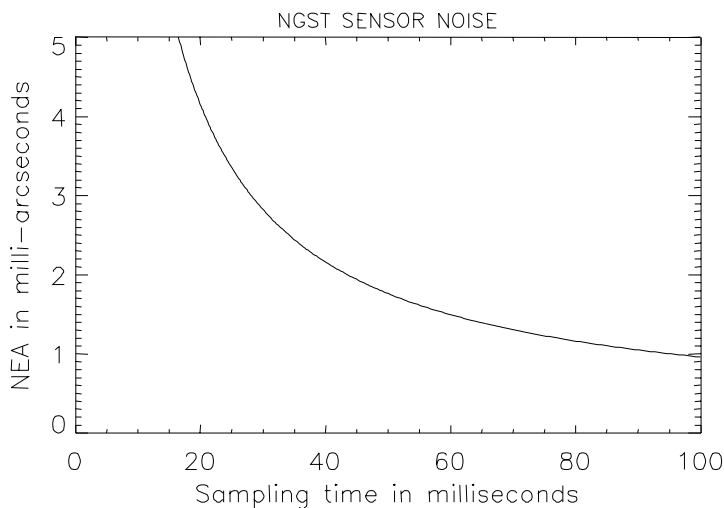


Figure 7.5. Noise equivalent angle of a guiding sensor centroiding on a magnitude 16.5 star in the K band (2 microns)

Fast steering mirror (FSM)

The FSM is located in the Integrated Science Instrument Module. The device is a tip-tilt active mirror with an angular resolution better than 0.06 arcsecond absolute motion (1 mas on the sky). It is suspended on flexures and driven by electro-magnetic actuators. The position sensors are noncontacting differential inductive proximity devices. This configuration has been chosen because of its extremely high linearity, which has been proven to achieve tracking accuracies as low as 10 nrad rms.

Because the FSM is in the incoming beam common to all science instruments, the FSM creates a single-point failure critical to the mission. Therefore, the FSM has fully redundant electronics including position sensors and actuator coils. Additionally, a second, fully redundant FSM is located on the back of the first FSM on a rotating exchange mechanism and can be flipped into place should the first one fail.

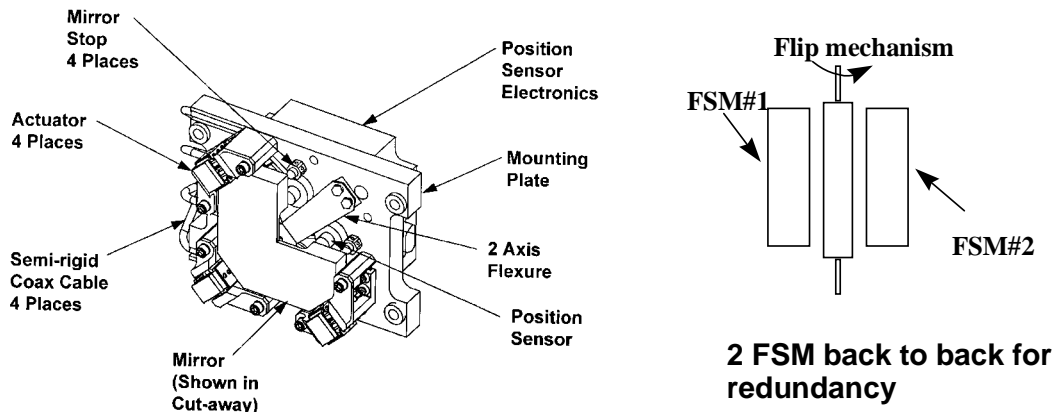


Figure 7.6. View of the fast steering mirror (left); for redundancy 2 FSM are mounted back-to-back on a flip mechanism (right)

The FSM servo loop removes the low-frequency components of the tip and tilt errors from the wavefront. At low frequencies, it provides 60 dB of attenuation to the LOS error, which means the arcsecond level spacecraft motion is reduced to the milli-arcsecond level. In the event of sensor drift or other bias errors, the mirror can be kept centered in its range of travel by a low-bandwidth loop closed around the ACS. This feedback signal would make minor adjustments to the inertial attitude reference.

A model for a cascaded controller and plant transfer functions was derived from transfer function test data for a model FO50-35 FSM manufactured by Left Hand Design Corporation. The poles and zeros were scaled to match the reduction in closed-loop bandwidth from 2200 Hz, the nominal setting for this device, to 6Hz, a bandwidth appropriate for the NGST guide star sampling rate of 30 Hz. The performance of this servo loop is most usefully characterized by the two transfer functions plotted in Figure 7.7. The transfer functions relate the LOS error to each of two inputs: position command (or

sensor noise) and base motion. The FSM loop acts as a lowpass filter to the position command, which attenuates the effect of the sensor noise. Conversely, the loop acts as a highpass filter to base motion, which means that only the jitter due to the lowest frequency modes in the structure (below 1-2 Hz) is significantly attenuated. This requires that any excitation of structural modes critical to the image stability be limited by proper isolation of the disturbance sources.

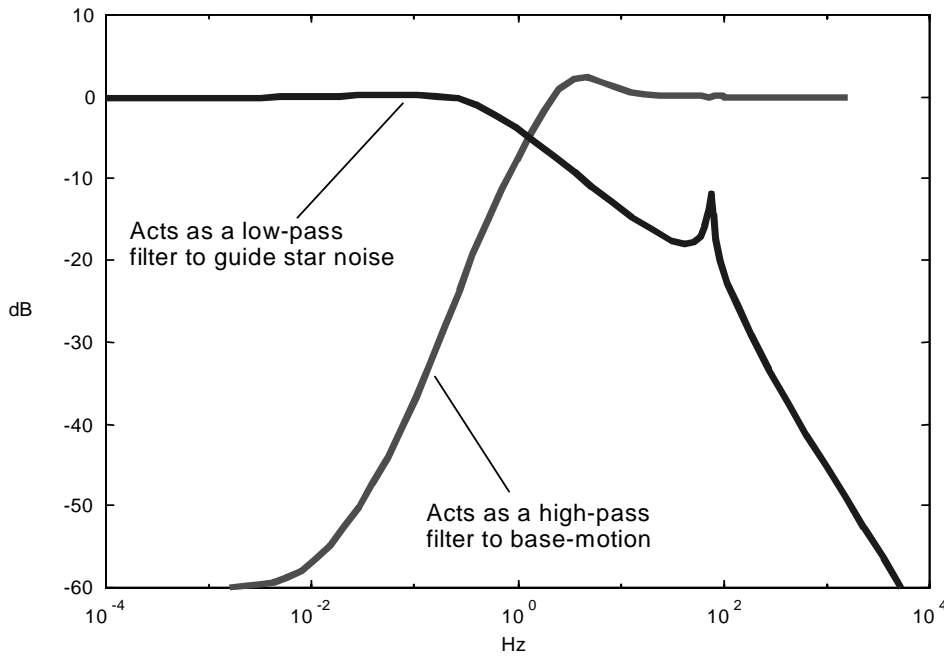


Figure 7.7. FSM servo loop response functions

7.4 Predicted performance

Line of sight jitter results from the sensor noise and from any structural vibration affecting the optical train which is beyond the control range of the FSM. The sensor noise is limited by the availability of bright guide stars to several milli-arcseconds. Neither the FSM nor the ACS has the bandwidth to attenuate the effects of vibration resulting from sources such as reaction wheels, thrusters, or any other mechanisms.

During science operations, only the reaction wheels will operate. The wheels produce disturbance forces and torques due to rotor imbalance and bearing runout. These disturbances are not broadband like sensor noise, but tonal in nature, appearing at frequencies corresponding to the wheel speed and at harmonics thereof. The wheel speeds will vary during observations, according to conservation of momentum, to accommodate the external torque from solar pressure on the thermal sunshield. In between momentum unloads, the wheels will cover a speed range from ~200 rpm out to ~4500 rpm. When accounting for higher order harmonics, 5-10 times the fundamental, the disturbance spectra

will extend out to many hundreds of Hz, well above the bandwidth of the ACS and FSM control loops.

These disturbances will interact with the primary bending modes of critical structural elements such as the sunshield, secondary mirror supports, and thermal isolation truss at frequencies below 10 Hz. They will furthermore interact with higher order bending modes of these elements, as well as modes of the SSM, OTA and ISIM, at frequencies above 10 Hz. Adding passive isolation to the reaction wheel mounts is a proven means of providing attenuation (~40 dB/decade) to these forces and torques. Not all modes significantly contribute to jitter. The isolator must be tuned to provide adequate attenuation at the first significant mode in the system.

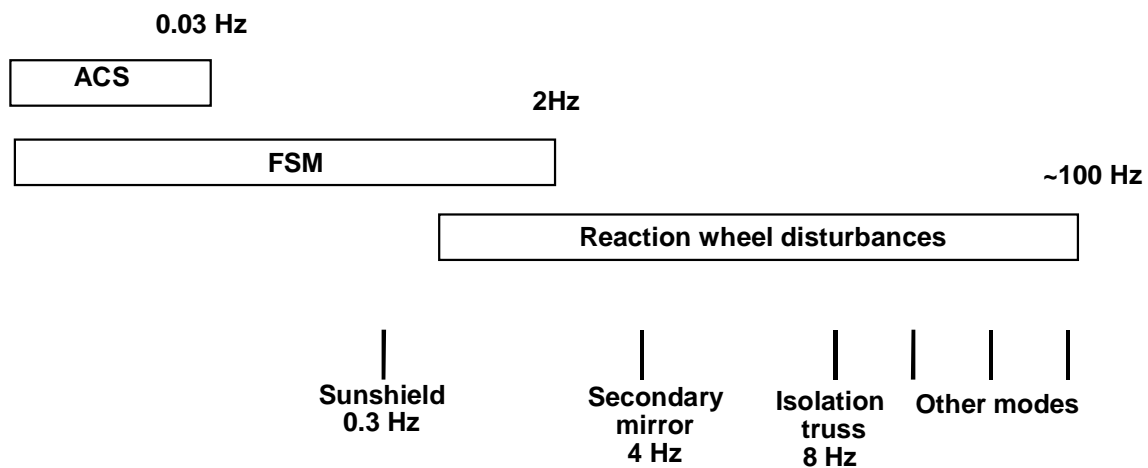


Figure 7.8. Relative distribution of the disturbance frequencies and bandwidths of the attitude control and image compensation systems. The bandwidths of the image compensation system is limited to about 2 Hz. Disturbances beyond this frequency must be either negligible or attenuated by isolation.

First order estimate

A first order estimate of the pointing performance can be obtained as follows. We assume, as previously stated, that the only source of dynamic disturbance is the reaction wheels. The wheel imbalance and bearing runouts induce forces (and torques) proportional to the square of the wheel speed (ω). Consider the effect only of static imbalance, which produces a force in the plane of the rotor (radial direction). Neglect for now the effects of harmonic terms. The imbalance force is given by

$F = u_s \omega^2 \sin \omega t$, where u_s is the static imbalance coefficient. We may simplify the remaining calculations by assuming a constant wheel speed and simple harmonic motion, i.e. neglecting the $\sin \omega t$ term.

Furthermore, we assume that the observatory is a rigid body. In general, flexible body motion will produce relative motion between optics, which may increase the jitter. The calculations are also significantly more complex. Under the rigid body assumption, we can neglect the effects of resonances and establish a minimum LOS error due to the wheel imbalance.

The wheels are located a distance r from the center of mass of the observatory, so the forces produce a

torque $\tau = Fr$, which in turn produces an angular acceleration $\ddot{\theta} = \tau/I$ where I is the moment of inertia. For sinusoidal motion, the angular displacement relates to angular acceleration as $\theta = \ddot{\theta}/\omega^2$. Now we can relate the imbalance force to the LOS error as:

$$\theta = \frac{\tau}{I\omega^2} = \frac{Fr}{I\omega^2} = \frac{u_s \omega^2 r}{I\omega^2} = \frac{u_s r}{I}$$

Therefore, the LOS error is independent of wheel speed under these simplifying assumptions. It varies linearly with both the static imbalance and the distance of the wheel from the center of mass. For the yardstick design, we have $r \sim 3$ m, $I \sim 20000$ kg-m², and $u_s \sim 1.5 \cdot 10^{-4}$ N-s². To first order, then, the expected LOS error is approximately $q = 5 \times 10^{-8}$ radians = 10 mas.

Again, this sets a floor for uncompensated jitter. When the combined effects of static and dynamic imbalance, multiple harmonics, multiple wheels, and flexible body motion are considered, the resulting LOS error turns out to be nearly two orders of magnitude higher in the worst cases of resonances. A more detailed model is required to produce these estimates and to design adequate compensation in the form of vibration isolation.

Detailed simulation

Models of the ACS and FSM subsystems were created and combined with models of the rigid and flexible dynamics, internal and external disturbances, and linear optics (sensitivities). The most significant disturbances are self-induced, resulting from the rotational imbalances and other mechanical sources within the reaction wheels, and noise from the gyros, trackers, and NIR guide star sensor. This integrated model was used to predict several metrics that most strongly affect the science performance, namely wavefront error and centroid error. A block diagram of the model is shown in Figure 7.9. Refer to Monograph 6 for detailed explanations and results.

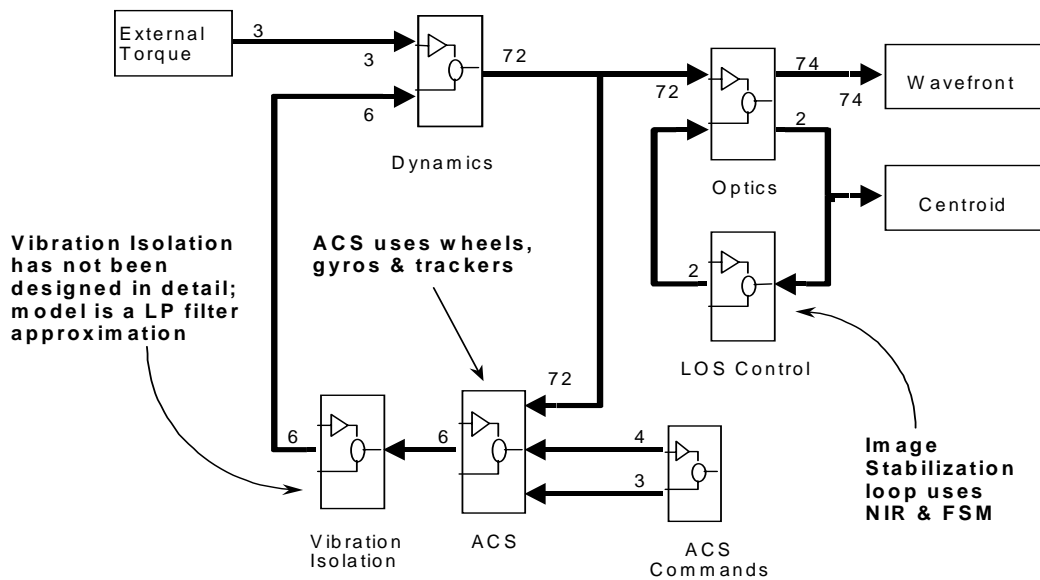


Figure 7.9. Integrated model used for hi-fidelity jitter studies

This model was exercised using both frequency response and time domain simulation methods. Parametric studies were performed to establish baseline (uncompensated) jitter estimates, and to establish requirements for reaction wheel imbalance and vibration isolation. Insight into the results of these studies is offered in Figure 7.10. Under conservative assumptions regarding the combined effects of multiple reaction wheels, peak (3σ) steady-state jitter was estimated using frequency domain techniques for three cases:

- nominal (ACS and FSM attenuation only, standard reaction wheels)
- with $1/10^{\text{th}}$ scale wheel disturbances
- with a 1Hz vibration isolation mount on the (nominal) wheels

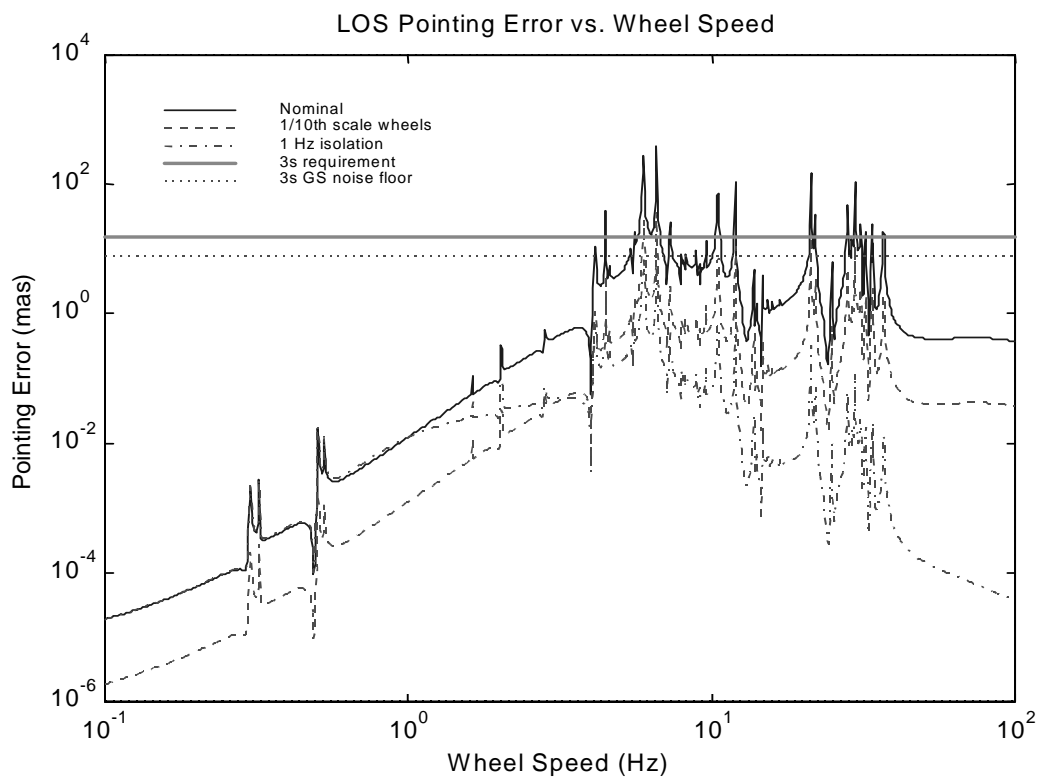


Figure 7.10. Line of sight jitter as a function of reaction wheel speed for nominal wheels of the HST type (solid line), wheels which would be 10 times smaller (dashed line) or with 1 Hz isolation (dash-dot line).

Plotted for reference are both the 15 mas, 3σ , requirement, and the ~ 8 mas 3σ jitter due to guiding sensor noise (constant at all wheel speeds). This guiding sensor noise floor establishes a target for designs efforts to attenuate the dynamic disturbances – attenuating the contribution of wheel forces and torques much beyond this jitter floor is over-design, and would be money better spent elsewhere on NGST.

From the plots for the 3 cases, we can see that above 2 Hz, some amount of vibration isolation or suppression is required to attenuate the effect of the reaction wheel dynamic disturbances. Assuming HST-class wheels, which are among the quietest wheels available, the line of sight jitter exceeds the 5

milli-arcseconds, $1\text{-}\sigma$ requirement over a wide range of wheel speeds at strong structural resonances. Reducing the amplitude of the wheel imbalance terms by a factor of 10 reduces the peak jitter by exactly a factor of 10, a not-unexpected result for a linear analysis. This still fails to meet requirements, and may be difficult and expensive to achieve in practice. However, mounting the wheels on a 1-Hz isolation system reduces jitter at the significant structural modes beyond 10 Hz well below the critical level. Jitter at modes below 10 Hz (secondary mirror support and isolation truss) are attenuated to an almost acceptable level. Use of a time-domain simulation approach with this model eliminated some of the conservatism in the treatment of the wheel disturbances, and showed that a 1-Hz isolation system does indeed meet or exceed the requirement at all wheel speeds.

Table 7.2. Summary of expected pointing performance

<i>Jitter source</i>	<i>Effect on LOS</i>
ACS sensor noise	~1.5" before filtering
Guide star sensor noise	~3.5 mas – 0 mag 16.5 K star
Reaction wheel noise	Wheel speed dependent; $10^2\text{-}10^3$ mas w/o isolation, 10-15 mas w/ isolation
Thermal drifts	a few deg K following large slew, but quasi-static in nature and does not affect LOS stability

Conclusions

The most significant conclusions to result from parametric studies were the following:

- The contribution of the ACS sensor noise is negligible due to the low bandwidth of the ACS.
- The NIR detector noise establishes a lower bound on centroid error of roughly 2.8 mas, 1σ .
- The FSM effectively attenuates only the base motion associated with the low-frequency modes of the sunshield. All other significant modes, such as those of the isolation truss and secondary mirror support, are above the FSM bandwidth. The FSM bandwidth can only be raised if we are willing to accept more contribution from NIR detector noise. The NIR detector noise could be reduced if brighter guide stars could be used, but this, in turn, would require a larger field-of-view for the instrument.
- Some amount of vibration isolation or suppression is required to attenuate the effect of the reaction wheel dynamic disturbances. Assuming HST-class wheels, which are the quietest wheels for which data was found, the centroid error exceeds the 5 mas, 1σ requirement over a wide range of wheel speeds at strong structural resonances. One possibility is the use of passive, active, or hybrid mounts for the wheels, similar to the design for the HST wheels or the hexapod system being studied for SIM. Another possibility is magnetic bearing reaction wheels. Little data is available on these devices, which have limited flight heritage. Yet another possibility is a magnetic suspension system, such as the voice-coil design proposed

during the NGST study phase. All of these technologies are being explored and modeled to understand the performance impact and total system costs associated with each.

- Structural damping is a major factor affecting the performance, and is also an area in which little data is available for analysis. Jitter is inversely proportional to the damping. Global modal damping of 0.1% of critical has been assumed for all frequencies. Data exists which indicates that this assumption is optimistic. Certainly the material damping drops sharply with temperature, and many critical parts of the NGST structure are below 150 K, such as the secondary mirror tower. However, the effect in complex structures is not clearly understood. If damping were to present a problem, it would be paramount to develop solutions such as passive or active damping treatments for the materials and structures. Such technologies have been demonstrated in other applications and even in the space environment, but not at the low temperatures typical of NGST.

Comparisons with HST

Some comparisons between HST and NGST are of interest. Both systems achieve milli-arcsecond pointing stability, but in very different ways. HST has a heavier and more rigid structure. The pointing control system and fine guidance sensors are effectively co-located. It is therefore able to body-point the entire spacecraft with a high-bandwidth servo loop closed around the reaction wheels. NGST is a lightweight, flexible structure. The pointing control system and fine guidance sensors are not co-located. Pointing control must therefore be achieved by cascading control loops: a low bandwidth ACS that provides a platform stable to the arcsecond level, and a high bandwidth FSM loop that reduces LOS errors to the milli-arcsecond level. Both designs feature vibration isolation mounts for the reaction wheels, but NGST requires significantly more performance (lower corner frequency) from the isolators due to the flexibility of the thermal isolation truss and secondary mirror support structure. Basic pointing characteristics for the two observatories are shown in Table 7.3.

Table 7.3. A comparison of NGST yardstick and HST pointing parameters

<i>Parameters</i>	<i>HST</i>	<i>NGST</i>
Inertia (Kg m ²)	70,000	20,000
Lowest mode (Hz)	0.1	0.3
Primary mirror mode (Hz)	60	10
Secondary mirror mode (Hz)	80	4
ACS bandwidth (Hz)	0.5	0.02
Gyro noise (arcsec)	0.01	0.07

8. MASS ESTIMATE

The mass estimate for the entire observatory is shown in Table 8.1. The overall mass is estimated at 3133 kg, which is 128 kg under the lower end capability of the EELV.

Table 8.1. Mass estimate and budget

<i>Item</i>	<i>Estimate</i>	<i>Mass (kg) Margin</i>	<i>Total</i>
Spacecraft Support Module (SSM)			
Attitude Isolation & Mirror (AIM)	84	9	92
Command & Data Handling (C&DH)	11	3	14
Communication/RF	25	3	28
Cryo-Cooler	0	0	0
Electrical Power Subsystem (EPS)	2	11	83
Electrical RSN	7	2	9
Harness	75	23	98
Propulsion/RCS	24	2	26
Structure & Mechanical	175	36	211
Sunshield	129	31	160
Thermal Control Hardware	26	6	32
Contamination Cover (Cocoon)	30	9	39
Total SSM Dry Mass	657	133	791
N2H4 Propellant & He Pressurant	110	0	110
Total SSM Wet Mass	767	133	901
Integrated Science Instrument Module (ISIM)			
Structure	136	27	163
Optics	23	5	28
Detectors	4	1	6
Electronics & Harnessing	57	17	74
Mechanisms	20	6	25
Cryo-Cooler	21	6	27
Miscellaneous	39	12	51
Total ISIM Mass	300	74	374
Optical Telescope Assembly (OTA)			
Primary Mirror	243		
Reaction Structure and Actuators	258		
Structure	143		
Secondary Mirror Assembly	157		
Mechanisms	28		
Electronics & Harnessing	55		
Thermal Control Hardware	20		
Total OTA Mass	904	226	1130
Total Observatory Wet Mass	1971	433	2405
Budgeted Management Reserve			600
Launch Vehicle Performance			3133
Total Payload launch mass is under/over ELV capability			128

9. ORBIT AND LAUNCH

9.1 Orbit

Among possible orbits for NGST (low earth orbit, geostationary, drift orbit, L2, 1 x 3AU heliocentric), the Lagrange 2 point of the Sun-Earth system was selected for the Yardstick mission for the following reasons:

- no short term interruption in target visibility (as in LEO),
- shielding the telescope from the sun also blocks radiation of the earth and moon allowing a high degree of passive cooling,
- easy communication (moderate distance, 8 hr coverage with a single Earth station, continuous coverage with 3 stations),
- easy power generation (compared to 1 x 3AU)
- moderate transfer time (3 months compared to 3 years to get to lowest zodiacal light level in a 1x3AU orbit)
- medium requirement on launch vehicle performance (C3 value -- which indicates the kinetic energy per unit mass that the launch vehicle imparts to a payload, relative to escape velocity, of $-0.7 \text{ km}^2/\text{sec}^2$ compared to 0.4 for the drift orbit and 45 for the 1x3AU orbit).

The main drawback of the L2 orbit is that it is metastable and requires orbit maintenance because of perturbations from the moon and planets. This orbit maintenance is minimized, however, by selecting a large Halo orbit (Figure 9.1). A large Halo orbit avoids eclipses by the Earth and requires only modest delta V requirements for orbit insertion and orbit maintenance. The communications system

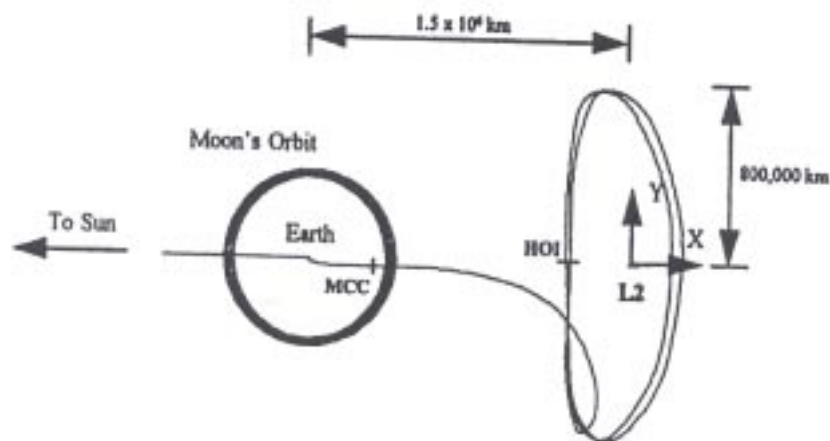


Figure 9.1. Transfer trajectory and Halo orbit around L2 (viewed from the ecliptic pole)

has to work over a greater range of angles but is still compatible with a phased array antenna that should be more reliable than a gimballed antenna.

Orbit insertion is best done by direct injection. Lunar swingby or lunar phasing would require a lower C3 ($-2.24 \text{ km}^2/\text{sec}^2$ instead of -0.7 for direct injection), but takes more time and increases risks due to thermal cycling and exposure to radiation belts during Earth passages.

9.2 Launch vehicle

The launch vehicle envisaged for NGST at the start of the yardstick study (1996) was the Atlas IIARS with the Extended Payload Fairing (EPF) which has the capability of launching 3133 kg into direct transfer trajectory to an L2 orbit and can accommodate payloads up to 3.65 m in diameter. Since then it has become clear that this vehicle will be replaced by the US Air Force Evolved Expendable Launch Vehicle (EELV). Two new families of vehicles are being developed, the Boeing Delta IV and the Lockheed Martin Atlas V, with expected availability in 2002 and 2003 respectively.

The second stages of both vehicles use the same RL-10 engine with liquid hydrogen and oxygen propellants. The biggest apparent difference in the designs is that the first stage of the Delta IV utilizes liquid hydrogen and liquid oxygen, whereas the Atlas V fuel is kerosene and liquid oxygen. In its most basic version, the EELV payload capability would be very similar to that of the Atlas IIARS, with a 3.65 meter ID diameter fairing and a launch capability to L2 transfer orbit of about 2800 kg. But the EELV-Medium, with the optional larger fairing and strap-on solid boosters, offers a significantly larger margin in both volume (4.57 meter ID) and mass (5,000 kg to L2 transfer orbit). Although launch would be more expensive, the overall cost of the mission might be reduced because the need for compactness and lightweighting would be relaxed.

9.3 On-Board propulsion system

The spacecraft is equipped with a propulsion system for L2 halo orbit insertion and station keeping. The same system is also used for momentum dumping.

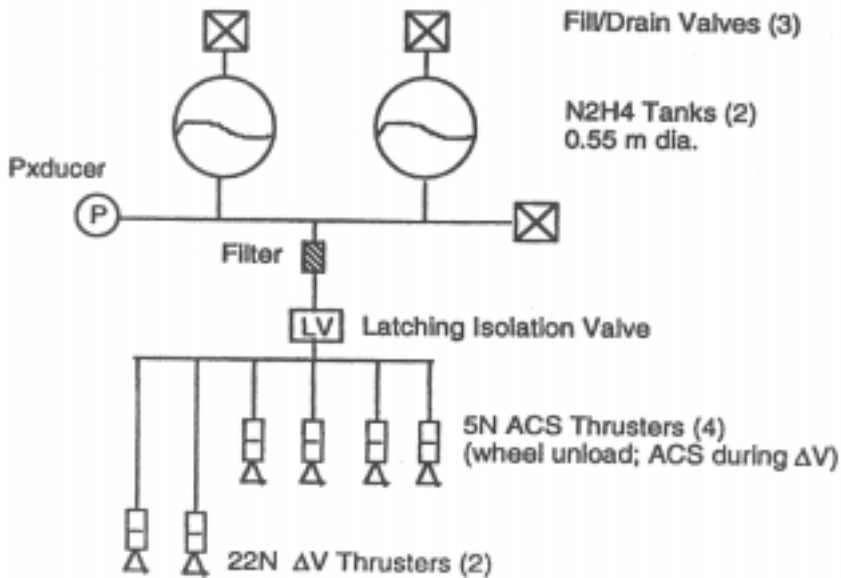
When the Yardstick observatory is in its nominal orientation with respect to the sun (sunshield perpendicular to the sun line), the force due to solar radiation pressure passes through the center of gravity resulting in essentially no torque. But the observatory can be pitched by ± 25 degrees from the sunline for target accessibility. Assuming an average pitch of 12.5 degrees, the unbalance torque results in a daily momentum buildup of 23 Nms. As the reaction wheels have a capacity of only 56 Nms, this momentum must be unloaded on about a daily basis. This could be accomplished by simply chaining observations so that the average pitch is close to zero on the time scale of one or two days. This imposes a serious constraint on observations, however, and it is better to dump momentum using the propulsion system.

The total requirements on the spacecraft propulsion system are summarized in Table 9.1.

Table 9.1. Propulsion requirements

Function	Propulsion Need	Fuel Consumption
Correct +/- sigma LV dispersions	13.5 m/s	20 kg
L2 orbit insertion for direct transfer trajectory	13.5 m/s	20 kg
10 years of L2 orbit station keeping	20 m/s	30 kg
10 years of momentum unloading	47000 Nms	30 kg

In view of the long duration of the mission (10 years), a monopropellant hydrazine (N_2H_4) system has been selected because of its simplicity and reliability. Hydrazine has a specific impulse (I_{sp}) of 220, so that with a payload mass of 2600 kg, the above requirements can be met with about 100 kg of propellant. The system schematically shown in Figure 9.2. The 22N nozzles, whose thruster vectors pass through the NGST CG, are for providing the delta-V for orbit insertion and orbit maintenance. The four canted 5 N nozzles are fired in pairs either to unload momentum or to control attitude during delta-V firings.

**Figure 9.2.** Propulsion system

To prevent propellant products from condensing on the cold optics, all of the thrusters are located on the sun side of the sunshield. However, when the thrust must be towards the sun, this imposes that the observatory be canted beyond its nominal ± 25 degree range. For the short duration of the maneuver, the observatory is pitched 50 degrees from the sunline, the bottom part of the sunshade still fully protecting the OTA and ISIM from the sun (Figure 9.3). The maneuver is short enough that the thermal stability of the observatory is not affected. One of the 22 N nozzles is mounted on a boom and is canted by $+62$ degrees so that its thrust vector passes through the center of gravity and points 112 degrees from the sun. During a burn of the thruster, 37% of the thrust pushes towards the sun. The observatory is then rolled 180 degrees around the sunline and the burn is repeated to cancel out the component of the thrust that is normal to the sun line.

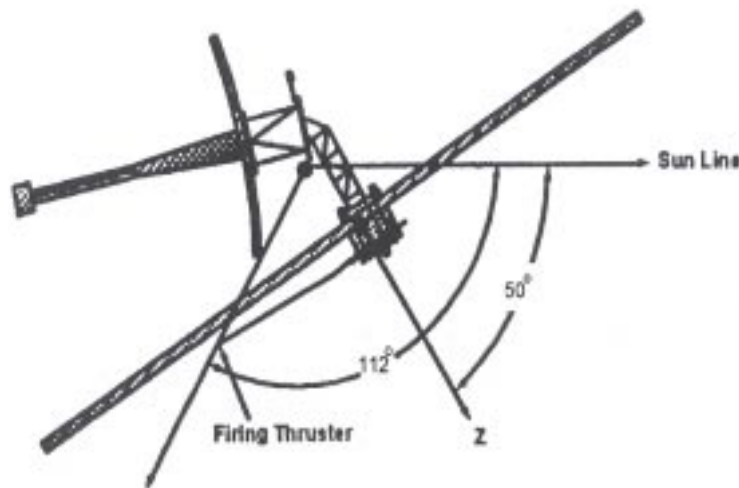


Figure 9.3. Observatory orientation for D-V firing towards the sun

10. OBSERVATORY PERFORMANCE

10.1 Introduction

Like most space missions, a space observatory is a tightly integrated system where most subsystems are strongly interacting and their individual performance must be traded against each other in order to arrive at an optimum design. The case of NGST is particularly difficult because of its complexity and because design margins must be reduced in order to minimize cost. Traditional “error budgeting,” where budgets are assigned to each contributing component and combined in an rms fashion is clearly deficient in this regard. Error sources may not always be Gaussian and may not always be fully independent variables, so that the simple root-mean-square combination is not mathematically correct. Moreover, the determination of the budget components is often done in an educated but “a-priori” fashion instead of being directly traced to the physical characteristics and behavior of the subsystem in question. By necessity, the error budget method does not capture the complexity of the environment or operation conditions and typically only addresses nominal operational modes in average or worst case conditions. Finally, the monetary cost of allocating errors between systems is not taken into account. Ideally, the model could be used to compute partial deviations of performance with respect to cost, so that resources can be allocated properly.

The availability of high fidelity computer modeling offers an ideal solution. It is now possible to develop a detailed computer model of the entire system, simulating actual operating conditions and exploring the trade spaces in order to find the best configuration according to performance and cost criteria.

A first attempt at this overall modeling was performed using the Yardstick design. The primary goal was to establish technical feasibility and determine the expected performance of the observatory. Although our overall design approach strived to reduce cost, cost was not formally included in the model, nor used in the trade studies. The model covered the following subsystems:

- Optics layout (entire optical train including FSM and DM)
- Initial optics position and figure errors
- Wavefront control system (WF sensing, control algorithms)
- Active optics system (mirror positioning and figure control devices)
- Structure (geometry, dynamics, isolation devices)
- Thermal system (radiation, conduction and heaters)
- Attitude control system (reaction wheels, star trackers, attitude control software)
- Guiding system (guide star flux, centroiding)
- Science instruments detectors (pixelization, dark current, readout noise)

Individual models were produced for each subsystem models using traditional optical, mathematical and finite elements methods and combined in a integrated model in a MATLAB/SIMULINK environment.

The main results of the performance analysis are presented hereafter. A first order wavefront error budget established in the traditional manner but based at least partially on the results of the integrated modeling is also given. Sky coverage limitations which were obtained separately from the model are also presented.

10.2 Point spread function

The nominal Point Spread Functions (psf) for the NIR and MIR cameras are shown in Figure 10.1.

These psf assume that the observatory has been aligned, phased and is guided on a star of magnitude 16.5, but the deformable mirror is not active.

They include the following effects:

- Residual polishing errors of the optics (primary and secondary mirrors only)
- Mirror surface deformation due temperature gradients
- Segmented, notched aperture
- Secondary mirror baffle and support structure obscurations
- Residual errors following alignment and phasing
- Detector noise

The psf at 2 μm is shown in Figure 10.1. The Strehl ratio of a point source is 81%, which satisfies the Maréchal condition for diffraction-limited optics. The Strehl degrades only slowly with wavelengths. In the visible, at 0.6 μm , it is still a respectable 0.31. With the use of the DM, simulations indicate that most of the errors can be recovered and the optical system is diffraction-limited at 0.6 μm .

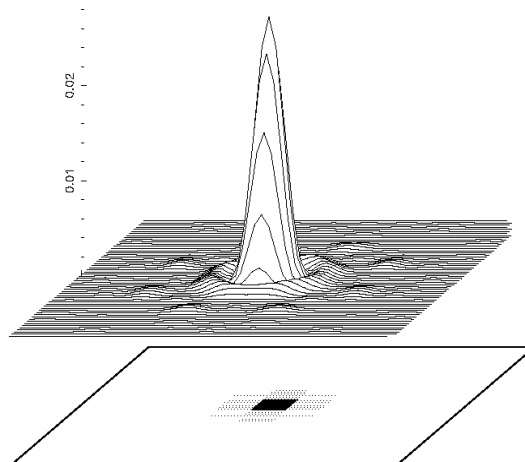


Figure 10.1. Point spread function at 2 micron for 20% bandpass compared to pixel size shown below. The central pixel contains 50% of total energy at 1 μm and 18% at 2 μm .

If the Strehl ratio is a good metric for evaluating the resolution of a telescope, sensitivity is better described by the image sharpness defined as Σpsf^2 . In a background limited observation, the exposure time for imaging a point source with a given signal to noise ratio is given by:

$$t = \frac{Bh^2}{I^2 A \Sigma psf^2}$$

where t is the exposure time, I is the source flux, B the background flux per pixel element, A is the aperture area, h is the desired signal to noise ratio and psf is the normalized 2-dimensional point spread function. With the same assumptions as above, the image sharpness of the Yardstick telescope is shown in Fig 10.2. Although the system is optimized for 2 microns, the sharpness is best at 1 micron: in spite of a reduced image quality at 1 micron compared to 2 microns, the core of the image at 1 micron is smaller because of the reduced wavelength (“wavelength advantage”) resulting in a higher sensitivity in background limited mode.

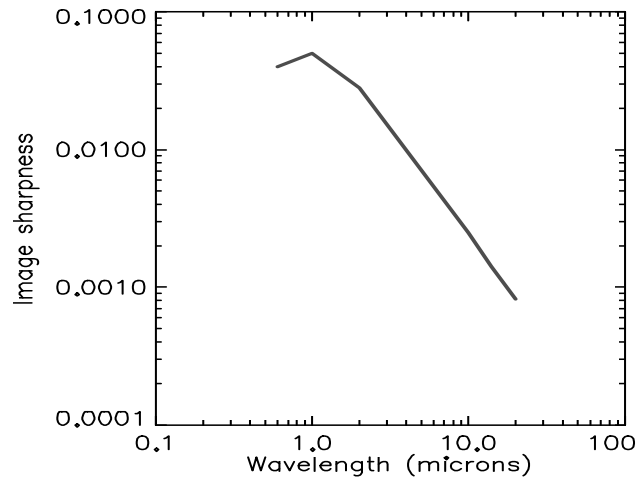


Fig 10.2. Image sharpness as a function of wavelength

10.3 Influence of line of sight jitter

Degradation of the image quality as a function of line of sight jitter is shown in Fig 10.3. Degradation becomes significant when jitter exceeds 5 mas rms which represents 1/5 of a pixel in the NIR camera. The spacecraft attitude control and beam steering systems have been designed to keep line of sight jitter to less than 6 mas rms when using a guide star of magnitude 16.5 in K. (A 16.5 magnitude guide star will supply approximately 14,000 photoelectrons at the detector). There is a 95% probability of being able to find a guide star of magnitude 16.5 or brighter in the NIR camera 4' x 4' field of view when pointing at the ecliptic poles

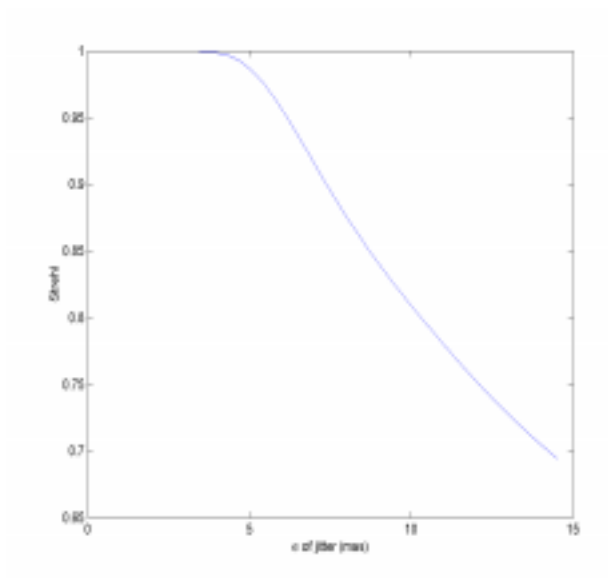


Figure 10.3. Strehl of a point source image at 2 microns as a function of line of sight jitter. The degradation starts to be significant when the jitter exceeds 7 milli-arcseconds radial rms (e.g. 2-dimensional).

The degradation of jitter with guide star magnitude is shown in Figure 10.4.

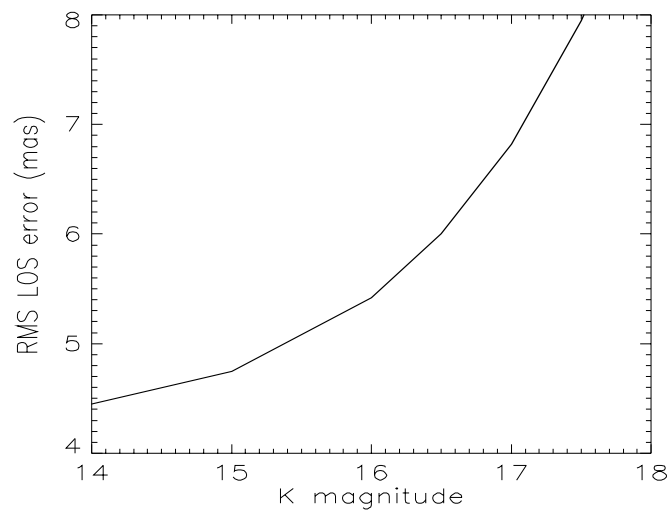


Figure 10.4. Line of sight jitter as a function of guide star magnitude in K

10.4 Slew time - settling time after a slew

The time required for slewing as a function of the angle of slew is shown in Fig 10.5. This time includes the slew time proper and the time for the system to settle to less than 1 arcsecond rms of line of sight error, at which point the guider/FSM system can take over. The settling time is about 2 minutes.

The results assume that the controller bandwidth is 0.025 Hz controller and that the controller damping is 0.707. Pending actual tests, the structural damping was estimated at 0.0001.

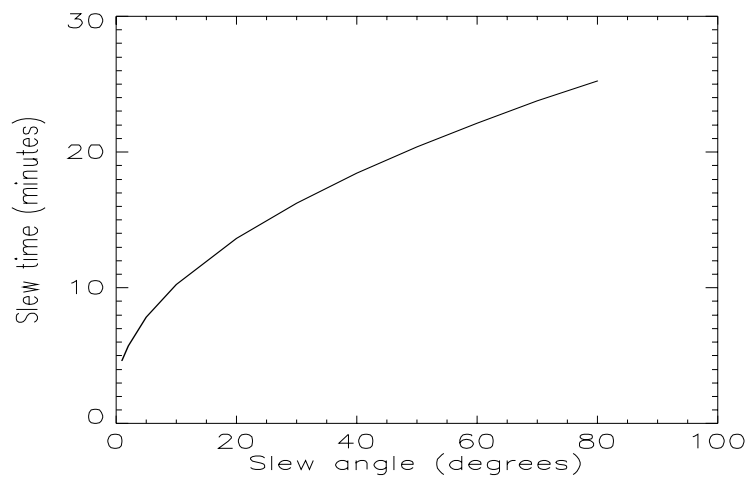


Figure 10.5. Slew time as a function of slew angle

10.5 Thermal effects of slews

The effect of a worst case slew on the image quality is shown in Figure 10.6. The simulation assumes that the optical system has been aligned and phased at the hottest attitude (sunshield perpendicular to the sunline), and that thermal control of the primary mirror is not active. The observatory is then slewed to the coldest attitude (sunshield tilted by 25 degrees). Steady state is reached about 28 hours later. The Strehl ratio which was 0.79 at 2 microns at start ends up at about 0.7 which is barely acceptable.

With thermal control of the primary mirror, however, the degradation is totally negligible: less than 46 nm rms. The power needed for the thermal control of the primary is only 200 mW total and has no influence on the infrared background.

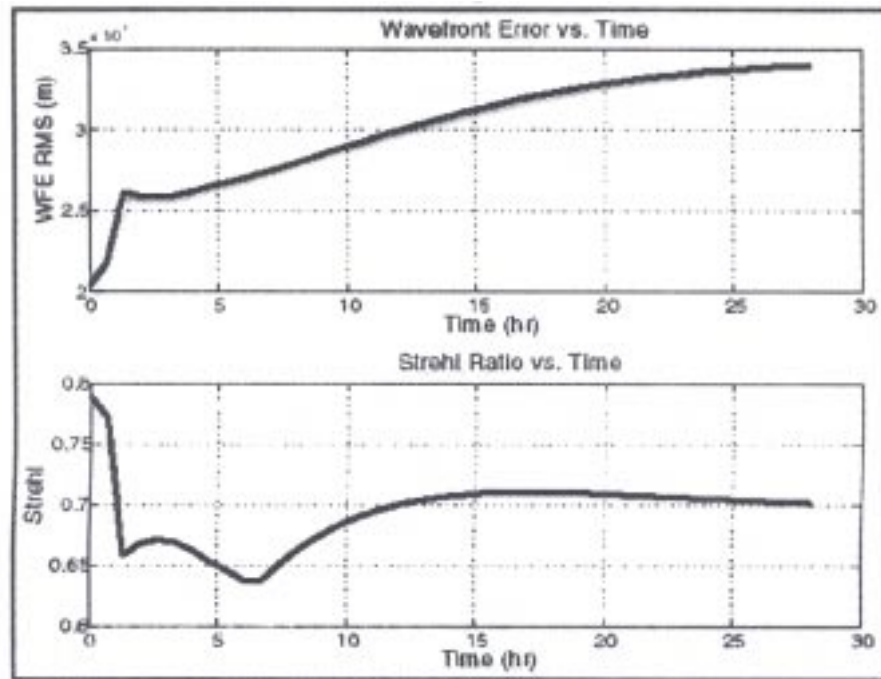


Figure 10.6. Effect of worst case slew on the image quality when the thermal control of the primary mirror is not active. With thermal control, the degradation is negligible (<46 nm).

10.6 Instrumental backgrounds

The various instrumental backgrounds are shown in Figure 10.7. The determination has been made assuming 20% bandpass. As desired, the observatory is zodiacal background limited at least up to 10 microns.

The thermal background is dominated by the back of sunshield radiation scattering off the dust of the primary and secondary mirrors. The calculation assumes about 1% dust coverage on the mirrors. Compared to sunshield scatter, the direct thermal emission of the mirrors is negligible up to 30 microns. The thermal properties of the sunshield degrade with time due to meteoroids and uv exposure. With end of life thermal properties (10 year), the thermal background due to the sunshield is less than the zodiacal light level up to 16 microns. At beginning of life, that cross over point is about 20 microns.

The straylight due to the zodiacal dust, starlight and galactic dust emission is at least on order of magnitude smaller than the zodiacal light seen in the field. (For more details on these results see NGST Monograph 2).

The detector noise background is calculated with the following assumptions:

- dark current: 0.02 electron/s for the NIR detectors and 1 electron/s for the MIR detectors.
- single readout noise of 15 electrons/s
- 32 samples per exposure and
- 1000 seconds sub-exposures (for cosmic ray removal).

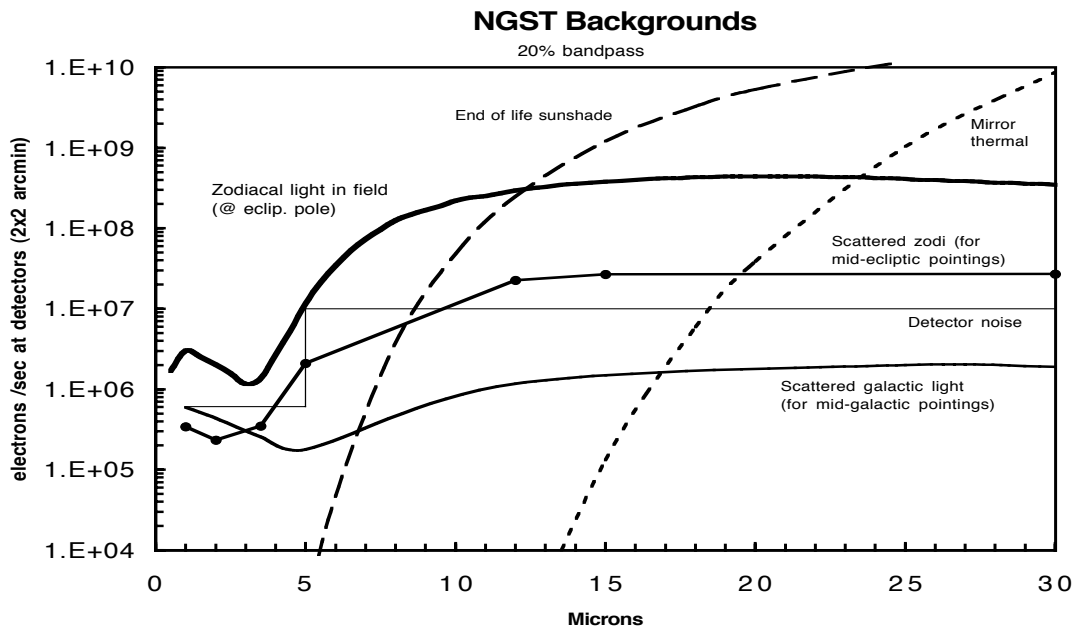


Figure 10.7. Thermal, straylight and detector backgrounds of the observatory assuming 20% bandpass.

10.7 Sky coverage

The observatory can be pitched from 85 to 135 degrees from the sunline and can be rolled 360 degrees around the sunline allowing viewing in a 50 degree wide spherical band (Figure 10.8). This results in an instantaneous sky coverage of 39.7 % of the entire sky. The region near the ecliptic poles is continuously visible and target visibility decreases with ecliptic latitude. Full sky coverage is achieved in slightly under 6 months.

The number of days per year during which a given target is visible is shown in Figure 10.8. Targets can be tracked continuously for a period of at least 7 weeks.

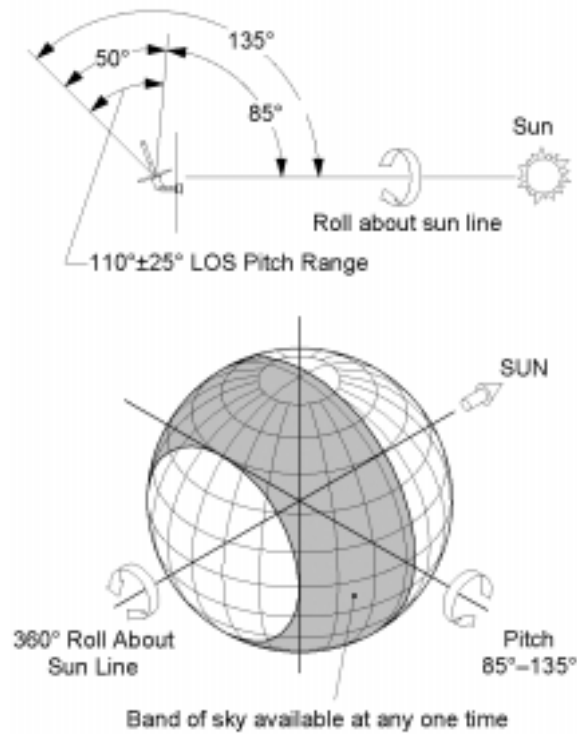


Figure 10.8. Observatory pointing capability (left) and instantaneous sky coverage (right)

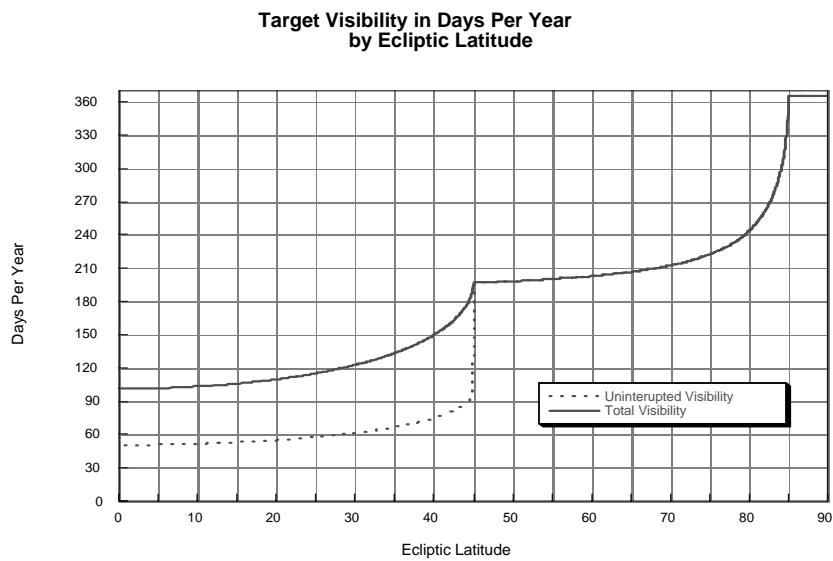


Figure 10.9. Target visibility in days per year as a function of ecliptic latitude

10.8 Wavefront error budget

The system level modeling approach used to evaluate NGST observatory performance, gives the final answer on performance without having recourse to the traditional “error budget”. This is a better approach because the traditional error budget analysis forces to assign a fixed value to each contributor while they could change dynamically and to combine all the contributors in an rms fashion while they may not be fully independent variables. Still, there is value to establishing a strawman “error budget” to provide the orders of magnitude of the various contributors, as long as the assigned budgets are not meant to be definite requirements for each subsystems.

A first order “error budget tree” is shown in Figure 10.10. It is a mixture of assumptions used in the modeling and of results from that modeling itself. It gives the wavefront error in waves at 2 microns for a generic observation, in the following situation:

- the optics has been aligned and phased
- the observatory was slewed to a new target
- the optics were cryo-figured at 100 K, and are now at their nominal on-orbit temperature
- the thermal control of the primary mirror is active
- structural vibrations due to a slew have damped out
- guiding is on a 16.5th magnitude star
- the deformable mirror is not active.

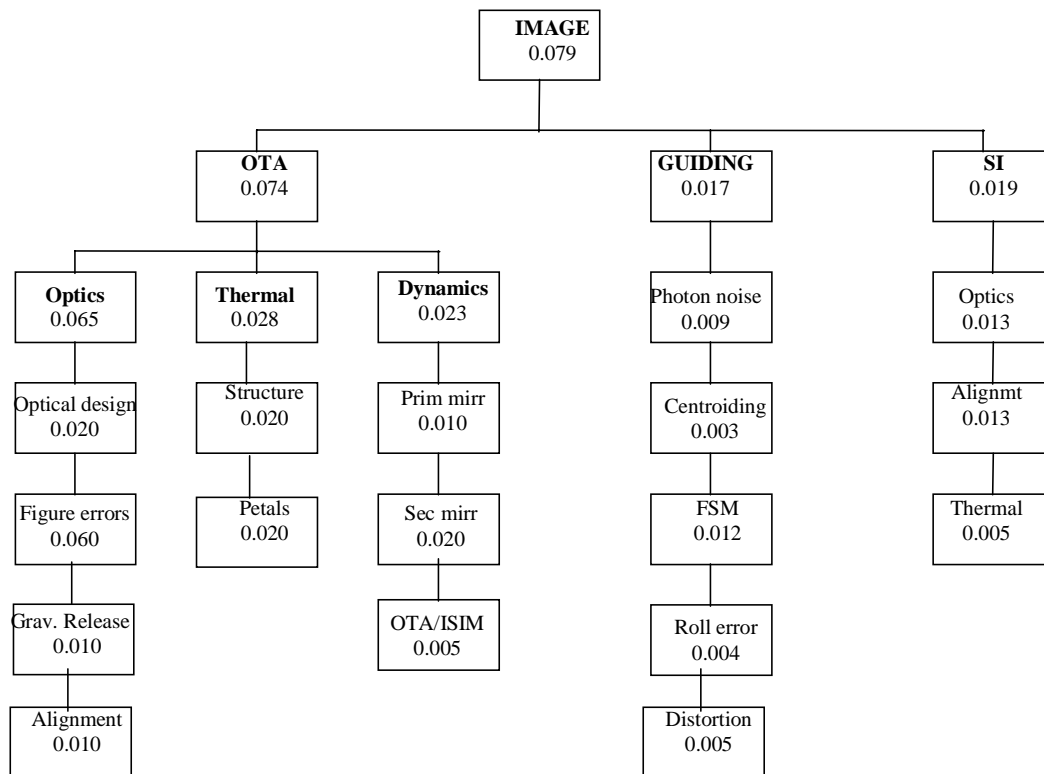


Figure 10.10. First order wavefront error budget wavefront errors are expressed in fraction of wave at 2 microns and rss'd.

An explanation of what each component of the error budget covers follows:

OTA optics:

Optical design: average theoretical wavefront error over the field of the NIR camera

Figure errors: residual mirror figure errors after cryofiguring. This includes the actual figure errors measured on the ground at 100 K during cryofiguring, errors in that measurement, and wavefront errors due to thermal distortion when operating at 30-40 K.

Gravity release: error in the measurement of the mirror figures on the ground with an off-loading system

Alignment (and phasing): Residual error of the wavefront sensing and control system (sensing error, algorithm errors, actuator positioning granularity) following correction

OTA Thermal

Structure thermal drifts: error due to the positional drift of the telescope structure induced by thermal changes following wavefront correction (slew)

Petal warping: errors due to gradients across petals and temperature difference between the actual temperature of each petal and the nominal operational temperature (function of location with respect to the sunshield)

OTA dynamics

Primary mirror: dynamics: error due to the vibration of the mirror surface and of its support system as they excited by disturbances (reaction wheel, sunshield residual motion)

Secondary mirror dynamics: error due to the vibration of the mirror surface and of its support system as they excited by disturbances (reaction wheel, sunshield residual motion)

OTA/SIM dynamics: error induced by the vibration of the ISIM with respect to the OTA as it is excited by disturbances (reaction wheel, sunshield residual motion)

Guiding:

Photon noise: photon noise of the sensing device (16.5th mag star in the NIR camera read at 100Hz)

Centroiding: error due to the centroiding algorithm and camera pixel to pixel calibration

FSM control: residual error in the positioning of the fast steering mirror following control

Roll error: error due to the roll control error (pitch yaw of the image is controlled by the NIR camera guider, but roll is controlled by the spacecraft – see Figure 10.11)

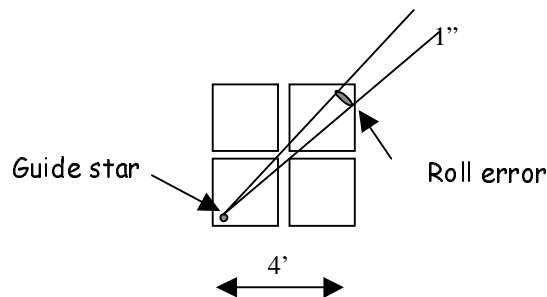


Figure 10.11. The telescope roll around the line of sight is not controlled by focal plane guiding but by the spacecraft attitude control system. This results into an error which grows with the distance to the guide star. The figure above shows the worst case for the NIR camera.

Distortion: error due to the fact that as it steers the beam to keep the target field at the same place on the detector, the FSM shifts the mapping of the sky onto the optics focal surface. The resulting error is the difference between the field distortion on center and that at the average excursion of the FSM.

Science Instrument:

Optics: residual figure errors in the power optics, flat mirrors and filters of the instrument

Optics alignment: wavefront error due to misalignment in the science instrument

Thermal drift: figure errors and positional errors of the optics due to the instrument on orbit temperature being different from the design and ground test temperature (the SI have only focussing adjustment) and thermal transients (due to power cycling)

10.9 Throughput

The overall throughput of the entire optical train all the way to the detector is given in Table 10.1. The wavelengths at which the throughput is calculated for the visible, NIR and MIR are 0.6, 2 and 12 microns respectively. The reflectivity of each reflective surface was taken as 99% in the NIR and MIR and 97% in the visible. The throughput shown for the instruments include the OTA but not the quantum efficiency of the detectors.

Table 10.1. OTA + Instrument throughput

	<i>VIS</i>	<i>NIR</i>	<i>MIR</i>
NIRCAM	0.27	0.84	
NIRSPEC	0.26	0.74	
MIRCAM			0.78
MIRSPEC			0.74

10.10 Meeting the science goals

NGST is an “observatory”, that is to say a multipurpose facility with various science goals. Because observing goals can have somewhat conflicting requirements, the metric used to judge performance consists in determining how well a particular architecture can execute a representative set of observations. A representative set, called the Design Reference Mission (DRM) has been established based on the goals proposed by the HST and Beyond Committee report.

The minimum mission time for NGST is 5 years and it is considered that the DRM should be accomplished in half of that time to allow for general observers programs. The observing program of the DRM (1998 version) together with the exposure time needed when using the Yardstick architecture are shown in Table 10.2. The entire mission is accomplished in 2.42 years.

The surveys of the core program require about half a year for completion (19.9%).

The total observing time by instruments is distributed as follows:

NIR camera: 43.6 %

NIR spectrograph: 35.2%

MIR camera: 8.0 %

MIR spectrograph: 13.2 %

Table 10.2. NGST Science Program

	<i>Inst</i>	<i>S/N req</i>	<i>Spec Res</i>	<i>ABMag</i>	<i>Jansky</i>	<i>Size</i>	<i>Dens /min2</i>	<i>Req #</i>	<i># Visit</i>	<i>Exp hrs</i>	<i># exp</i>	<i>total hours</i>	<i>% mission</i>
COSMIC DISTANCES - CORE													
SN survey	NIR	5	5	31.0	1.45e-009	0.00	100.0	192000	2	3.88	120.00	1038.56	2.37
SN followup	NIR	5	5	31.0	1.45e-009	0.00	0.0	100	5	3.88	100.00	2163.95	4.94
SN spectro	NIRS	3	100	30.3	2.76e-009	0.00	0.0	100	1	15.16	100.00	1686.04	3.85
UNIVERSE AT $z>2$ - CORE													
Primordial Galaxies - deep	NIR	5	2	32.3	4.38e-010	0.50	4000.0	320000	1	125.84	5.00	699.48	1.60
Primordial Galaxies - shallow	NIR	5	2	29.8	4.38e-009	0.50	1000.0	8000000	1	1.26	500.00	704.98	1.61
Prim. Gal. Spectro - deep	NIRS	10	100	29.8	4.38e-009	0.50	1000.0	9000	1	608.42	1.00	676.37	1.54
Prim. Gal. Spectro - shallow	NIRS	10	100	27.3	4.38e-008	0.50	300.0	270000	1	6.08	100.00	677.47	1.55
Prim. Gal. Spectro high res	NIRS	10	1000	27.3	4.38e-008	0.50	300.0	2700	1	338.75	1.00	376.73	0.86
Prim. Gal. Spectro high res	NIRS	10	1000	26.3	1.10e-007	0.50	100.0	9000	1	53.69	10.00	596.98	1.36
Prim. Gal. Spectro high res	NIRS	10	1000	25.3	2.76e-007	0.50	60.0	5400	1	8.51	10.00	94.99	0.22
COSMIC DISTANCES - COMPL													
Gravitational lensing	NIR	100	5	26.8	6.95e-008	0.20	0.0	40	4	0.85	40.00	153.34	0.35
UNIVERSE AT $z>2$ - COMPL													
Birth of quasars	MIR	5	5	26.6	7.98e-008	0.00	0.0	50	1	0.78	50.00	44.26	0.10
Birth quasars spectro	NIRS	5	100	30.3	2.76e-009	0.00	0.0	30	1	42.11	30.00	1404.50	3.21
Birth quasars spectro	MIRS	5	100	25.6	2.00e-007	0.00	0.0	30	1	16.30	30.00	543.85	1.24
Primeaval spheroids	NIR	5	5	28.8	1.10e-008	0.50	0.0	150	1	0.53	468.75	279.32	0.64
Primeaval spheroids	MIR	5	5	25.6	2.00e-007	0.50	0.0	150	1	0.09	1875.00	203.03	0.46
Evolution of disks	NIR	60	5	25.8	1.74e-007	1.00	0.0	50	1	1.21	156.25	211.34	0.48
Evolution of disks	MIR	30	5	23.8	1.05e-006	1.00	0.0	50	1	0.46	625.00	324.23	0.74
Early evol of galaxies	NIR	10	5	28.3	1.74e-008	0.50	0.0	150	1	0.84	468.75	441.51	1.01
Early evol of dark matter	MIR	10	5	25.8	1.67e-007	0.50	0.0	50	1	0.50	625.00	357.78	0.82
Material before galaxies	MIR	10	5	25.0	3.48e-007	0.50	0.0	50	1	0.12	625.00	87.57	0.20
Origin of ISM	NIRS	5	100	27.8	2.76e-008	1.00	0.0	50	1	15.28	50.00	849.94	1.94
Origin of ISM	MIRS	5	100	25.0	3.48e-007	1.00	0.0	50	1	15.36	50.00	854.08	1.95
CHEMICAL EVOLUTION OF ISM	NIRS	30	1000	23.8	1.10e-006	0.00	0.0	150	1	5.71	150.00	953.69	2.18
ACTIVE GALAXIES													
Spectroscopy NIR	NIRS	5	1000	26.8	6.95e-008	0.10	0.0	100	1	1.35	100.00	151.29	0.35
Spectroscopy MIR	MIRS	5	1000	24.6	5.04e-007	0.10	0.0	100	1	5.53	100.00	615.70	1.41
NORMAL GALAXIES	MIRS	10	100	23.0	2.20e-006	1.00	0.0	150	1	1.54	150.00	259.17	0.59
STELLAR DEATH	MIRS	5	1000	22.0	5.52e-006	0.00	0.0	150	1	1.72	150.00	288.64	0.66
STELLAR POPULATION													
Local Group study	NIR	10	5	30.5	2.30e-009	0.00	0.0	150	1	7.12	150.00	1188.76	2.71
Virgo Cluster study	NIR	10	5	32.0	5.78e-010	0.00	0.0	15	1	82.67	15.00	1378.35	3.15
ISM	MIRS	10	1000	20.8	1.67e-005	0.00	0.0	50	3	0.88	50.00	149.55	0.34
BROWN DWARFS	MIR	10	5	26.8	6.64e-008	0.00	0.0	50	1	4.49	50.00	250.30	0.57
CIRCUMSTELLAR GAS/DUST	MIR	10	5	26.8	6.64e-008	0.00	0.0	50	1	4.49	50.00	250.30	0.57
SOLAR SYSTEM													
Planets & asteroids	NIR	10	5	23.8	1.10e-006	0.00	0.0	40	10	0.01	40.00	10.15	0.02
Kuiper Belt survey	NIR	5	5	30.3	2.76e-009	0.00	0.0	50	3	1.32	156.25	693.98	1.58
KBS thermal	MIR	5	5	25.0	3.48e-007	0.00	0.0	50	3	0.05	625.00	116.54	0.27
KBS followup	NIR	10	5	30.3	2.76e-009	0.00	0.0	50	1	5.28	50.00	294.34	0.67
KBS followup	MIR	10	5	26.0	1.39e-007	0.00	0.0	50	1	1.06	50.00	59.72	0.14
KBS follow spectro	MIRS	5	100	24.6	5.04e-007	0.00	0.0	30	1	2.68	30.00	89.91	0.21

APPENDIX A: LIST OF CONTRIBUTORS

Stefi Baum, Space Telescope Science Institute
 Pierre Bely, Space Telescope Science Institute
 Jim Bilbro, Marshall Space Flight Center
 Richard Burg, Johns Hopkins University
 Chris Burrows, Space Telescope Science Institute
 Stefano Casertano, Space Telescope Science Institute
 Steven Castles, Goddard Space Flight Center
 Michael Choi, Goddard Space Flight Center
 Mark Clampin, Space Telescope Science Institute
 Dan Coulter, Jet Propulsion Laboratory
 Larry Craig, Marshall Space Flight Center
 James Crocker, Space Telescope Science Institute
 Mike DiPirro, Goddard Space Flight Center
 Tom Dixon, Ball Aerospace
 Rodger Doxey, Space Telescope Science Institute
 Michael Femiano, Goddard Space Flight Center
 Mike Fitzmaurice, Goddard Space Flight Center
 Bill Forrest, University of Rochester
 Robert Fosbury, European Space Agency
 Paul Geithner, Goddard Space Flight Center
 Larry Germann, Left Hand Design
 Matt Greenhouse, Goddard Space Flight Center
 James Hadaway, University of Alabama
 Tim Hawarden, Joint Astronomy Center
 Allan Hoffman, Santa Barbara Research Center
 Garrett Horner, Langley Research Center
 David Jacobson, Marshall Space Flight Center
 Keith Kalinowski, Goddard Space Flight Center
 Andy Kissil, Jet Propulsion Lab
 Anuradha Koratkar, Space Telescope Science Institute
 Mike Krim, Hughes Dansburry Optical Systems
 Matt Lallo, Space Telescope Science Institute
 Jon Lawrence, Goddard Space Flight Center
 Andrew Lowman, Jet Propulsion Laboratory
 Steven Macenka, Jet Propulsion Laboratory
 John MacKenty, Space Telescope Science Institute

Piero Madau, European Space Agency
John D. Mather, Goddard Space Flight Center
Peter Maymon, Goddard Space Flight Center
Craig McCreight, NASA-Ames Research Center
Mike Mesarch, Goddard Space Flight Center
Wally Meyer, Ball Aerospace
Ralph Mollerick, Goddard Space Flight Center
Sandy Montgomery, Marshall Space Flight Center
Gary Mosier, Goddard Space Flight Center
Max Nein, Marshall Space Flight Center
Yi Ngan, Goddard Space Flight Center
Keith Parrish, Goddard Space Flight Center
Chuck Perrygo, Goddard Space Flight Center
Larry Petro, Space Telescope Institute
Judy Pipher, University of Rochester
Lloyd Purves, Goddard Space Flight Center
John Rakuczy, Marshall Space Flight Center
David Redding, Jet Propulsion Laboratory
George Roach, Goddard Space Flight Center
Greg Schunk, Marshall Space Flight Center
Bernie Seery, Goddard Space Flight Center
Chris Skinner, Space Telescope Science Institute
Eric Smith, Goddard Space Flight Center
Massimo Stiavelli, Space Telescope Science Institute
Peter Stockman, Space Telescope Science Institute
Rodger Thompson, University of Arizona
Mark Wilson, Goddard Space Flight Center
Robert Woodruff, Ball Aerospace
Eve Wooldridge, Goddard Space Flight Center

APPENDIX B: LIST OF ACRONYMS

ACS	Attitude Control System
AU	Astronomical Unit
BOL	Beginning of Life
BP	Bandpass
CCD	Charge-Coupled Device
CG	Center of Gravity
CM	Center of Mass
CTE	Coefficient of Thermal Expansion
C&DH	Command and Data Handling
DET	Direct Energy Transfer
DoD	Depth of Discharge
DM	Deformable mirror
DRM	Design Reference Mission
DFS	Dispersed Fringe Sensor
EELV	Evolved Expandable Launch Vehicle
EOL	End of Life
FOV	Field of View
FSM	Fast Steering Mirror
GS	Guide Star
GSFC	Goddard Space Flight Center
HST	Hubble Space Telescope
IBC	Impurity Band Conduction
IR	Infrared
ISIM	Integrated Science Instrument Module
ISO	Infrared Space Observatory
JPL	Jet Propulsion Laboratory
L2	Second Lagrange Point
LEO	Low Earth Orbit
LOS	Line of Sight
LP	Low Pass (filter)

MIR	Mid Infrared
MLI	Multi-Layer Insulation
MSFC	Marshall Space Flight Center
NASA	National Aeronautics and Space Administration
NEA	Noise Equivalent Angle
NICMOS	Near Infrared Camera and Multi-Object Spectrometer
NIR	Near Infrared
OPD	Optical Path Difference
OTA	Optical Telescope Assembly
PID	Proportional-Integral-Derivative
PM	Primary Mirror
PSE	Power System Electronics
PSF	Point Spread Function
QE	Quantum Efficiency
RMS	Root mean square
RSS	Root square of the Sum of the Squares
SIRTF	Space Infrared Facility
SM	Secondary Mirror
SSM	Spacecraft Support Module
UKIRT	United Kingdom Infrared Facility
WF	Wavefront
WFE	Wavefront error
WFS	Wavefront Sensor
WLI	White Light Interferometry